

DEVELOPMENT OF NOVEL ASSEMBLY APPROACHES FOR SUPERIOR ELECTRODE MATERIALS OF LITHIUM- ION BATTERIES

By Ruiming Huang

A Dissertation submitted to the

Graduate School-Newark

Rutgers, the State University of New Jersey

In partial fulfillment of the requirements

For the degree of

Doctor of Philosophy

Graduate Program in Chemistry

Written under the direction of

Professor Huixin He

And approved by

Newark, New Jersey

October, 2015

COPYRIGHT

©2015

Ruiming Huang

ALL RIGHTS RESERVED

ABSTRACT OF THE THESIS

Development of Novel Assembly Approaches for Superior Electrode

Materials of Lithium-Ion Batteries

By Ruiming Huang

Dissertation Director:

Dr. Huixin He

Rechargeable lithium ion batteries have attracted tremendous attention as “green” technology for electric vehicles and smart grids. In addition, the demand for flexible and high energy batteries has increased exponentially due to the growing need for smartphones and bio-devices over last few years. The conventional inorganic cathode materials (e.g., LiCoO_2 and LiFePO_4) for Lithium ion batteries are not flexible; they are also restricted by their low theoretical specific capacity. To satisfy the emerging large-scale applications of energy storage, new generation batteries should have high power and energy densities, and a long cycle life. In near term, new inorganic cathode and anode materials are developing to increase their capacity. In long term, the next generation batteries were proposed to be made from inexpensive renewable and/or recyclable resources via low energy consumption processes for energy sustainability with minimal environmental footprint. However, issues such as low electronic conductivity, large volume change during the charge/discharge cycles and dissolution of the active materials, commonly existed in these new electrode materials. These problems not only

decrease their energy and power density, charging/discharging rate, but also lead to poor cycling performance, which largely hampered their practical applications. In this thesis, novel assembly approaches were developed to address some of the critical issues for the next generation battery devices with optimum electrochemical performance.

Chapter 1 will include a general overview of basic but important information of current rechargeable Lithium ion battery technology, the requirement for the next generation Lithium ion battery for sustainable energy storage and their current issues and challenges. In addition, the structures, physical properties, methods of fabrications and applications of graphene, an important carbon material was employed for assembly with electrode materials in this thesis, will also be discussed.

In **Chapter 2**, a simple, efficient and scalable assembly method was introduced for the controllable fabrication of nano-structured electrochemical active organic material for sustainable energy storage. Croconic acid disodium salt (CADS) as a sustainable organic electrode example to investigate the size effect on the battery performance of organic electrodes. CADS organic wires with different diameters were fabricated through a facile synthetic route using anti-solvent crystallization method. Cracks and pulverization were observed for micrometer size CADS and its relative low capacity retention rate revealed that lithiation induced strain was also contributed to the limited cycling performance for organic electrode materials. The CADS nanowire exhibits much better electrochemical performance than its crystal bulk material and microwire counterpart. CADS nanowire with a diameter of 150 nm delivers a reversible capability of 177 mAh g^{-1} at a current density of 0.2 C, and retains capacity of 170 mAh g^{-1} after 110 charge/discharge cycles.

The nanowire structure also remarkably enhances the kinetics of croconic acid disodium salt. The CADS nanowire retains 50% of the 0.1 C capacity even when the current density increases to 6 C. In contrast, the crystal bulk and microwire material completely lose their capacities when the current density merely increases to 2 C. Such a high rate performance of CADS nanowire is attributed to its short ion diffusion pathway and large surface area, which enable fast ion and electron transport in the electrode.

In **Chapter 3**, we successfully developed a one-step, bottom up method for direct conversion of H_2S to sulfur@graphene core-shell composite with various shapes (nanoparticles, nanosheets, and nano-wires), which can be used as cathode materials for the next generation Li batteries. This method employed graphene quantum dots as novel catalytic soft templates, taking advantage of their unique amphiphilicity and catalytic characteristics. We found, for the first time, the graphene quantum dots undergo micelle formation in aqueous solution (various solvents). The size and shape of the graphene micelle can be easily adjusted by changing the solution condition (ionic strength, dielectric constant) and it determines the size and shape of the resulted sulfur@graphene core-shell composite material. Our sulfur source, H_2S , a major air pollutant, was directly converted as sulfur based cathode material, which opens up a potential route toward effective pollution control.

We developed a general route to fabricate graphene based free standing, carbon black and binder free, flexible electrodes for high energy lithium ion battery in **Chapter 4**. Various particles (element sulfur, element Tin, Tin oxide and $\text{Li}_{1.2}\text{Mn}_{0.5}\text{Ni}_{0.3}\text{Co}_{0.3}\text{O}_2$) were wrapped by graphene oxide through a simple solution phase assembly approach, no

special interaction was needed. The as-prepared composite can be easily fabricated as free standing, flexible film and directly used as anode/cathode after recover graphene's conductivity through thermal annealing. A free standing, flexible electrode of SnO₂@Graphene was fabricated and used as an example for high energy lithium ion battery. The inter-connected graphene network functions as a conductive buffer matrix for the volume expansion of SnO₂ during charge and discharge. A high specific capacity of 726 mAh g⁻¹ (calculated by the total mass) and area specific capacity of 2.2mAh/cm² was retained after 50 cycles for SnO₂@Graphene composite anode at the current density of 500mA g⁻¹. The assembly method developed in this study is general, robust and easy to apply on other functional materials rather than battery material, which opens up an easy path to fabricate flexible devices.

In the **Chapter 5**, we report a new approach to intentionally induce phase transition of Li-excess layered cathode materials for high-performance lithium ion batteries. In high contrast to the limited layered-to-spinel phase transformation that occurred during in-situ electrochemical cycles, we hereby completely convert a Li-excess layered Li[Li_{0.2}Mn_{0.54}Ni_{0.13}Co_{0.13}]O₂ (LMNCO) to a Li₄Mn₅O₁₂-type spinel product via ex-situ ion-exchanges and a post-annealing process. Such a layered-to-spinel phase conversion is examined using in-situ X-ray diffraction (XRD) and in-situ high-resolution transmission electron microscopy (HRTEM). It is found that generation of sufficient lithium ion vacancies within the Li-excess layered oxide plays a critical role for realizing a complete phase transition. The newly-formed spinel material exhibits initial discharge capacities of 313.6, 267.2, 204.0 and 126.3 mAh g⁻¹ when cycled at 0.1, 0.5, 1 and 5 C (1 C = 250 mA g⁻¹), respectively, and can retain a specific capacity of 197.5 mAh g⁻¹ at 1 C after 100

electrochemical cycles, demonstrating remarkably improved rate capability and cycling stability in comparison with the original Li-excess layered cathode materials. This work sheds light on fundamental understanding of phase transitions within Li-excess layered oxides. It also provides a novel route for tailoring electrochemical performance of Li-excess layered cathode materials for high-capacity lithium ion battery.

In **chapter 6**, a facile surfactant-free sonication-induced route is developed to prepare colloidal nanocrystals of lithium-excess transition metal oxide. The sonication process plays a critical role in forming LMNCO nanocrystals in ethanol (ethanol molecules marked as EtOHs) and inducing the interaction between LMNCO and ethanol molecules. The formation mechanism of LMNCO-EtOHs supramolecules in the colloidal dispersion system is proposed and examined by theoretical simulation and Zeta potential measurement. It is suggested that the as-formed supramolecule is composed of numerous ethanol molecules capping at the surface of LMNCO nanocrystal core via hydrogen bonding. Such chemisorption gives rise to dielectric polarization of the absorbed ethanol molecules, resulting in a negative surface charge of LMNCO colloids. Additionally, diverse superstructures are resulted from self-assembly of LMNCO colloids during evaporation of ethanol. Such self-assembly behaviors of colloidal LMNCO nanocrystals are then investigated by tuning the solvent evaporation condition. The assembled LMNCO architecture also exhibits remarkably improved capacity and cycleability compared to original LMNCO particles, demonstrating a very promising cathode material for next-generation lithium-ion batteries. This work thus provides new insight into the formation and self-assembly of multiple-element complex inorganic colloids in common and surfactant-free solvents for enhanced performance in device applications.

DEDICATION

To my family and friends

Thank you for all the unconditional love, patience and support

ACKNOWLEDGEMENT

I would like to express my deepest and sincerest gratitude to my outstanding research advisor, Dr. Huixin He, for all the supports, advices and encouragement that she has provided during my Ph. D. study at Rutgers. I deeply appreciate her guidance and patience for me.

I would like to also thank all of my committee members, Dr. Phil Huskey, Dr. Jenny Lockard, and Dr. Chunsheng Wang, for spending their precious time and effort in criticizing and correcting my thesis.

Special thanks give to my collaborators: Dr. Chao Luo from Dr. Chunsheng Wang's group for their time to work with me on the coin cell assembly and characterization for the content of chapter 2 and Chapter 3; Dr.Ying Wang and Dr.Jianqiang Zhao from Louisiana State University for their time and help for the content of chapter 5 and Chapter 6 in battery characterization. ; Dr. Eric Garfunkel and his student Feixiang Luo for XPS study; Dr.Michele Pavanello for the theoretical calculation; Yuan Chen from Dr.Jenny Lockard's group for Raman study. Dr.Xiaofeng Zhang from Hitachi, Dr.Jianmin Zuo and his student Wenpei Gao from University of Illinois Urbana-Champaign for In-situ TEM characterization.

I would also like to express my great appreciation to all the faculty and staff members in our department for making my years at Rutgers more enjoyable. I would like to

acknowledge the financial support from our department and National Science Foundation (CBET 1438493).

Finally, but not last, I want to express my gratitude to my parents, my family, my girlfriend Dejing Huang and my friends for their unconditional loves, supports and trusts.

Table of content

ABSTRACT OF THE THESIS	ii
DEDICATION	vii
ACKNOWLEDGEMENT.....	Vviii
Table of content.....	x
List of Figure	xiii
List of Table	xxii
Chapter 1. Introduction.....	1
1.1Research background	1
1.2Lithium-ion battery- working principle.....	2
1.3Anode materials for Lithium-ions battery	4
1.4Cathode materials for Lithium ion battery	7
1.5Motivation and scope.....	17
1.6 References	21
Chapter 2 Anti-solvent promoted self-assembled organic nanowires for high power density lithium ion batteries	26
2.1: Introduction	26
2.2 Results and discussion:	29
2.2.1: Self assemble of CADS from anti-solvent crystallization with and without external nucleus.....	29
2.2.2 Electrochemical evaluation of self-assembled organic nanowires as cathode material for Lithium ion battery	35
2.3 Conclusion:	48
2.4 Materials and methods:	48
2.5 References:.....	52

Chapter 3. Micelle formation of graphene quantum dots and its application as the soft template for the growth of nanomaterial with control size and shape for Lithium ion battery	
.....	Error! Bookmark not defined.
3.1 Introduction	Error! Bookmark not defined.
3.2 results and discussion	Error! Bookmark not defined.
3.2.1 Micelle formation of graphene quantum dots in aqueous solution and its multiple roles in sulfur generation with core-shell structure via one step reaction.	Error! Bookmark not defined.
3.2.2 Electrochemical evaluation of as prepared sulfur@graphene composite and composite with additional polymer coating.	Error! Bookmark not defined.
3.3 Conclusion	Error! Bookmark not defined.
3.4 Materials and methods:	Error! Bookmark not defined.
3.5 References	Error! Bookmark not defined.
Chapter 4. Anti-solvent assisted graphene oxide coating on various electrochemical active materials and its application toward flexible electrode fabrication	76
4.1:Introduction	76
4.2: Result and discussion	79
4.2.1: Anti-solvent precipitation method as a general route to induce graphene coating on various particles with different size and shape	79
4.2.2: Electrochemical evaluation of free standing, additive free SnO₂@Graphene composite anode for Lithium ion battery	83
4.3Conclusion:	91
4.4Materials and methods:	92
4.5 References	95
Chapter 5: Ion Exchange Promoted Phase Transformation of Li-rich Layered Cathode Materials and Related Electrochemical Performance for High-Energy Lithium-Ion Batteries	99
5.1Introduction	99
5.2 Results and discussion	104
5.2.1 Ex-situ phase transition of Li-excess layered cathode materials promoted by two-step ion exchanges followed by post annealing.	104
5.2.2 Electrochemical evaluation of final spinel cathode material for high capacity Lithium ion battery	120
5.3 Conclusions	128

5.4 Materials and Methods	128
5.5 References	132
Chapter 6. Sonication-Induced Colloidal Nanocrystals of High-Capacity Cathode Materials for Advanced Lithium-Ion Batteries	135
6.1 Introduction	135
6.2 Results and Discussion	139
6.2.1 Sonication-induced generation colloidal nanocrystals and solvent evaporation promoted morphology reconstruction of Lithium excessed oxide	139
6.2.2 Structure and electrochemical evaluation of the re-assembled product	153
6.3 Conclusions	155
6.4 Materials and Methods	156
6.5 References	159

List of Figure

Fig. 1.2 A schematic representation of a lithium ion battery based on $\text{LiCoO}_2/\text{Graphite}$...	3
Fig. 1.4.1 The structure and redox mechanism of various types of organic electrode materials.....	10
Fig. 1.4.2 Schematic diagram of Li-S cell.....	13
Fig. 2.1. Molecular structure of croconic acid disodium salt.....	29
Fig. 2.2.1.1: schematic drawing of anti-solvent crystallization.....	30
Fig.2.2.1.2 SEM images 200 μl of a)0.2mg/ml; b)0.4mg/ml; c)0.8mg/ml; d)1mg/ml of CA was added into 12ml of Acetone.....	31
Fig.2.2.1.3 SEM images of CADS product from different poor solvent system a Acetonitril; b Tetrahydroguran; c Dimethylformamide and d Acetonitrile/Chloroform mixture(volume raio 3:1).....	32
Fig.2.2.1.4 SEM images of CADS product with different carbon materials as seeding template: a ME-LOGr; b MWCNT; c NQD and d CB.....	34
Fig. 2.2.2.1. SEM images for CADS micropillar (a), CADS microwire (b) and CADS nanowire (c, d).	36
Fig. 2.2.2.2. XRD patterns of CADS micropillar, CADS microwire and CADS nanowire.....	37
Fig. 2.2.2.3. Electrochemical performance of CADS micropillar, CADS microwire and CADS nanowire. (a) Charge and discharge curves of CADS micropillar, CADS	

microwire and CADS nanowire for the second cycle; Cyclic voltammograms for CADS micropillar (b), CADS microwire (c), CADS nanowire (d).....38

Fig. 2.2.2.4. Calculated energy levels of NaCA and LiCA. Potentials shown are referenced to the Li electrode.....42

Fig. 2.2.2.5. Cycle life (a) and rate capability (b) of CADS micropillar, CADS microwire and CADS nanowire. (1 C is defined as 288 mA g⁻¹).....44

Fig. 2.2.2.6. EIS spectra for CADS micropillar electrode, CADS microwire electrode and CADS nanowire electrode. (The inset is magnification of the semi-circle of CADS Nanowire)45

Fig. 2.2.2.7. SEM images for CADS micropillar (a), CADS microwire (b) and CADS nanowire (c) after 100 cycles.....47

Fig.2.2.2.8. Schematic illustration of lithiation/de-lithiation mechanism for croconic acid disodium salt.....47

Fig. 3.2.1.1 SEM (a) STEM(b) image of as prepared sulfur particles from H₂S H₂O₂ reaction in the existence of NQD; STEM (c) image of empty shell after sulfur removal via heat treatment.....56

Fig. 3.2.1.2 SEM of sulfur@graphene composite material from H₂S H₂O₂ reaction in the present of graphene quantum dots (a) with the addition of 0.5M Na₃PO₄, (b) with the addition of 1M Na₃PO₄,(c)H₂O:Ethonal (1:1) mixed solvent system; STEM (d) image of empty shell after sulfur removal via heat treatment from (c).....58

Fig.3.2.1.3 Critical micelle concentration determined by conductivity measurement. (a) Regular graphene quantum dots; (b) Nitrogen doped graphene quantum dots; (c) Microwave-enabled low oxygen nano graphene.....59

Fig.3.2.1.4 Camera pictures of a)Pure water; b)no heterogeneous catalyst for H_2S H_2O_2 reaction ; c) Conductive nano graphene as the seeding template and catalyst; d) Regular graphene quantum dots as the seeding template and catalyst; e)Nitrogen doped graphene quantum dots as the seeding template and Catalyst.....61

Fig.3.2.1.5 (a)Absorption spectra of 27 $\mu\text{g}/\text{mL}$ NQD in a pH 6.8 Phosphate buffersolution change as a function of time after addition of 300 mM H_2O_2 ; (b)Absorption spectra of 27 $\mu\text{g}/\text{mL}$ NQD in a pH 6.8 phosphate buffer solution change as a function of H_2O_2 concentration.....63

Fig.3.2.1.6 XPS characterization a) C 1s spectrum of nitrogen doped graphene quantum dots; b) N 1s spectrum of nitrogen doped graphene quantum dots; c) C 1s spectrum of sulfur@graphene composite; d) S 2p XPS spectrum and fitted curves for the sulfur@graphene composite.....64

Fig.3.2.2.1 cycle stability of the as prepared sulfur@graphene composite cathode....66

Fig.3.2.2.2 a) STEM image of “carbon shell” after sulfur removal by toluene test; Stability test of sulfur@graphene composite under high vacuum and electron beam irradiation as the function of time b)at 0 min; c)3 min and d 7 min.....67

Fig. 3.2.2.3 STEM images of a) left over of Poly(3,4-ethylenedioxythiophene) coated sample after toluene test; b) left over of Poly-dopamine coated sample after toluene test; c) Poly-dopamine coating composite sample before toluene test at 0min; d) Poly-dopamine coating composite sample before toluene test at 40min.....68

Fig. 4.2.1.1 camera picture of anti-solvent precipitation induce GO coating on a) metallic Sn; b) Lithium excess oxide ($\text{Li}_{1.2}\text{Mn}_{0.5}\text{Ni}_{0.3}\text{Co}_{0.3}\text{O}_2$); c) Element Si; d) SnO_2 , before (small picture) and after (large picture) addition of antisolvent.....81

Fig. 4.2.1.2 SEM of anti-solvent precipitation induce GO coating on a) metallic Sn; b) Lithium excess oxide ($\text{Li}_{1.2}\text{Mn}_{0.5}\text{Ni}_{0.3}\text{Co}_{0.3}\text{O}_2$); c) Element Si; d) SnO_282

Fig. 4.2.2.1 XRD pattern of GO (black), bare SnO_2 (red) and SnO_2 @Graphene composite (blue).....85

Fig. 4.2.2.2 a) Camera pictures of Free standing SnO_2 @Graphene composite anode after thermal annealing at 2000C; b) SEM (zoom in) of free standing SnO_2 @Graphene composite anode ; c) SEM picture (zoom out) of free standing SnO_2 @Graphene composite anode, top view; d) SEM pictures of free standing SnO_2 @Graphene composite anode, side view (intersection).....86

Fig 4.2.2.3 Thermal gravimetric analysis (TGA) of SnO_2 @Graphene composite anode.....87

Fig. 4.2.2.4 a) Cyclic Voltammetry of SnO_2 @Graphene composite anode 1st to 5th cycle in the voltage range of 0.01V to 3V, at the scan rate of 0.1mV/s. b) Galvanostatic

charge/discharge profiles of the 1st, 2nd, 5th, 25th, and 50th cycles at the current density of 500mA/g of SnO₂@Graphene composite anode; c) Cycling performance of bare SnO₂, bare RGO and SnO₂@Graphene composite anode at the current density of 500mA/g; d) rate performance of Free standing SnO₂@Graphene composite anode.....89

Fig. 5.2.1.1 In situ characterizations to identify phase transition of LHMNCO TBA during heat treatments. (a) TG/DTA curves showing weight loss and heat transfer when LHMNCO TBA is heated from room temperature to 950°C (solid lines) and cooled back to ambient temperature (dashed lines) in air, (b) in situ XRD patterns of LHMNCO powders when heated to 900°C and subsequently cooled down to room temperature, with selected portions shown from I to IV.....105

Fig. 5.2.1.2. SEM images of (a) LMNCO, (b) LHMNCO, (c) LHMNCO TBA, (d) LHMNCO TBA Li, (e) LHMNC HT, (f) LHMNCO TBA HT and (g) LHMNCO TBA Li HT.109

Fig. 5.2.1.3 XRD patterns of pristine Li-rich layered Li[Li_{0.2}Mn_{0.54}Ni_{0.13}Co_{0.13}]O₂ nanoparticles and corresponding derivatives in (a) full 2θ range and (b) enlarged 2θ portions between 16-22°, 34-40° and 62-68°. LMNCO: pristine Li[Li_{0.2}Mn_{0.54}Ni_{0.13}Co_{0.13}]O₂ nanoparticles; LHMNCO: LMNCO treated in 2M HCl solution for protonation; LHMNCO TBA: protonated LHMNCO shaken in TBA·OH solution via violent vortex; LHMNCO TBA Li: LHMNCO TBA treated in 1M LiOH solution for Li⁺-TBA⁺ ion exchange; LHMNCO HT, LHMNCO TBA HT and LHMNCO TBA Li HT: LHMNCO, LHMNCO TBA and LHMNCO TBA Li sintered at 500°C in 3h, respectively.111

Fig. 5.2.1.4. TEM and HRTEM images of (a and b) LMNCO, (c and d) LHMNCO, (e and f) LHMNCO TBA, and (g and h) LHMNCO TBA HT115

Fig. 5.2.1.5. (a) Nitrogen adsorption/desorption isotherms and (b) corresponding pore size distributions of LMNCO and LHMNCO TBA and LHMNCO TBA HT.117

Fig. 5.2.2.1. Cyclic voltammetric (CV) curves of (a) LMNCO, (b) LHMNCO HT, (c) LHMNCO TBA HT and (d) LHMNCO TBA Li HT in the first three cycles at a scanning rate of 0.1 mV/s in a voltage range of 2.0-4.8 V vs. Li/Li⁺.121

Fig. 5.2.2.2. Charge and discharge curves of (a) LMNCO, (b) LHMNCO HT, (c) LHMNCO TBA HT and (d) LHMNCO TBA Li HT in the first five cycles at a current density of 0.1 C in a voltage range of 2.0-4.8 V vs. Li/Li⁺.124

Fig. 5.2.2.3. (a) Cycling performance at 1 C and (d) high-rate performance at different currents of LHMNCO HT, LHMNCO TBA HT LHMNCO TBA Li HT in comparison with the pristine layered LMNCO in a voltage range of 2.0-4.8 V vs. Li/Li⁺.126

Fig. 6.2.1.1. SEM image of original LMNCO particles.....139

Fig. 6.2.1.2. Particle size distribution of the as-prepared LMNCO powders.....141

Fig. 6.2.1.3. A theoretical study by simulating the interaction between LMNCO nanocrystals and ethanol molecules via hydrogen bonding: (a) the structural configuration of MnO₆ octahedron representative of Li-excess transition metal oxide, (b) the molecular structure of an ethanol molecule (EtOH) at ground and excited states, respectively, (c) the

composite structure of $\text{MnO}_6\text{-EtOH}$ optimized by Avogadro, and (d) the optimal geometry of $\text{MnO}_6\text{-EtOH}$ by Gaussian 03.....142

Fig. 6.2.1.4. (a) Zeta potentials and photographs in the inset and (b) particle size distribution of LMNCO/ethanol colloidal systems with different dispersion concentrations; (c) TEM images of dominant LMNCO nanocrystals and (d) HRTEM images of LMNCO monocrystals from a colloidal dispersion with a concentration of 0.5 mg/mL.....145

Fig. 6.2.1.5 Schematics showing the sonication-induced colloidal LMNCO nanocrystals to form LMNCO-EtOHs supramolecules, and the resultant superstructures through evaporation-induced self-assembly.147

Fig. 6.2.1.6 FESEM images of various nanoarchitectures via self-assembly of LMNCO colloids on Al substrates at 80°C: (a) fiber networks, (b) regular-shaped blocks, (c) sheet networks, (d) aggregates of particles with magnified details, and (e) a composite structure.149

Fig. 6.2.1.7 SEM images of superstructures assembled from LMNCO colloidal system with a dispersion concentration of 2.5 mg/mL at room temperature prepared in (a) DI water, and (b) methanol with an inserted photo showing corresponding colloidal dispersion.....152

Fig. 6.2.2.1 XRD patterns of original LMNCO particles and the self-assembly product from a colloidal system with a dispersion concentration of 0.5 mg/mL (LMNCO-SA).....153

Fig. 6.2.2.2 Electrochemical performances of original LMNCO particles and the self-assembly product from LMNCO colloidal system (LMNCO-SA), cycled in a voltage range of 2.0-4.8 V *vs.* Li/Li⁺: (a) initial charge and discharge curves, and (b) cycling performances at a current density of 0.5 C (1C = 250 mA/g) and corresponding Columbic efficiencies.....154

List of Table

TABLE 2.2.2.1: Total bonding energy and HOMO-LUMO gap in eV.....	40
TABLE 2.2.2.2: Summary of the calculated electrochemical potentials from the energies in Table 2.2.2.1.....	41
Table 5.2.1. Porous characteristics and elemental composition of LMNCO, LHMNCO TBA and LHMNCO TBA HT.....	123

Chapter 1. Introduction

1.1 Research background

Energy and environmental issues are recognized as two major challenges to maintain sustainable global development in the 21st century. The increasing consumption of fossil fuels causes many problems such as global warming and air pollution due to the emission of CO₂ and other hazardous gas. On the other hand, the supplies of fossil fuels are limited. Therefore, the exploitation and generation of renewable energy has been regarded to be critical to solve our current energy limitation and crisis¹. Over the last few decades, many efforts have been devoted into the exploitation of renewable energy such as wind power, hydro power, biofuels and solar power with fruitful achievements²⁻⁵. Despite of energy generation, development of energy storage devices with high capacity, high efficiency for energy conversion and long service life is also critical for the development of future renewable energy.

In the past two decades, Lithium ion battery technology has achieved great success and been regarded as the most promising solution for energy storage, due to their high energy density, compared to lead-acid, Ni-Cd and Ni-MH battery. It has been successfully employed as the power source of electric vehicles. Several brands have presented their electric vehicles using lithium ion battery packs. For example, Tesla Motor presented the Roadster and Model S, which can offer competitive mileage range to traditional gasoline powered vehicles. Other hybrid vehicles such as Chevrolet Volt and the Toyota Prius have also been available on the market for more than five years. Besides, Lithium-ion batteries dominated the market for portable electronics and played an important role in grid scale stationary storage, enabling effective use of renewable

energies. The conventional inorganic cathode materials (e.g., LiCoO_2 and LiFePO_4) for Lithium ion batteries are restricted by their low theoretical specific capacity. To satisfy the emerging large-scale applications of energy storage, new generation batteries should have high power and energy densities, and a long cycle life. In near term, new inorganic cathode and anode materials are developing to increase their capacity. In long term, the next generation batteries were proposed to be made from inexpensive renewable and/or recyclable resources via low energy consumption processes for energy sustainability with minimal environmental footprint.

1.2 Lithium-ion battery- working principle

Lithium-ion battery has presented various advantages in terms of high specific capacity and operating voltage, excellent rate capability and long-term cycling performance, safety, and environmental benignity compared with traditional lead-acid battery, nickel-metal hydride battery and nickel-cadmium battery⁶. For example, LiCoO_2 based Lithium ion battery (as presented in Fig 1.2) has an operating voltage of 3.7v, which is almost three times in comparison with Lead acid battery. The Lithium-ion battery industry expanded rapidly both in research and market due to its high gravimetric and volumetric energy density after the release of first rechargeable Lithium-ion battery by SONY in the early 1990's.

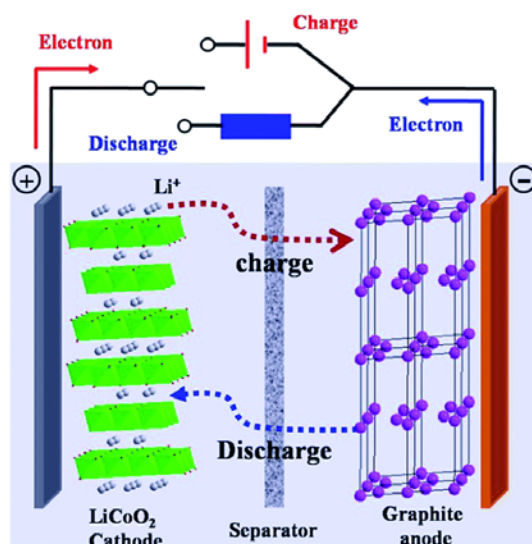


Fig. 1.2 A schematic representation of a lithium ion battery based on LiCoO₂/Graphite⁷

Lithium-ion batteries are comprised of three major components: Cathode, anode and electrolyte. Cathode and anode are separated by a porous membrane (separator) immersed in electrolyte with copper foil as the current collector for anodes and Aluminum foil as the current collector for cathodes. Commercial anode materials are almost exclusively graphite based material. Anode materials with higher energy density, such as Si, SnO₂ and Li₄Ti₅O₁₂⁸⁻¹¹, have been widely studied but still in the research stage. Common active materials for cathode electrode are intercalation compounds, such as LiCoO₂, LiMn₂O₄ and LiFePO₄, which have been widely applied in commercial batteries^{12,13}. As for the electrolyte, Lithium salts such LiPF₆ and LiClO₄ are generally used and dissolved in organic solvents consisting of ethylene carbonate, dimethyl carbonate, and diethyl carbonate, etc. During the operation of Lithium-ions battery, Lithium ions migrate repeatedly between the cathode and the anode. When intercalation compounds were used as cathode materials, Li ions were extracted from the cathode and

migrated to graphite anode during the charge process. The electrons were then migrated through the external circuit. The entire process was reversed during the discharge.

1.3 Anode materials for Lithium-ions battery

Lithium metal anodes are typically used during the initial research development for both anode and cathode materials as the “infinite” Lithium source. While the application of Lithium metal anodes in commercial Lithium ions battery is limited due to its safety issues and dendrite formation. Graphite is commonly applied as the anode material in commercial Lithium ion batteries, due to its long cycle life, abundant material supply and relatively low cost. Graphite can be characterized as a stack of hexagonally bonded sheets of carbon (graphene) held together by van der Waals forces. Lithium ions are able to be inserted in between the planes of graphite. The theoretical capacity of graphite anode is 372 mAh/g¹⁴. This corresponded to the formation of LiC_6 after full intercalation of Lithium ions into graphite. Graphite was widely used also because of their low expansion during Lithium ion insertion, which is directly linked to their ability to maintain their long term cycle stability. However, 372 mAh/g is a relatively low Lithium insertion capacity. Therefore, there has been a growing interest in developing alternative anode materials with enhance safety, high-energy density and long term cycle stability¹⁵.

For the past few years, research efforts on exploring alternative anode materials are mainly focus on alternative carbon materials(carbon nanotube, graphene, mesoporous carbon), Lithium alloy materials (element Si, SnO_2) and nanostructured composite materials. In the later 1990's, research efforts for alternative carbon anode were mainly focused on so call “hard” carbon, which exhibits much higher capacity than LiC_6 ¹⁶⁻¹⁸. The origin of the high capacity from those “hard” carbons was uncertain. Sato's model¹⁶

proposed that the Lithium intercalation happened not only within but also between the graphene layers. The Mabuchi's model¹⁹ assumes that the absorption of large amount of Lithium in the pores or voids of the carbon host is responsible for the high capacity. On the other hand, Dahn's model¹⁸ proposed that the internal surface of the hard carbon also contributed to the total capacity. However, the operation of those "hard" carbon anodes usually accompanied with huge irreversible capacity loss, limited conductivity, as well as relatively short cycle stability.

Graphitic carbon materials other than graphite such as carbon nanotube (CNT) and graphene have also shown great potential as alternative anode. The advantages of these graphitic carbon materials over graphite include their high tensile strength, high conductivity, and relative inertness and much increased capacity without being susceptible to pulverization²⁰. If all the graphene sheets are strictly monolayer, LiC_3 structures can be formed in which lithium is stored on both sides of the graphene sheet, delivered the theoretical capacity of 744mAh/g ²¹. Recently, several strategies have been employed to improve the performance of graphene based anodes. Several studies even presented graphene based anode with specific capacity beyond above mentioned limit. Chemical doping of graphene has also been demonstrated as an effective method for adjusting the physical and chemical properties of graphene resulted from the introduction of suitable reactive sites, which lead to improved electrochemical properties. For example, Zhong et al reported doped graphene shows a high reversible capacity of $>1040\text{mAh/g}$ at a low rate of 50mA/g ²². It also exhibits excellent high rate capability (199 and 235mAh/g was obtained for the N-doped graphene and B-doped graphene at 25A/g (about 30s to full charge). In addition, creating defect on graphene plane is another effective

method to improve its electrochemical performance. The defects on graphene plane not only offer faster ion and electron transfer pathway, but also create more edges, which are more electrochemically active than pristine graphene. Therefore, high specific capacity beyond its theoretical capacity was reported. For example, Zhu et al reported that defect holes can be introduced via KOH treatment²³. Zhao et al also presented defect generation of in-plane carbon via ultrasonic-assisted treatment in hot HNO₃²⁴. On the other hand, graphene not only have a higher capacity in comparison with graphite, it can also be used as a support matrix to form novel graphene and metal oxide composites that can take advantage of the higher capacity of metals oxide which will be discussed later in details.

On the other hand, Lithium alloy material such as element Si (4200 mAh/g)²⁵⁻²⁷ and SnO₂ (1493mAh/g for 8.4e)²⁸⁻³¹ are capable of storing more Lithium ions per-gram than graphitic carbon materials by forming an alloy with Lithium. However, Lithium alloy materials suffer from severe volumetric expansion and contraction during the Lithiation and delithiation, which leads to poor cycle stability. Besides, alloy anodes show high initial irreversible capacities. The causes of large irreversible capacity for alloy anodes can be contributed to: (1) Loss of active materials. Cracking and pulverization of active particles resulting from large volume change during cycling, lead to the disconnection of some alloy particles from the conductive carbon or current collector³²⁻³⁴. The cracking of the active material has been captured by SEM observation³⁵. The breakdown of the conductive network was supported by the sudden increases of the internal resistance of a Si anode at ~0.4 V during the Li-extraction process³³. (2) Formation of Solid Electrolyte Interface (SEI). The formation of this passivation layer was the result of lithium reaction with the electrolyte at the surface of alloy particles, which has been evidenced by

HRTEM, FTIR and XPS^{34,36,37}. (3) After alloyed with active materials, some Li ion might be permanently trapped in the alloys^{38,39}. (4) Aggregation of alloy particles due to the welding effect results from the large volume expansion⁴⁰. Different approaches have been attempted to reduce the first cycle irreversible capacity loss and improve of their cycle stability. Increasing efforts have been focus on incorporating Lithium alloy materials into carbon matrix in order to obtain anode materials with both high energy density and long term cycle stability^{8,11,41}. It has been confirmed in many studies that improved cycle stability can be obtained by preparing alloy/carbon composite either from ball milling or pyrolysis of carbon precursors. This can be attributed to the improvement of electric conductivity and the buffering effect from the carbon matrix for the volume expansion. It was also suggested that the carbon coating can suppress the formation of SEI layers and minimize the aggregation of alloy particles^{42,43}. Other methods were also attempted such as controlling the operating voltage and choosing proper binder and electrolyte specifically for each type of material. In chapter 4, we developed a novel approach to prepare free standing, flexible SnO₂@Graphene composite anode with both high gravimetric specific capacity and area specific capacity. This composite anode is additive free and even current collector free. All the components were involved in Lithium storage and contributed to the total capacity.

1.4Cathode materials for Lithium ion battery

Cathode materials are typically Lithium transition metal oxides, which undergo oxidation when Lithium was removed during charging and reverse back during discharging. The development of state-of-art cathode materials is critical to meet the

requirement of high energy and power density for the electric vehicles, since the cathode materials usually have much lower capacity than anode materials.

In the past two decades, layered LiCoO_2 has been widely used in portable electronic after being introduced by Goodenough *et al.* in 1979 and manufactured by SONY since 1991. The practical capacity of LiCoO_2 is only about 130 mAh g^{-1} , less than half of its theoretical capacity (272 mAh g^{-1}). Its limited capacity along with its high cost and toxicity prevents its large scale application in transportation and stationary energy storage⁴⁴⁻⁴⁶. The olivine lithium iron phosphate (LiFePO_4) is another commercially used cathode material (by BYD and A123), which was first reported by Padhi *et al.* in 1997. In comparison with LiCoO_2 , LiFePO_4 exhibits a higher practical capacity of 170 mAh/g , excellent cycling stability, lower cost, and better safety as well as environmental benignity. The major challenge of this material is its extremely poor electronic conductivity in nature, results in limited rate capability. Research efforts on improving LiFePO_4 's high rate performance have been focused on cation doping and carbon coating in order to increase the overall electronic conductivity⁴⁷⁻⁴⁹. In order to meet the high energy and power densities required for electric vehicles, advanced cathode materials for high performance Lithium ion battery should meet the following standard^{44,50}: (1) High operating voltage and flat voltage plateau. In order to reach high operating voltage, cathode materials are preferred to possess relatively high chemical potential versus Lithium metal. The flat voltage plateau is also necessary for lasting operation of electrical devices; (2) High energy and power density: the advanced cathode materials candidate should have high specific practical capacity and favorable high-rate performance; (3) excellent cycling stability: The reaction between the advanced cathode material with Lithium ions

must be highly reversible during the continuous lithiation and delithiation cycles. Besides, excellent mechanical stability is also critical for maintain structure stability which also contributed to their cycling stability. Other characteristics such as safety, wide operational temperature range, sustainability are also important for the state of art cathode materials candidates.

Recently, Lithium excess layered oxide materials, by “combining” Li_2MnO_3 with LiMO_2 (where $\text{M}=\text{Mn}, \text{Ni}, \text{Co}$) into an integrated component have attracted tremendous research attentions due to its high theoretical capacity ($> 250 \text{ mAh/g}$) and high operating potential ($> 4.5 \text{ V}$). Originally, Li_2MnO_3 was considered to electrochemically inactive. It was employed primarily to stabilize the layered structure. Later, researches revealed that the Li_2MnO_3 component can be activated during the initial charge above $4.5 \text{ V vs. Li/Li}^+$. During such activation process, Li_2MnO_3 is decomposed to Li_2O and MnO_2 due to electrochemical extraction of lithium ions. Simultaneously, this process results in an irreversible oxygen loss and creation of lithium ion vacancies in the layered structure^{51,52}. One phenomenon occurred during subsequent electrochemical cycles of these materials is the unavoidable and continuous layered-to-spinel phase conversion due to the generation of Lithium ion vacancy upon cycling. The newly formed spinel phase can significantly contribute to the high-rate capability, due to its lithium-active characteristics, higher electronic conductivity and facile lithium ion diffusivity^{53,54,55}. On the other hand, the formation of spinel structures breaks down the parent layered lattice and induces lattice strains, causing structural instability during lithiation/delithiation and poor electrochemical reversibility of Li-excess layered cathode materials⁵⁶. Therefore, it would be very intriguing to purposely and controllably induce a layered-to-spinel phase

transformation, in order to explore fundamental mechanism of the layered-to-spinel phase transition and crystal structure of the resultant spinel phase. It would also be very interesting to evaluate electrochemical performance of the resultant spinel structure for use in superior lithium ion batteries. Therefore, in chapter 5, we develop an ex-situ route in this work to realize a layered-to-spinel phase transition of Li-excess layered transition metal oxides for high-performance batteries and offer insight for the detail structure of the newly developed spinel phase. Sonication induced generation of colloidal nanocrystal of Lithium excessed oxide, its morphology reconstruction after solvent evaporation and the impact on its electrochemical performance were also discussed in Chapter 6.

Structure	Redox mechanism	Examples
Conjugated hydrocarbon	$(R)^{+*}_n \longleftrightarrow (R)_n \longleftrightarrow (R)^{-}_n$	<p>PAc PPP</p>
Conjugated amine	$R-\dot{N}^+R \longleftrightarrow R-N^+R$	<p>PAn PPy</p>
Conjugated thioether	$R-S^+-R \longleftrightarrow R-S-R$	<p>PTh TA</p>
Organodisulfide	$R-S-S-R \longleftrightarrow R-S^+ + ^-S-R$	<p>PDMcT PDTTA</p>
Thioether (4e)	$R-\overset{O}{\underset{O}{\parallel}}S-R \longleftrightarrow R-\overset{O}{\parallel}S-R \longleftrightarrow R-S-R$	<p>PEDOT PTBDT</p>
Nitroxyl radical	$R-\dot{N}^+R \longleftrightarrow R-N^+R \longleftrightarrow R-N^+R$	<p></p>
Conjugated carbonyl	$R-\overset{O}{\parallel}C-R \longleftrightarrow R-\overset{O}{\parallel}C-R$	<p>AQ NTCDA</p>

Fig. 1.4.1 The structure and redox mechanism of various types of organic electrode materials⁵⁷

Electroactive organic materials, such as organic salts and polymers, involving reversible redox reactions are promising candidates as alternative cathode materials due

to their higher theoretical capacity, safety, sustainability, environmental friendliness and potential low cost^{58,59}. Fig. 1.4.1 summarized different type of organic electrode materials which has been reported including their structures and redox mechanism. In general, the existence of conjugated structure is critical, since a conjugated structure is beneficial for electron transportation in the reaction and charge delocalization of the redox product. Besides, lone pair electrons usually have a higher reaction activity. Therefore, the redox reaction usually happened on the organic group with conjugated structure and atoms with lone pair electrons, such as N, O and S. Base the above discussion, large amount of organic materials can be designed as potential candidate for cathode material. However, there are other requirements for those organic electrode materials. First of all, the reversibility of the redox reaction and the kinetics associated with the potential candidate need to be excellent. The reversibility corresponds to the cycle stability of the electrochemical cell and the kinetics is usually associated with its rate capability. Secondly, proper redox potential which was determined by the redox organic group is also important since it determined the potential output voltage of the full cell. Unfortunately, the redox potential of above mentioned organic electrode materials are usually between 2.0 and 4.0 V vs. Li^+/Li , which was relatively lower than traditional inorganic intercalation compound. At the meantime, it's usually much easier to design organic electrode material than synthesize it. Therefore a promising organic electrode material should be easily obtained from nature or synthesized. Although organic cathode materials usually have relatively low redox potential, high energy density can be still obtained due to its much higher theoretical and practical capacity compared with inorganic intercalation compound. For example, theoretical energy density of

benzoquinone is close to 1400 Wh kg^{-1} , which was calculated based on 2.8v redox potential and theoretical capacity of 496 mAh g^{-1} ⁶⁰. This is much higher than the commercial LiCoO_2 (550 Wh kg^{-1}). For another, many organic redox reaction possessed much faster reaction kinetics than inorganic intercalation compound. As a result, high power density can also be expected. Different from the inorganic cathodes, which only focus on a few materials, it's believed that there are still many other organic material of different structures can be employed as the cathode materials. Ideally, it's expected that the organic electrode materials can be directly extracted from natural compound or synthesized from biomass as sustainable energy resources. However, there are still several challenges for commercialization and practical use of organic cathode. First of all, Lithium metal was generally used as the anode and lithium source, which brings about safety concern for practical use. For another, apart from conducting polymer, nearly all other organic electrode materials are electrically insulated, which compromise the full usage of the active materials. Besides, more conductive carbon was needed for electrode preparation for the construction of effective electron transfer network, which lower down the percentage loading of the active material. Dissolution of the electrochemical active organic materials into the battery electrolyte was another serious issue for organic cathode materials, which leads to loss of active material and poor cycle stability. The solubility of organic compounds could be reduced by enhancing their polarities via salt formation and solubility of organic salt in organic electrolyte can be further reduced by increasing the concentration of lithium salt in organic electrolyte⁶¹. Due to their high theoretical capacity, fast reaction kinetics, together their structural diversity, conjugated carbonyl compounds were not only the first type organic electrode materials being

studied, but also considered to be the most promising type of organic electrode materials so far. The first organic electrode material, dichloroisocyanuric acid, was reported by D. L. Williams et al in 1969⁶². After that, scientists are trying to explore other small organic molecule with conjugated carbonyl structure as alternative cathode. In chapter 2, croconic acid disodium salt, (CADS, $C_5O_5Na_2$, an organic salt with conjugated carbonyl structure) wires with different diameter were synthesized via anti-solvent crystallization. It was not only investigated as a new candidate of organic cathode material but also was used as model to investigate the size effect on the battery performance of organic electrodes.

Element sulfur is an intriguing cathode material for Lithium ion battery with theoretical capacity of $1,673 \text{mAh g}^{-1}$, more than five times the commercial $LiCoO_2$ cathode. Besides, sulfur is naturally abundant, inexpensive and environmentally friendly^{63,64}. The Li-S cell consists of Lithium metal as the anode, organic electrolyte and composite sulfur cathode as shown in Fig. 1.4.2.

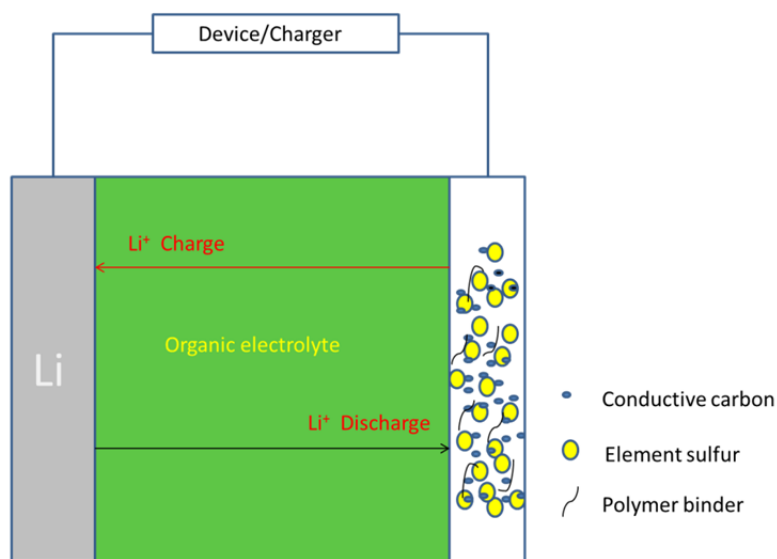


Fig. 1.4.2 Schematic diagram of Li-S cell

The operation of the Li-S cell start with the discharge since element sulfur is in the charged state. During the discharge process, metallic Li is electrochemically oxidized at the negative electrode and produces Lithium ions and electrons. The produced lithium ions are then move internally through the electrolyte to the positive electrode while electrons are transferred to the positive electrode via external circuit, thus electrical current is generated. The overall reaction is shown as follows during the discharge and backward during the charge.



For the idea discharge process, generation of high-order lithium polysulfides Li_2S_x ($6 < x \leq 8$) is first obtained through the reduction of orthorhombic S_8 via ring opening. With the incorporation of additional Lithium ions, lower order of lithium polysulfides Li_2S_x ($2 < x \leq 6$) are formed as the discharge continues. Two discharge plateaus are often observed for ether based electrolyte at 2.3v and 2.1v, which represent the conversion of S_8 to Li_2S_4 and Li_2S_4 to Li_2S , respectively. During the following charge, the Li_2S converts back to S_8 via polysulfide intermediate⁶⁵.

Current challenges for the practical use of Li-S technology including: (1) poor electronic conductivity of element sulfur and its various discharged products (Li_2S_x , $x=2-8$); (2) heavy dissolution of intermediate polysulfide and (3) large volume expansion during charge/discharge cycles⁶⁶⁻⁶⁸. In addition, the dissolved polysulfide shuttles between the anode and cathode. It also reacts with the anode material during the cycles. These issues result in a low utilization of the active material, poor cycle stability, and low

system efficiency. Great efforts have been carried out to address the above issues in order to enable the practical application of Li-S batteries with high energy density and long cycle stability. For example, element sulfur is usually combined with conductive substrate in order to increase the electrical contact. Such composite cathodes are usually prepared via two general strategies: surface coating and sulfur impregnation. Due to its high electrical conductivity, dense structure, and elastic nature, carbon coating has been demonstrated as effective method to improve Li storage property for various electrode materials^{69,70}. However, element sulfur poses relatively low sublimation temperature and melting point. Therefore, traditional methods for carbon coating such as hydrothermal reaction and chemical vapor deposition (CVD) are not suitable for sulfur. As mentioned earlier, graphene or reduced graphene oxide are suitable for low temperature coating in solution phase. It can be wrapped onto the active sulfur particles via ionic strength engineering to form a conducting network and diminish the interface resistance among particles⁷¹. Besides, the flexibility of graphene is beneficial to alleviate the stress introduced by the volume expansion and contraction during the cycling. High specific capacities of sulfur and a favorable cycle life can also be obtained via sulfur coating by conducting polymer^{66,72,73}. Several polymer sulfur core-shell structured cathodes have been reported to have much improved electrochemical performance in terms of high specific capacity and desirable cycle lifespan. The elastic polymer framework can also effectively accommodate the volume variation and trap the soluble polysulfide intermediates. Recently, oxides material such as TiO₂ have been demonstrated to be an effective coating material for sulfur⁷⁴. TiO₂ coating on monodispersed sulfur nanoparticles was first obtained through controlled hydrolysis. S@TiO₂ yolk shell

composite was then obtained by partial dissolution of sulfur. The intact mesoporous TiO_2 shell allows Li^+ to pass through and prevents the polysulfides from dissolving out. On the other hand, the large internal voids in the composite could accommodate the volume expansion of sulfur. Instead of applied conductive coating onto sulfur surface after sulfur was generated, another strategy take advantages of sulfur's low sublimation temperature. Porous substrates such as mesoporous carbon were first prepared via various routes. Sulfur was then impregnated into the pores of the host substrate by heating the substrate and element sulfur mixed at elevated temperature in a sealed vial. This strategy was first reported by Nazar et al by introducing sulfur into an ordered mesoporous carbon (CMK-3) to improve the cycling performance of the sulfur cathode⁷⁵. Since then, various porous materials have been synthesized as the host substrate for sulfur^{67,76-78}. The benefit of this approach is that better sulfur retention can be reached, in comparison with the post carbon or polymer coating. In Chapter 3, we successfully employed graphene quantum dots as the soft template, reporting a one-step, bottom up method for sulfur@graphene core-shell composite fabrication with various shapes (Spherical, nanosheet, nano-wires), by utilizing the unique amphiphilicity of graphene quantum dots. We found, for the first time, the graphene quantum dots undergo micelle formation in aqueous solution (various solvents). The size and shape of the graphene micelle can be easily adjusted by changing the solution condition (ionic strength, dielectric constant) and it determine the size and shape of the resulted sulfur@graphene core-shell composite material. Our sulfur source, H_2S , a major air pollutant, was directly converted as the sulfur cathode, which opens up a potential route toward effective pollution control.

1.5 Motivation and scope

Although the Lithium ion batteries are commercially successful, such as portable devices, extensive research efforts have been devoted to improve their performance, which was mainly promoted by the increasing demand for the energy storage devices with higher energy density and power density. As mentioned earlier, issues such as low electronic conductivity, large volume change during the charge/discharge cycles and dissolution of the active materials, commonly existed in these new electrode materials. These problems not only decrease their energy and power density, charging/discharging rate, but also lead to poor cycling performance. The development of efficient, scalable assembly method for nanostructured electrode materials fabrication has been considered as the most promising direction to resolve the above issues and apply the alternative electrode materials into practical applications. The nanostructured electrode materials exhibit advantages such as short Lithium ion diffusion length, large surface area, fast diffusion rate and capability of effective strain release, which are beneficial for Lithium ion battery technology. Much enhanced capacities, high rate performance, cycle stability, have been found to benefit from nanometer size effects for the novel Li storage systems.

The objective of this dissertation is to develop new assembly approaches for the preparation of nanostructured electrode materials with high energy density, excellent rate capability and cycling stability. The following chapters 2 to chapter 6 present all research achievements in my doctoral program.

In **Chapter 2**, a simple, efficient and scalable assembly method was introduced for the controllable fabrication of nano-structured electrochemical active organic material for sustainable energy storage. Croconic acid disodium salt (CADS) as a sustainable organic electrode example to investigate the size effect on the battery performance of organic electrodes. CADS organic wires with different diameters were fabricated through a facile synthetic route using anti-solvent crystallization method. Cracks and pulverization were observed for micrometer size CADS and its relative low capacity retention rate revealed that lithiation induced strain was also contributed to the limited cycling performance for organic electrode materials. The CADS nanowire exhibits much better electrochemical performance than its crystal bulk material and microwire counterpart. CADS nanowire with a diameter of 150 nm delivers a reversible capability of 177 mAh g⁻¹ at a current density of 0.2 C, and retains capacity of 170 mAh g⁻¹ after 110 charge/discharge cycles. The nanowire structure also remarkably enhances the kinetics of croconic acid disodium salt. The CADS nanowire retains 50% of the 0.1 C capacity even when the current density increases to 6 C. In contrast, the crystal bulk and microwires material completely lose their capacities when the current density merely increases to 2 C. Such a high rate performance of CADS nanowire is attributed to its short ion diffusion pathway and large surface area, which enable fast ion and electron transport in the electrode.

In **Chapter 3**, we successfully employed graphene quantum dots as the soft template, reporting a one-step, bottom up method for sulfur@graphene core-shell composite fabrication with various shapes (Spherical, nanosheet, nano-wires), by utilizing the unique amphiphilicity of graphene quantum dots. We found, for the first time, the graphene quantum dots undergo micelle formation in aqueous solution (various solvents).

The size and shape of the graphene micelle can be easily adjusted by changing the solution condition (ionic strength, dielectric constant) and it determine the size and shape of the resulted sulfur@graphene core-shell composite material. Our sulfur source, H_2S , a major air pollutant, was directly converted as the sulfur cathode, which opens up a potential route toward effective pollution control.

We developed a general route to fabricate graphene based free standing, carbon black and binder free, flexible electrodes for high energy lithium ion battery in **Chapter 4**. Various particles (element sulfur, element Tin, Tin oxide and $\text{Li}_{1.2}\text{Mn}_{0.5}\text{Ni}_{0.3}\text{Co}_{0.3}\text{O}_2$) were wrapped by graphene oxide through a simple solution phase assembly approach, no special interaction was needed. The as-prepared composite can be easily fabricated as free standing, flexible film and directly used as anode/cathode after recover graphene's conductivity through thermal annealing. A free standing, flexible electrode of SnO_2 @Graphene was fabricated and used as an example for high energy lithium ion battery. The inter-connected graphene network functions as a conductive buffer matrix for the volume expansion of SnO_2 during charge and discharge. A high specific capacity of 550 mAh g^{-1} was retained after 100 cycles for SnO_2 @Graphene free standing, flexible electrode at the current density of 200 mA g^{-1} . The assembly method developed in this study is general, robust and easy to apply on other functional materials rather than battery material, which opens up an easy path to fabricate flexible devices.

In **Chapter 5**, reports a new approach to intentionally induce phase transition of Li-excess layered cathode materials for high-performance lithium ion batteries. In high contrast to the limited layered-to-spinel phase transformation that occurred during in-situ electrochemical cycles, we hereby completely convert a Li-excess layered

$\text{Li}[\text{Li}_{0.2}\text{Mn}_{0.54}\text{Ni}_{0.13}\text{Co}_{0.13}]\text{O}_2$ (LMNCO) to a $\text{Li}_4\text{Mn}_5\text{O}_{12}$ -type spinel product via ex-situ ion-exchanges and a post-annealing process. Such a layered-to-spinel phase conversion is examined using in-situ X-ray diffraction (XRD) and in-situ high-resolution transmission electron microscopy (HRTEM). It is found that generation of sufficient lithium ion vacancies within the Li-excess layered oxide plays a critical role for realizing a complete phase transition. The newly-formed spinel material exhibits initial discharge capacities of 313.6, 267.2, 204.0 and 126.3 mAh g^{-1} when cycled at 0.1, 0.5, 1 and 5 C (1 C = 250 mA g^{-1}), respectively, and can retain a specific capacity of 197.5 mAh g^{-1} at 1 C after 100 electrochemical cycles, demonstrating remarkably improved rate capability and cycling stability in comparison with the original Li-excess layered cathode materials. This work sheds light on fundamental understanding of phase transitions within Li-excess layered oxides. It also provides a novel route for tailoring electrochemical performance of Li-excess layered cathode materials for high-capacity lithium ion battery.

In **chapter 6**, a facile surfactant-free sonication-induced route is developed to prepare colloidal nanocrystals of lithium-excess transition metal oxide. The sonication process plays a critical role in forming LMNCO nanocrystals in ethanol (ethanol molecules marked as EtOHs) and inducing the interaction between LMNCO and ethanol molecules. The formation mechanism of LMNCO-EtOHs supramolecules in the colloidal dispersion system is proposed and examined by fluorescence spectra, theoretical simulation and Zeta potential measurement. It is suggested that the as-formed supramolecule is composed of numerous ethanol molecules capping at the surface of LMNCO nanocrystal core via hydrogen bonding. Such chemisorption gives rise to dielectric polarization of the absorbed ethanol molecules, resulting in a negative surface

charge of LMNCO colloids. Additionally, diverse superstructures are resulted from self-assembly of LMNCO colloids during evaporation of ethanol. Such self-assembly behaviors of colloidal LMNCO nanocrystals are then investigated by tuning the solvent evaporation condition. The assembled LMNCO architecture also exhibits remarkably improved capacity and cycleability compared to original LMNCO particles, demonstrating a very promising cathode material for next-generation lithium-ion batteries. This work thus provides new insight into the formation and self-assembly of multiple-element complex inorganic colloids in common and surfactant-free solvents for enhanced performance in device applications.

1.6 References

- 1 Manthiram, A. Materials challenges and opportunities of lithium ion batteries. *The Journal of Physical Chemistry Letters* 2, 176-184 (2011).
- 2 Benemann, J. Hydrogen biotechnology: progress and prospects. *Nature biotechnology* 14, 1101-1103 (1996).
- 3 Paish, O. Small hydro power: technology and current status. *Renewable and sustainable energy reviews* 6, 537-556 (2002).
- 4 Ackermann, T. *Wind power in power systems*. (John Wiley & Sons, 2005).
- 5 Willner, I., Yan, Y. M., Willner, B. & Telieps, R. Integrated Enzyme-Based Biofuel Cells—A Review. *Fuel Cells* 9, 7-24 (2009).
- 6 Goodenough, J. B. & Kim, Y. Challenges for rechargeable Li batteries†. *Chemistry of Materials* 22, 587-603 (2009).
- 7 Xu, G.-L. et al. Tuning the structure and property of nanostructured cathode materials of lithium ion and lithium sulfur batteries. *J. Mater. Chem. A* 2, 19941-19962 (2014).
- 8 Terranova, M. L., Orlanducci, S., Tamburri, E., Guglielmotti, V. & Rossi, M. Si/C hybrid nanostructures for Li-ion anodes: An overview. *Journal of Power Sources* 246, 167-177 (2014).
- 9 Chiu, H.-c. et al. Aqueous synthesized nanostructured Li₄Ti₅O₁₂ for high-performance lithium ion battery anodes. *Journal of The Electrochemical Society* 160, A3041-A3047 (2013).
- 10 Hovington, P. et al. In situ Scanning electron microscope study and microstructural evolution of nano silicon anode for high energy Li-ion batteries. *Journal of Power Sources* 248, 457-464 (2014).

- 11 Ramasamy, E. & Lee, J. Ordered Mesoporous SnO₂- Based Photoanodes for High-Performance Dye-Sensitized Solar Cells. *The Journal of Physical Chemistry C* 114, 22032-22037 (2010).
- 12 Whittingham, M. S. Electrical energy storage and intercalation chemistry. *Science* 192, 1126-1127 (1976).
- 13 Guyomard, D. & Tarascon, J. Li Metal-Free Rechargeable LiMn₂O₄/Carbon Cells: Their Understanding and Optimization. *Journal of The Electrochemical Society* 139, 937-948 (1992).
- 14 Winter, M., Besenhard, J. O., Spahr, M. E. & Novak, P. Insertion electrode materials for rechargeable lithium batteries. *Advanced materials* 10, 725-763 (1998).
- 15 Larcher, D. et al. Recent findings and prospects in the field of pure metals as negative electrodes for Li-ion batteries. *Journal of Materials Chemistry* 17, 3759-3772 (2007).
- 16 Endo, M., Nishimura, Y., Takahashi, T., Takeuchi, K. & Dresselhaus, M. Lithium storage behavior for various kinds of carbon anodes in Li ion secondary battery. *Journal of Physics and Chemistry of Solids* 57, 725-728 (1996).
- 17 Zheng, T., Xing, W. & Dahn, J. Carbons prepared from coals for anodes of lithium-ion cells. *Carbon* 34, 1501-1507 (1996).
- 18 Zheng, T., Xue, J. & Dahn, J. Lithium insertion in hydrogen-containing carbonaceous materials. *Chemistry of materials* 8, 389-393 (1996).
- 19 Mabuchi, A., Tokumitsu, K., Fujimoto, H. & Kasuh, T. Charge-discharge characteristics of the mesocarbon microbeads heat-treated at different temperatures. *Journal of the Electrochemical Society* 142, 1041-1046 (1995).
- 20 de las Casas, C. & Li, W. A review of application of carbon nanotubes for lithium ion battery anode material. *Journal of Power Sources* 208, 74-85 (2012).
- 21 Wang, G. et al. Sn/graphene nanocomposite with 3D architecture for enhanced reversible lithium storage in lithium ion batteries. *Journal of Materials Chemistry* 19, 8378-8384 (2009).
- 22 Wu, Z.-S., Ren, W., Xu, L., Li, F. & Cheng, H.-M. Doped graphene sheets as anode materials with superhigh rate and large capacity for lithium ion batteries. *ACS nano* 5, 5463-5471 (2011).
- 23 Zhu, Y. et al. Carbon-based supercapacitors produced by activation of graphene. *Science* 332, 1537-1541 (2011).
- 24 Zhao, X., Hayner, C. M., Kung, M. C. & Kung, H. H. Flexible holey graphene paper electrodes with enhanced rate capability for energy storage applications. *Acs Nano* 5, 8739-8749 (2011).
- 25 Park, M.-H. et al. Silicon nanotube battery anodes. *Nano Letters* 9, 3844-3847 (2009).
- 26 Jung, D. S., Hwang, T. H., Park, S. B. & Choi, J. W. Spray drying method for large-scale and high-performance silicon negative electrodes in Li-ion batteries. *Nano letters* 13, 2092-2097 (2013).
- 27 Green, M., Fielder, E., Scrosati, B., Wachtler, M. & Moreno, J. S. Structured silicon anodes for lithium battery applications. *Electrochemical and Solid-State Letters* 6, A75-A79 (2003).
- 28 Vinayan, B. & Ramaprabhu, S. Facile synthesis of SnO₂ nanoparticles dispersed nitrogen doped graphene anode material for ultrahigh capacity lithium ion battery applications. *Journal of Materials Chemistry A* 1, 3865-3871 (2013).
- 29 Zhang, L., Wu, H. B., Liu, B. & Lou, X. W. D. Formation of porous SnO₂ microboxes via selective leaching for highly reversible lithium storage. *Energy & Environmental Science* 7, 1013-1017 (2014).
- 30 Gao, T. et al. Free-standing SnO₂ nanoparticles@ graphene hybrid paper for advanced lithium-ion batteries. *Ceramics International* 40, 6891-6897 (2014).

- 31 Wang, X. et al. N-Doped Graphene-SnO₂ Sandwich Paper for High-Performance Lithium-Ion Batteries. *Advanced Functional Materials* 22, 2682-2690 (2012).
- 32 Yang, J., Wachtler, M., Winter, M. & Besenhard, J. O. Sub-Microcrystalline Sn and Sn-SnSb Powders as Lithium Storage Materials for Lithium-Ion Batteries. *Electrochemical and Solid-State Letters* 2, 161-163 (1999).
- 33 Ryu, J. H., Kim, J. W., Sung, Y.-E. & Oh, S. M. Failure modes of silicon powder negative electrode in lithium secondary batteries. *Electrochemical and Solid-State Letters* 7, A306-A309 (2004).
- 34 Stjern Dahl, M. et al. Surface chemistry of intermetallic AlSb-anodes for Li-ion batteries. *Electrochimica acta* 52, 4947-4955 (2007).
- 35 Ulus, A., Rosenberg, Y., Burstein, L. & Peled, E. Tin alloy-graphite composite anode for lithium-ion batteries. *Journal of The Electrochemical Society* 149, A635-A643 (2002).
- 36 Li, H. et al. The crystal structural evolution of nano-Si anode caused by lithium insertion and extraction at room temperature. *Solid State Ionics* 135, 181-191 (2000).
- 37 Alcántara, R. et al. Electrochemical reaction of lithium with the CoSb₃ skutterudite. *Journal of Materials Chemistry* 9, 2517-2521 (1999).
- 38 Limthongkul, P., Jang, Y.-I., Dudney, N. J. & Chiang, Y.-M. Electrochemically-driven solid-state amorphization in lithium-metal anodes. *Journal of power sources* 119, 604-609 (2003).
- 39 Ferguson, P., Dunlap, R. & Dahn, J. An in situ study of the electrochemical reaction of Li with nanostructured Sn₃₀Co₃₀C₄₀. *Journal of The Electrochemical Society* 157, A326-A332 (2010).
- 40 Li, H., Shi, L., Lu, W., Huang, X. & Chen, L. Studies on capacity loss and capacity fading of nanosized SnSb alloy anode for Li-ion batteries. *Journal of The Electrochemical Society* 148, A915-A922 (2001).
- 41 Xu, Y., Guo, J. & Wang, C. Sponge-like porous carbon/tin composite anode materials for lithium ion batteries. *Journal of Materials Chemistry* 22, 9562-9567 (2012).
- 42 Saint, J. et al. Towards a fundamental understanding of the improved electrochemical performance of silicon-carbon composites. *Advanced functional materials* 17, 1765 (2007).
- 43 Yoshio, M. et al. Carbon-coated Si as a lithium-ion battery anode material. *Journal of The Electrochemical Society* 149, A1598-A1603 (2002).
- 44 Xu, B., Qian, D., Wang, Z. & Meng, Y. S. Recent progress in cathode materials research for advanced lithium ion batteries. *Materials Science and Engineering: R: Reports* 73, 51-65 (2012).
- 45 Mizushima, K., Jones, P., Wiseman, P. & Goodenough, J. B. Li_xCoO₂ (0. Materials Research Bulletin 15, 783-789 (1980).
- 46 Amatucci, G., Tarascon, J. & Klein, L. CoO₂, the end member of the Li_xCoO₂ solid solution. *Journal of The Electrochemical Society* 143, 1114-1123 (1996).
- 47 Chen, J.-M., Hsu, C.-H., Lin, Y.-R., Hsiao, M.-H. & Fey, G. T.-K. High-power LiFePO₄ cathode materials with a continuous nano carbon network for lithium-ion batteries. *Journal of Power Sources* 184, 498-502 (2008).
- 48 Liu, J. et al. Long-term cyclability of LiFePO₄/carbon composite cathode material for lithium-ion battery applications. *Electrochimica Acta* 54, 5656-5659 (2009).
- 49 Doherty, C. M., Caruso, R. A., Smarsly, B. M. & Drummond, C. J. Colloidal crystal templating to produce hierarchically porous LiFePO₄ electrode materials for high power lithium ion batteries. *Chemistry of Materials* 21, 2895-2903 (2009).
- 50 Whittingham, M. S. Lithium batteries and cathode materials. *Chemical reviews* 104, 4271-4302 (2004).
- 51 Yabuuchi, N., Yoshii, K., Myung, S.-T., Nakai, I. & Komaba, S. Detailed studies of a high-capacity electrode material for rechargeable batteries, Li₂MnO₃-

- LiCo_{1/3}Ni_{1/3}Mn_{1/3}O₂. *Journal of the American Chemical Society* 133, 4404-4419 (2011).
- 52 Hy, S., Felix, F., Rick, J., Su, W.-N. & Hwang, B. J. Direct In situ Observation of Li₂O Evolution on Li-Rich High-Capacity Cathode Material, Li [Ni_xLi (1-2 x)/3Mn (2-x)/3]O₂ (0 ≤ x ≤ 0.5). *Journal of the American Chemical Society* 136, 999-1007 (2014).
- 53 Song, B. et al. High rate capability caused by surface cubic spinels in Li-rich layer-structured cathodes for Li-ion batteries. *Scientific reports* 3, 3094, doi:10.1038/srep03094 (2013).
- 54 Ates, M. N. et al. Mitigation of Layered to Spinel Conversion of a Li-Rich Layered Metal Oxide Cathode Material for Li-Ion Batteries. *Journal of the Electrochemical Society* 161, A290-A301, doi:10.1149/2.040403jes (2013).
- 55 Wang, D., Belharouak, I., Zhou, G. & Amine, K. Nanoarchitecture Multi-Structural Cathode Materials for High Capacity Lithium Batteries. *Advanced Functional Materials* 23, 1070-1075, doi:10.1002/adfm.201200536 (2013).
- 56 Gu, M. et al. Formation of the Spinel Phase in the layered composite cathode used in Li ion batteries (Jianqingzhao's conflicted copy 2014-02-17).pdf>. *ACS Nano* 7, 760-767 (2013).
- 57 Song, Z. & Zhou, H. Towards sustainable and versatile energy storage devices: an overview of organic electrode materials. *Energy & Environmental Science* 6, 2280-2301 (2013).
- 58 Poizot, P. & Dolhem, F. Clean energy new deal for a sustainable world: from non-CO₂ generating energy sources to greener electrochemical storage devices. *Energy & Environmental Science* 4, 2003-2019 (2011).
- 59 Liang, Y., Tao, Z. & Chen, J. Organic electrode materials for rechargeable lithium batteries. *Advanced Energy Materials* 2, 742-769 (2012).
- 60 Senoh, H., Yao, M., Sakaebe, H., Yasuda, K. & Siroma, Z. A two-compartment cell for using soluble benzoquinone derivatives as active materials in lithium secondary batteries. *Electrochimica Acta* 56, 10145-10150 (2011).
- 61 Armand, M. et al. Conjugated dicarboxylate anodes for Li-ion batteries. *Nature materials* 8, 120-125 (2009).
- 62 Williams, D., Byrne, J. & Driscoll, J. A high energy density lithium/dichloroisocyanuric acid battery system. *Journal of The Electrochemical Society* 116, 2-4 (1969).
- 63 Manthiram, A., Fu, Y. & Su, Y.-S. Challenges and prospects of lithium-sulfur batteries. *Accounts of chemical research* 46, 1125-1134 (2012).
- 64 Sun, L. et al. Sulfur Nanocrystals Confined in Carbon Nanotube Network As a Binder-Free Electrode for High-Performance Lithium Sulfur Batteries. *Nano letters* 14, 4044-4049 (2014).
- 65 Bruce, P. G., Freunberger, S. A., Hardwick, L. J. & Tarascon, J.-M. Li-O₂ and Li-S batteries with high energy storage. *Nature materials* 11, 19-29 (2012).
- 66 Li, W. et al. High-performance hollow sulfur nanostructured battery cathode through a scalable, room temperature, one-step, bottom-up approach. *Proceedings of the National Academy of Sciences* 110, 7148-7153 (2013).
- 67 Guo, J., Xu, Y. & Wang, C. Sulfur-Impregnated Disordered Carbon Nanotubes Cathode for Lithium-Sulfur Batteries. *Nano Letters* 11, 4288-4294, doi:10.1021/nl202297p (2011).
- 68 Zhang, W. et al. A Li⁺-conductive microporous carbon-sulfur composite for Li-S batteries. *Electrochimica Acta* 87, 497-502, doi:10.1016/j.electacta.2012.09.086 (2013).
- 69 Xin, S., Guo, Y.-G. & Wan, L.-J. Nanocarbon networks for advanced rechargeable lithium batteries. *Accounts of chemical research* 45, 1759-1769 (2012).
- 70 Zhou, X., Wan, L. J. & Guo, Y. G. Binding SnO₂ Nanocrystals in Nitrogen-Doped Graphene Sheets as Anode Materials for Lithium-Ion Batteries. *Advanced Materials* 25, 2152-2157 (2013).

- 71 Rong, J., Ge, M., Fang, X. & Zhou, C. Solution ionic strength engineering as a generic strategy to coat graphene oxide (GO) on various functional particles and its application in high-performance lithium–sulfur (Li–S) batteries. *Nano letters* 14, 473-479 (2013).
- 72 Fu, Y. & Manthiram, A. Orthorhombic bipyramidal sulfur coated with polypyrrole nanolayers as a cathode material for lithium–sulfur batteries. *The Journal of Physical Chemistry C* 116, 8910-8915 (2012).
- 73 Fu, Y. & Manthiram, A. Core-shell structured sulfur-polypyrrole composite cathodes for lithium-sulfur batteries. *Rsc Advances* 2, 5927-5929 (2012).
- 74 Seh, Z. W. et al. Sulphur–TiO₂ yolk–shell nanoarchitecture with internal void space for long-cycle lithium–sulphur batteries. *Nature communications* 4, 1331 (2013).
- 75 Ji, X., Lee, K. T. & Nazar, L. F. A highly ordered nanostructured carbon–sulphur cathode for lithium–sulphur batteries. *Nature materials* 8, 500-506 (2009).
- 76 Zheng, G., Yang, Y., Cha, J. J., Hong, S. S. & Cui, Y. Hollow carbon nanofiber-encapsulated sulfur cathodes for high specific capacity rechargeable lithium batteries. *Nano letters* 11, 4462-4467 (2011).
- 77 Jayaprakash, N., Shen, J., Moganty, S. S., Corona, A. & Archer, L. A. Porous Hollow Carbon@ Sulfur Composites for High Power Lithium–Sulfur Batteries. *Angewandte Chemie* 123, 6026-6030 (2011).
- 78 Li, X. et al. Optimization of mesoporous carbon structures for lithium–sulfur battery applications. *Journal of Materials Chemistry* 21, 16603-16610 (2011).

Chapter 2 Anti-solvent promoted self-assembled organic nanowires for high power density lithium ion batteries

2.1: Introduction

To satisfy the emerging large-scale applications of energy storage, new generation batteries should have high power and energy densities and long cycle life¹. In near term, new inorganic cathode and anode materials are being developed to increase their capacity. In long term, the next generation batteries were proposed to be made from inexpensive, renewable, and/or recyclable resources, via low energy consumption processes for energy sustainability with minimal environmental footprint². Among them, electrochemical active organic materials were proposed to be a competitive candidate as the alternative for the inorganic electrode material, due to their high theoretical capacity, low cost, sustainability, and environmental friendliness².

In general, organic electrode materials can be divided into three types, according to their different redox reactions. For the N-type organic electrode materials, the reaction is between its neutral state and negatively charged state (Conjugated carbonyl^{3,4}). For the P-type organic electrode materials, the reaction is between its neutral state and positively charged state (Conjugated thioether⁵). There are also bipolar organic electrode materials, for which can be either reduced to negatively charged state or oxidized to positively charged state (Nitroxyl radical^{6,7}). Among all those organic electrode materials, N type conjugated carbonyl based materials such as pururin⁸, tribrominated trioxotriangulene⁹, perylenetetracarboxylic anhydride¹⁰, and other compounds¹¹⁻²¹ have been investigated as electrodes for Li-ion batteries, and some organic materials can also be used for Na-ion battery electrodes^{22,23}. Conjugated carbonyl compounds are not only the earliest type of

organic electrode materials, but also the most attractive and fruitful research field at present. Dissolution of the organic compounds in the electrolyte and low electronic conductivity are the major challenges to obtain stable electrochemical performance. Recently, it has been reported that the solubility of organic electrode materials could be reduced by increasing their polarity via salt formation²⁴ and can be further reduced by increasing the salt concentration of the electrolyte²⁵. Except for conducting polymers, nearly all other electrochemical active materials are electrical insulators, which largely prevented the full utilization and high rate performance of the active materials, even with 30% conductive carbon addition. It has been demonstrated that fabrication of nanostructure can play an important role in improving the performance of Lithium ion battery, because the Lithium ion diffusion path is dramatically decreases. Besides, Nanoparticles have large surface areas and fast electron and Li ion diffusion rate which are also beneficial for the operation of Lithium ion battery. For example, organic $\text{Li}_4\text{C}_8\text{H}_2\text{O}_6$ nanosheets have shown better cycling stability and rate performance than its bulk material²⁶. However, the lithiation induced strain in electrodes that can result in high stress, fracture, and capacity loss, which is common for inorganic electrode material (e.g. Si), has not been reported for organic electrode. Since capability for strain relief of one material is highly size dependent, in order to study whether lithiation induced strain was also contributed to cracks and capacity loss in organics materials; an assembly method needs to be developed to be able to controllably fabricate organic active materials with difference sizes for electrode material fabrication.

Croconic acid disodium salt (CADS) has a cyclopentene backbone with three carbonyl groups, and two of them are connected by a conjugated chemical bond as shown

in Fig. 2.1. The two carbonyl groups in CADS can participate in the reversible reaction with lithium ions²⁷, providing a theoretical capacity of 288 mAh g⁻¹. Anti-solvent crystallization assembly method was introduced for the controlled fabrication of CADS wires with different sizes. Besides, various conductive carbon materials were introduced as the seeding templates and external nucleus to promote heterogeneous crystallization during CADS precipitation in the mixed solvent, in order to further increase the overall conductivity of the resulting structures. Diameter size of 150nm, 4μm, and 10μm of CADS wires were chosen as the representatives to investigate the size effect on the battery performance of organic electrodes. The experiment results demonstrated that CADS nanowires with the diameter of 150 nm exhibit superior capacity, rate capability, and cycling stability. The theoretical calculation for lithiation and delithiation of CADS suggests that sodium ions in CADS will be gradually replaced by lithium ions during the lithiation and delithiation of CADS electrode, which is confirmed by Inductively Coupled Plasma test. Since Li croconate has a more stable crystal structure than Na croconate, the formation of Li croconate further enhances the cycling stability of CADS electrode. To our best knowledge, CADS nanowires demonstrate one of the best battery performances for reported organic compounds in terms of cycling stability and rate performance at a low carbon content.

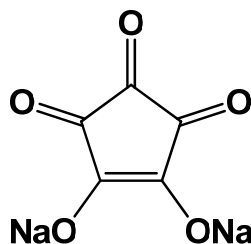


Fig. 2.1. Molecular structure of croconic acid disodium salt.

2.2 Results and discussion:

2.2.1: Self assemble of CADS from anti-solvent crystallization with and without external nucleus

Precipitation occurs when an anti-solvent (a solvent in which the product is insoluble in) is added, drastically reducing the solubility of the desired product in the new mixed solvent system²⁸. In our current system, CADS is highly soluble in water; however, it is not soluble in acetone. Precipitation of CADS occurs when large amount of acetone was added into CADS water solution due to the oversaturation of CADS in the acetone/water mixed solvent. The schematic drawing of the fabrication process is shown in Fig.2.2.1.1. The growth of CADS nanowires is driven by reducing the solubility of CADS, when acetone was added into CADS aqueous solution. Under bath sonication, CADS starts to crystallize within a few minutes, due to its poor solubility in the water/acetone mixture solvent. During crystallization, the CADS molecules self-assemble into nanowires, possibly due to π - π interaction between CADS molecules²⁹.

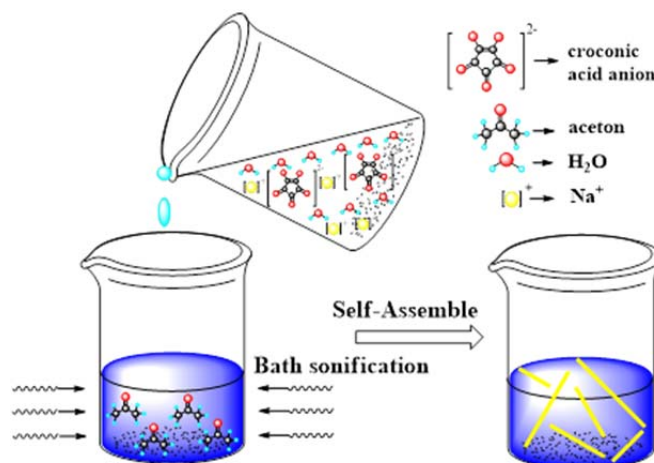


Fig. 2.2.1.1: schematic drawing of anti-solvent crystallization

A robust wire structure was always obtained when acetone was employed as the poor solvent. The concentration effect of the CADS water solution was studied when the volume ratio of water and acetone was fixed. In general, the diameter of CADS wires can be manipulated by tuning the concentration of CADS in aqueous solution. As shown in Fig. 2.2.1.2, CADS nanowires with average diameters of 150nm, 250nm, 500nm and 800nm were obtained with the concentration of CADS aqueous solution of 0.2mg/ml, 0.4mg/ml, 0.8mg/ml and 1mg/ml, respectively. The lower concentration CADS aqueous solution yields thinner CADS nanowires.

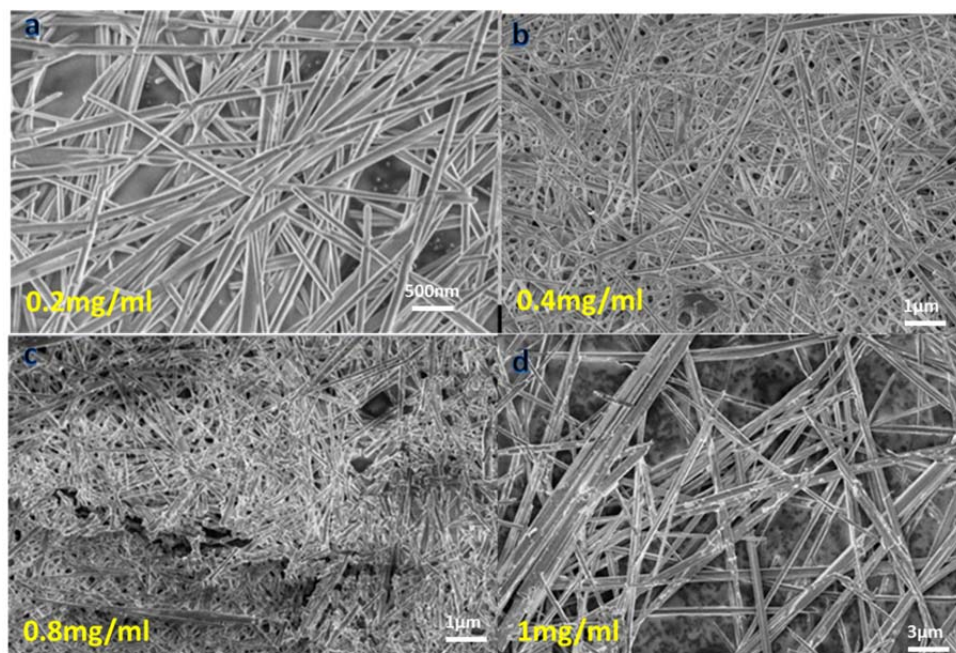


Fig.2.2.1.2 SEM images 200 μ l of a)0.2mg/ml; b)0.4mg/ml; c)0.8mg/ml; d)1mg/ml of CA was added into 12ml of Acetone

Different anti-solvents also influence the shape and size of the assembled morphology of CADS. For example, when acetonitrile was employed as the anti-solvent mixture of microsize rod and nanowire was obtained as shown in Fig.2.2.1.3 a. Similar to acetone, uniform nanowires were obtained when tetrahydrofuran (THF) was introduced as the anti-solvent(Fig.2.2.1.3 b). In the case of dimethylformamide (DMF), extremely long wires were obtained; however they were not uniform in diameters. More interestingly, the obtained nanowires orient themselves as fish bone configurations (Fig.2.2.1.3 c). When acetonitrile/chloroform mixture(volume ratio 3:1) was used, microrod with average diameter of 2 μ m was observed as the sole product. The size, shape, and uniformity observed for different antisolvents are mainly determined by the solubility of CADS in those solvent and the interaction between the good solvent and antisolvents.

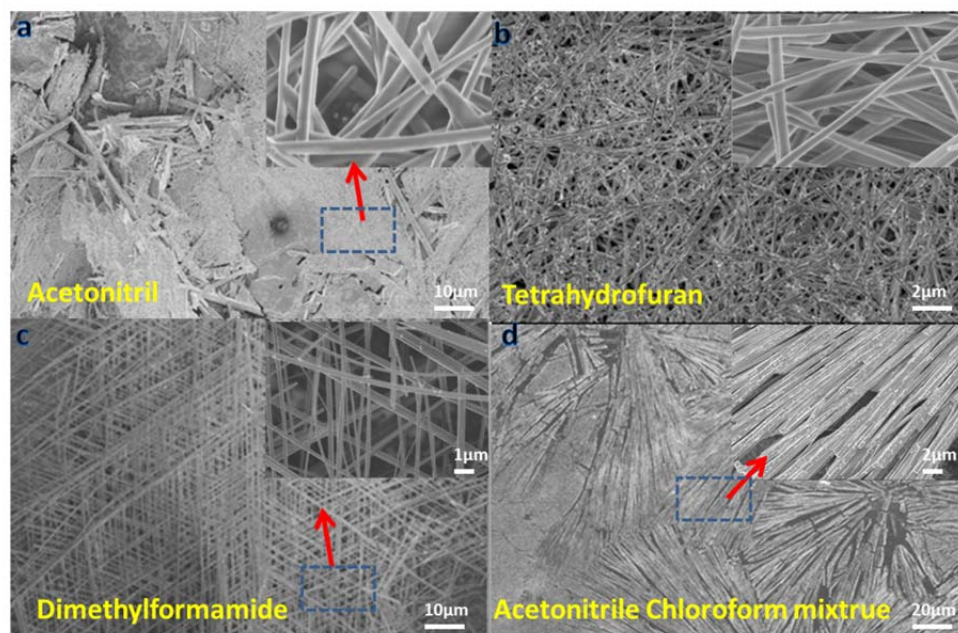


Fig.2.2.1.3 SEM images of CADS product from different poor solvent system a Acetonitril; b Tetrahydrofuran; c Dimethylformamide and d Acetonitrile/Chloroform mixture(volume ratio 3:1)

Heterogeneous crystallization will be promoted when foreign nucleus was introduced prior to the precipitation of the desired product³⁰. Current electrode preparation is involved mechanically mixing of polymer binder and carbon black as the conductive additive with the electroactive material. Recently, various carbon nanotubes and graphene materials have been explored to improve battery performance taking advantage of their high conductivity and unique shapes³¹⁻³⁴. If these conductive carbon nanomaterial was employed as the seeding template and external nucleus for the crystallization of CADS, a better mixing of the conductive carbon and the electrochemical active CADS is expected³⁵. As a result, the overall conductivity of the electrode materials should be increased, which will be beneficial for the battery rate performance.

We studied CADS morphology changes when microwave-enabled low oxygen graphene nanosheets (ME-LOGr)³⁶, multi-walled carbon nanotubes (MWCNT), nitrogen doped graphene quantum dots (NQD)³⁷, and carbon black (CB) were introduced as seeding templates and external nucleus for the CADS growth. ME-LOGr are two dimensional with lateral diameter of 10 ± 4 nm and an average thickness of 0.75 ± 0.23 nm. ME-LOGr are highly electrically conductive since they have limited amounts of oxygen-containing groups. MWCNT are highly conductive one dimensional carbon materials with average length around 400nm and average diameter of 20nm. Nitrogen doped graphene quantum dots, with lateral diameter of 10 ± 3 nm and an average thickness of 0.80 ± 0.21 nm, was obtained from bottom up reaction of citric acid and urea under microwave irradiation. Nitrogen atoms were introduced on the graphene basal plane such as graphitic nitrogen, pyridinic nitrogen and pyrrolic nitrogen. They also have oxygen rich functional group mainly distributed at the graphene edges. Therefore, the NQD are electrically insulating. Carbon black is the produced from the incomplete combustion of heavy petroleum products. These particle like carbon materials are high conductive with an average size of 50nm. They are electrochemically inactive and widely employed as the conductive carbon for the fabrication of electrode of Lithium ion battery.

Without adding external nucleus, the smallest diameter of CADS nanowires can be reached is around 150 nm (Fig.2.2.1.2 a). With the introduction of ME-LOGr nanosheets in the system prior to CADS crystallization, the average diameter of the final product is around 100 nm with minimum diameter of 20 nm (Fig.2.2.1.4 a), which is much thinner than the smallest ones achieved without seeding templates. When 1 D MWCNTs were introduced, the resulted CADS wires has similar average diameters as the ones achieved

without seeding templates, while they are relatively long (up to $30\mu\text{m}$). Very interesting, we also found that these nanowires well aligned in the same direction with several MWCNTs wrapping around some of the nanowires. (Fig.2.2.1.4 b). When NQDs were employed, uniform nanowires with average diameter of 50nm were obtained (Fig.2.2.1.4 c). When the commonly used conductive additive for lithium ion battery – carbon black – was used, the final product was not very uniform in size and shape (Fig.2.2.1.4 d). This might be due to the poor dispersity of CB in acetone, due to the lack of oxygen containing functional groups, large amount of CB aggregates were observed by SEM. Thus, it cannot serve as an effective nucleus to promote the heterogeneous crystallization.

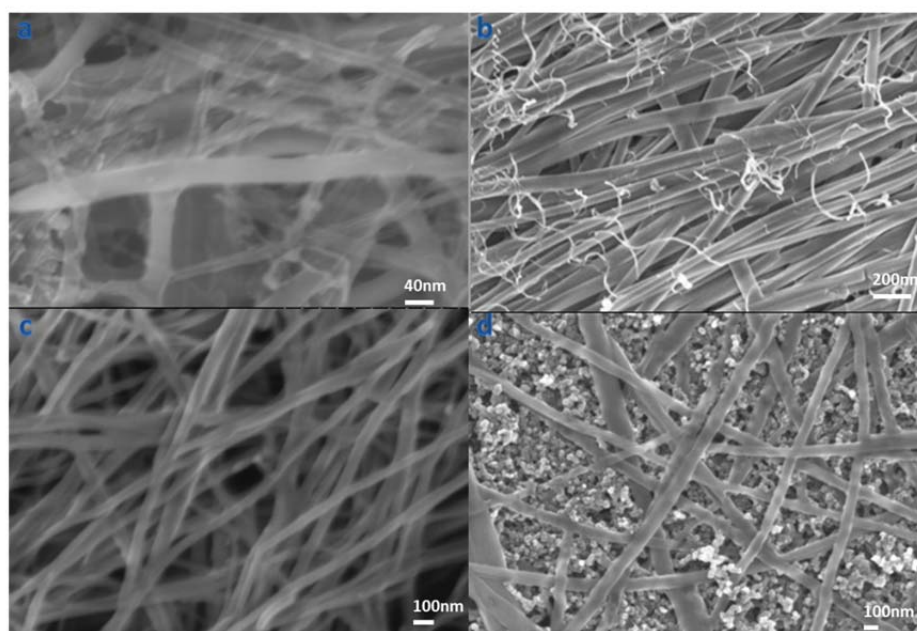


Fig.2.2.1.4 SEM images of CADS products with different carbon materials as seeding template: a ME-LOGr; b MWCNT; c NQD, and d CB.

2.2.2 Electrochemical evaluation of self-assembled organic nanowires as cathode material for Lithium ion battery

Crystal CADS micropillars with the width of 10 μm and length longer than 100 μm (Fig. 2.2.2.1 a) were obtained by directly recrystallizing CADS from water, and are used as control samples. Due to the insulating nature of CADS, the large particle size will significantly increase the transportation resistance of Li-ion and electron in the CADS micropillars. The large size and small surface area of CADS micropillars also result in poor contact between CADS and conductive carbon, thus remarkably reducing the charge transfer reaction kinetics. To improve the lithiation/delithiation kinetics, CADS microwires with an average diameter of about 4 μm (Fig. 2.2.2.1 b) and CADS nanowires with a mean diameter about 150 nm (Fig. 2.2.2.1 c & d) were fabricated at room temperature, using anti-solvent crystallization method.

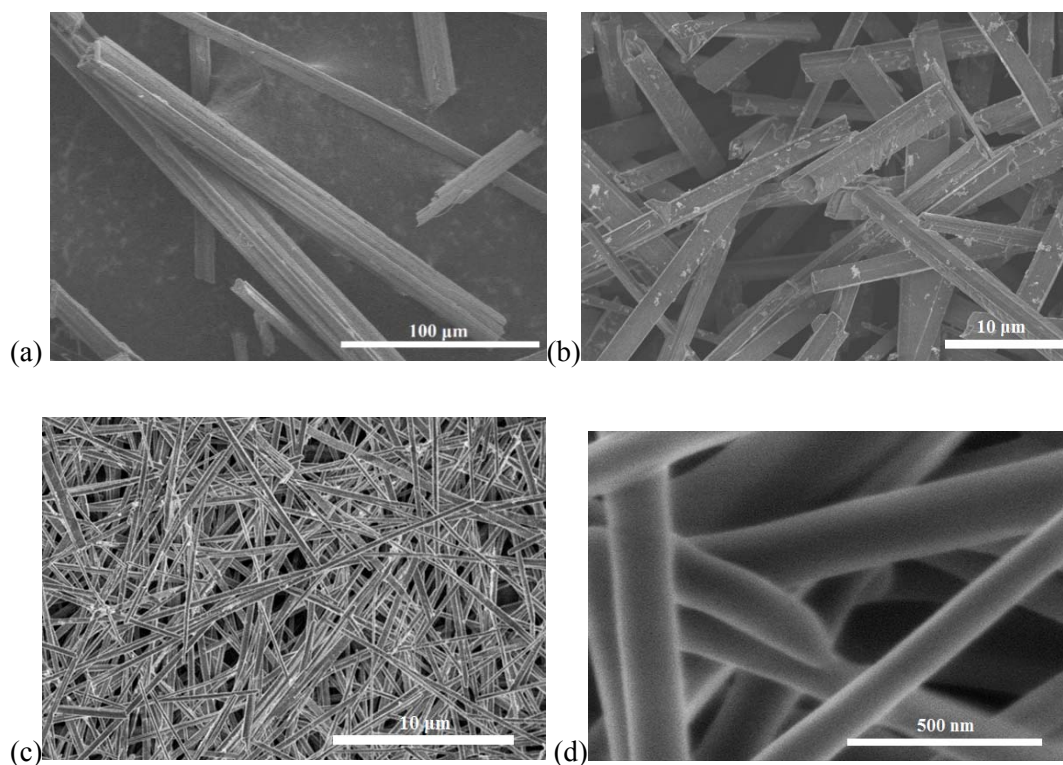


Fig 2.2.2.1. SEM images for CADs micropillar (a), CADs microwire (b) and CADs nanowire (c, d).

The crystal structures of three CADs samples were identified by the X-ray diffraction (XRD) method. The XRD patterns shown in Fig. 2.2.2.2, reveal that the CADs micropillar, CADs microwires, and CADs nanowires have the same crystal structure. No impurity peak is observed in these three CADs samples. The fact that the peak intensity of CADs nanowires is stronger than that of CADs micropillars and CADs microwires, revealed that CADs nanowires have high crystallinity and relatively uniform crystal size.

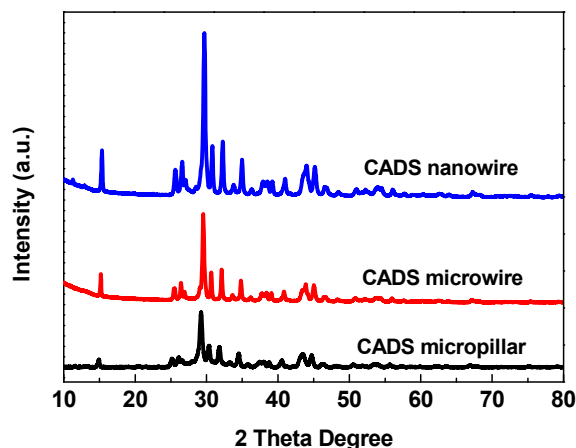


Fig. 2.2.2.2. XRD patterns of CADS micropillars, CADS microwires and CADS nanowires.

The charge and discharge profiles for CADS micropillars, CADS microwires, and CADS nanowires in the second cycle were measured at a current density of 0.2 C (1 C is defined as 288 mA g^{-1}) and are shown in Fig. 2.2.2.3 a. The lithiation potential decreases and delithiation potential increases as the size of CADS wires increases. The cyclic voltammetry (CV) of three CADSs with different diameters in Fig. 2.2.2.3 b-d shows a peak at 1.6 V with a small shoulder at 2.1 V in lithiation, and a peak at 2.0 V with a small shoulder at 2.6 V in delithiation, demonstrating that CADS undergoes a two-step reaction with lithium ions. The two carbonyl groups connected by carbon-carbon double bond react with lithium ions step by step. The potential hysteresis (ΔV) between the cathodic peak and anodic peak is 0.62 V for CADS micropillars, 0.47 V for CADS microwires and 0.30 V for CADS nanowires. The lowest overpotential for CADS nanowires indicates its better reversibility of the redox reaction than CADS micropillars and CADS microwires. The increase of potential hysteresis with wire size also confirms that lithiation/delithiation kinetics decreases with the increase of wire size. The equilibrium potentials of CADS are estimated by averaging the lithiation and delithiation potential.

The equilibrium lithiation potentials of CADS are 1.8 V and 2.35 V. As shown in CV curves in Fig. 2.2.2.3, the lithiation peak potential slightly increases to more positive value with lithiation and delithiation cycles.

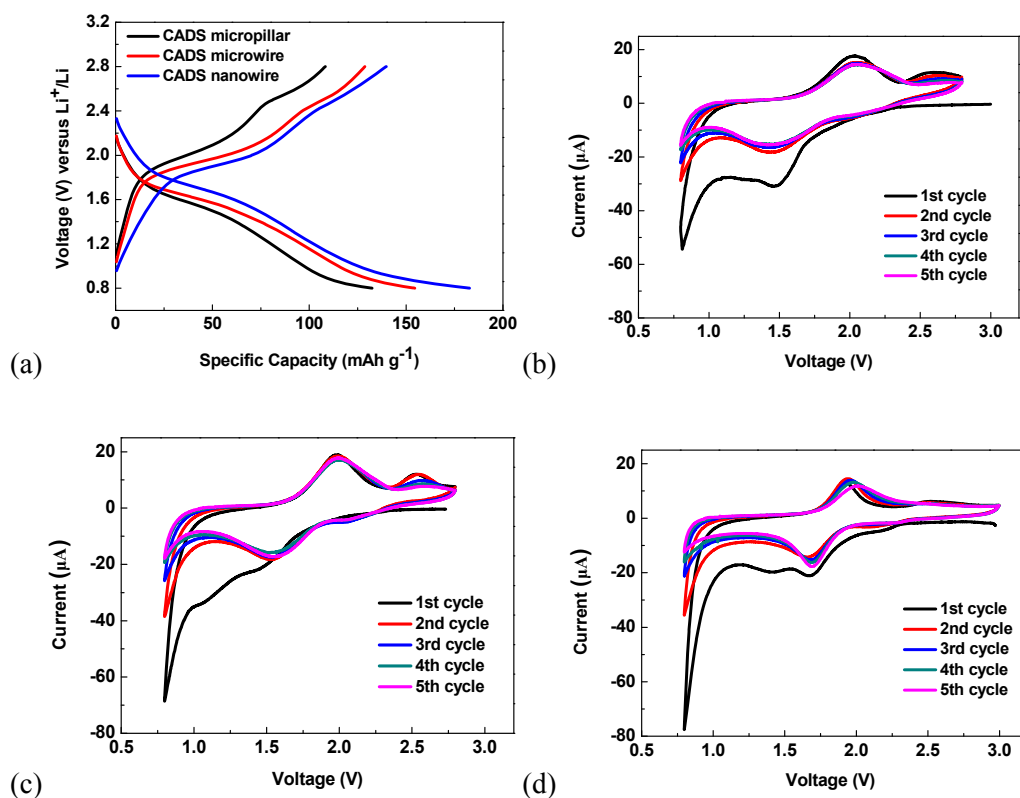


Fig. 2.2.2.3. Electrochemical performance of CADS micropillars, CADS microwires and CADS nanowires. (a) Charge and discharge curves of CADS micropillars, CADS microwires and CADS nanowires for the second cycle; Cyclic voltammograms for CADS micropillars (b), CADS microwires (c), CADS nanowires (d).

To explore the mechanism for two-step reaction and potential shift, the first principle DFT calculation is applied to calculate the lithiation process. Table 2.2.2.1 collects the values of the total electronic bonding energy of various species involved in the reduction of CADS. Table 2.2.2.2 collects the calculated reduction potential of the CADS with respect to a lithium electrode potential.

TABLE 2.2.2.1: Total bonding energy and HOMO-LUMO gap in eV.

Compound	Bonding Energy (eV)	Homo-Lumo gap (eV)
Na ₂ CA	-96.2954	3.39
Li ₂ CA	-98.4320	3.88
Li ₃ CA	-101.4177	2.13
Na ₂ LiCA	-99.1397	1.25
Na ₃ LiCA	-100.6417	0.61
Na ₂ Li ₂ CA	-101.9261	0.96
Li ₄ CA	-104.3329	1.94
Li	-0.4295	

TABLE 2.2.2.2: Summary of the calculated electrochemical potentials from the energies in Table 2.2.2.1.

Electrochemical process	Potential	# of electrons
$\text{Na}_2\text{CA} + \text{Li} \rightarrow \text{Na}_2\text{LiCA}$	2.42	1
$\text{Na}_2\text{LiCA} + \text{Li} \rightarrow \text{Na}_2\text{Li}_2\text{CA}$	2.36	1
$\text{Na}_2\text{CA} + 2\text{Li} \rightarrow \text{Na}_2\text{Li}_2\text{CA}$	2.39	2
$\text{Li}_2\text{CA} + \text{Li} \rightarrow \text{Li}_3\text{CA}$	2.56	1
$\text{Li}_3\text{CA} + \text{Li} \rightarrow \text{Li}_4\text{CA}$	2.49	1
$\text{Li}_2\text{CA} + 2\text{Li} \rightarrow \text{Li}_4\text{CA}$	2.52	2

Fig. 2.2.2.4 schematically reports the energy levels of Na and Li croconate for the three reduced forms considered. The potentials in Table 2.2.2.2 indicate that the one-electron and the two-electron reduction of CADS occur at very similar potentials. The sequential one-electron reductions are estimated to be 2.42 V and 2.36 V, which is higher than the equilibrium potential demonstrated by CV scans (2.35 V and 1.8 V). The large potential difference (2.36-1.8=0.56V) in second step reaction is probably attributed to the strain overpotential, induced by the volume expansion at high lithiation levels. A large strain overpotential of 0.6 V was reported for lithiation of Sn^{38} . Due to the low strain at low lithiation level, the calculated potential in the first step reaction is similar to

measured potential in CV. However, the calculations are unable to ascertain whether the electrochemical potentials result from a concerted two-electron process or two sequential one-electron processes. Analyzing the overall stability of the sodium and lithium croconate indicates (see Table 2.2.2.1) that lithium croconate forms a more stable crystal than the sodium salt. Thus, it is possible that the CADS undergo a chemical exchange from sodium croconate to lithium croconate. For this reason, additional simulations were carried out for the reduction of lithium croconate. The simulations showed that the reduction potential for Lithium croconate is 2.56 V and 2.49 V for the single one-electron processes, respectively. Thus, if a counter ion exchange occurs during the CV scans, the reduction potential should slightly increases, which is in well agreement with CV scans in Fig. 2.2.2.3. The simulations qualitatively reproduce the potentials determined experimentally and predict a possible Sodium-Lithium exchange during the lithiation and delithiation of CADS electrode. Such prediction is further confirmed by Inductively Coupled Plasma (ICP) test. A fresh CADS electrode and a CADS electrode (after first cycle) are dissolved in water separately, and then Li^+ and Na^+ concentration in water was measured by ICP. The result shows that the concentrations of Li^+ and Na^+ in fresh electrode are 0 and 0.135 mg L^{-1} , respectively, while the concentrations of Li^+ and Na^+ in cycled electrode are 0.103 mg L^{-1} and 0.020 mg L^{-1} , demonstrating that most of sodium ions in CADS are exchanged by lithium ions.

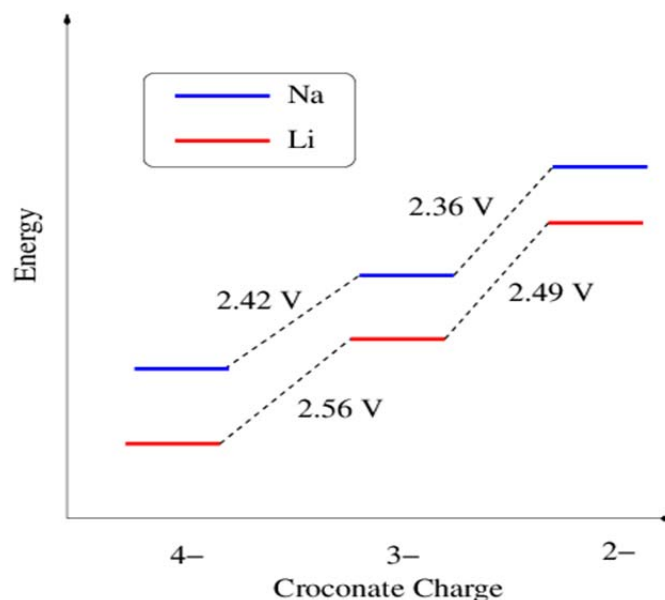


Fig. 2.2.2.4. Calculated energy levels of NaCA and LiCA. Potentials shown are referenced to the Li electrode.

The cycling performance of CADS electrodes is shown in Fig. 2.2.2.5 a. The specific capacities of CADS micropillars, CADS microwires and, CADS nanowires decrease a little in the first 10 cycles, and then it becomes very stable for CADS micropillars, and even begin to increase back to original capacity at 110 cycles for CADS nanowires, and slightly lower than initial capacity at 110 cycles for CADS microwires, which are consistent with CV results. This kind of cycling behavior is also observed in nano-Si/C composite³⁹. At initial cycles, the electrolyte does not fully penetrate to the entire electrode, leading to large overpotential and slow kinetics. Upon cycling, the large volume expansion and shrinkage of CADS increase the porosity of the CADS electrodes, allowing electrolyte penetrate to the entire electrode, thus shortening the ion diffusion pathway and lowering the overpotential. The faster kinetics enhances the utilization of organic electrode, resulting in capacity increase. The reversible capabilities of CADS micropillars, CADS microwires, and CADS nanowires measured at a current density of

0.2 C are 85 mAh g⁻¹, 132 mAh g⁻¹, and 177 mAh g⁻¹, respectively. CADS nanowires retain their initial capacity after 110 deep charge/discharge cycles.

Since CADS is an insulating material, lithium ions and electrons cannot be easily transported into the inside of bulk CADS materials. However, the smaller size and larger surface area of CADS nanowires enable more CADS to react with lithium ions, and lithium ions can quickly transfer to inside of CADS, so the specific capacity and rate capability of CADS nanowires is much higher than that of CADS micropillars and CADS microwires. The rate capability of CADS micropillars, CADS microwires, and CADS nanowires are shown in Fig. 2.2.2.5 b. With the current density increases from 0.1 C to 0.75 C, the specific capacity of CADS micropillars decreases rapidly from 125 mAh g⁻¹ to 7 mAh g⁻¹. Although the capacity of CADS microwires is still 48 mAh g⁻¹ at the current density of 0.75 C, the specific capacity of CADS microwires decreases from 160 mAh g⁻¹ to 11 mAh g⁻¹ when the current density increases from 0.1 C to 2 C, indicating the inferior rate performance of CADS microwires, due to the large diameter (~4 μm) of microwires. On the contrary, the smaller size and larger surface area of CADS nanowires can shorten the lithium ion diffusion length and enables better contact between CADS and conductive carbon. Therefore, CADS nanowires retain 50% of their initial capacity (200 mAh g⁻¹) subjected to the current density up to 6 C. After the current density returns to 0.1 C, the capacity of CADS nanowires recovers to its initial capacity, immediately. Hence, from the electrochemical performance of CADS micropillars, CADS microwires, and CADS nanowires, we can conclude that nanowire structure makes great contribution to the high capacity and high power density of CADS materials.

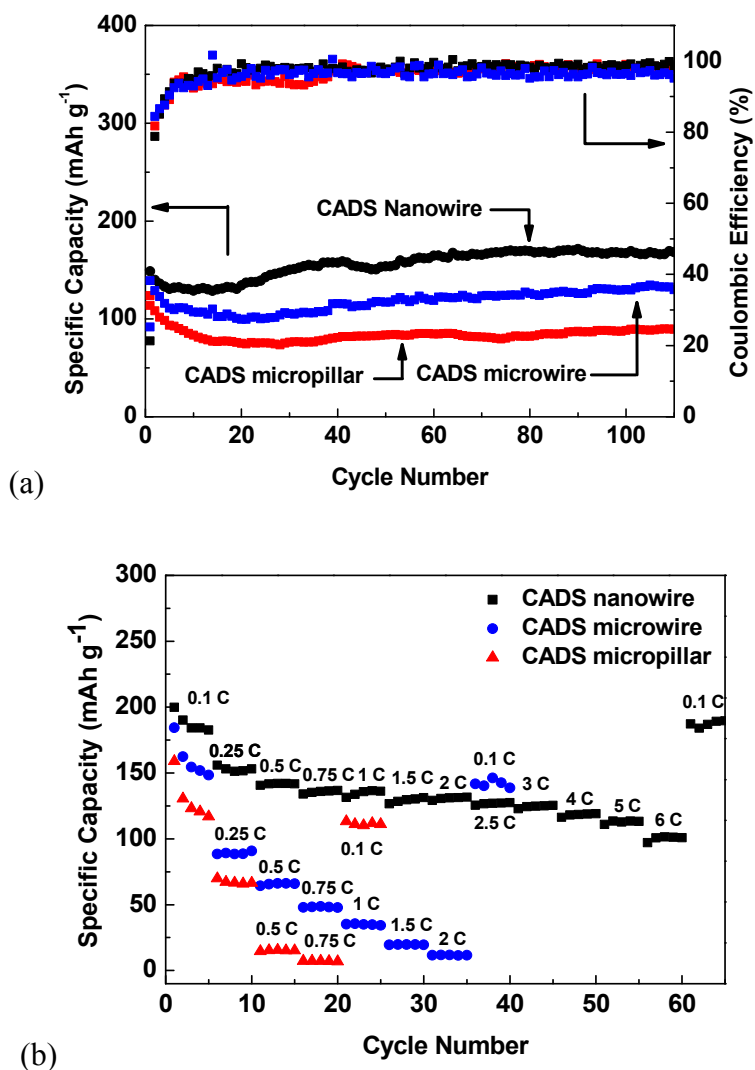


Fig. 2.2.2.5. Cycle life (a) and rate capability (b) of CADs micropillar, CADs microwire and CADs nanowire. (1 C is defined as 288 mA g⁻¹)

The reaction kinetics of CADs materials was investigated by using electrochemical impedance spectroscopy (EIS). The high frequency semicircle represents the interface resistance includes contact impedance or SEI impedance, and charge transfer impedance, while the low frequency line stands for ion diffusion resistance. As shown in Fig. 2.2.2.6, both the interface and diffusion impedances of CADs nanowires are significantly lower than that of CADs micropillars and CADs microwires, indicating the lower interface resistance and better kinetics of CADs nanowires. The interface resistance of CADs

nanowires is about 50 Ohm, while that for CADS micropillar electrode and CADS microwire electrode have much higher value of 300 Ohm and 750 Ohm, respectively. The impedance results confirm that the high capacity and superior rate capability of CADS nanowire is due to the large electrochemical reaction interface and short Li diffusion pathway.

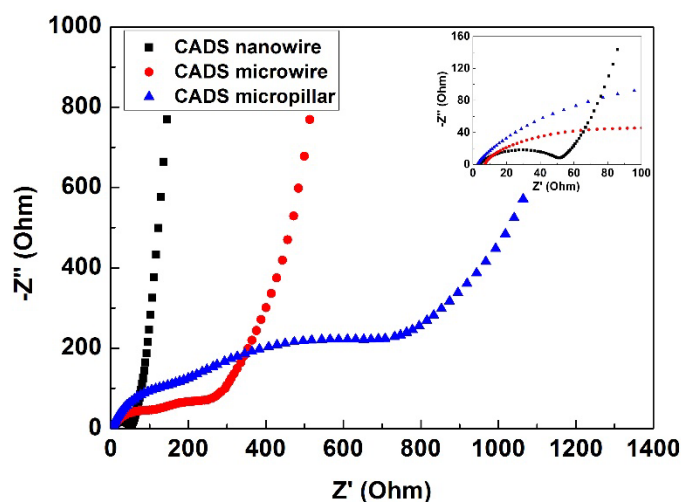
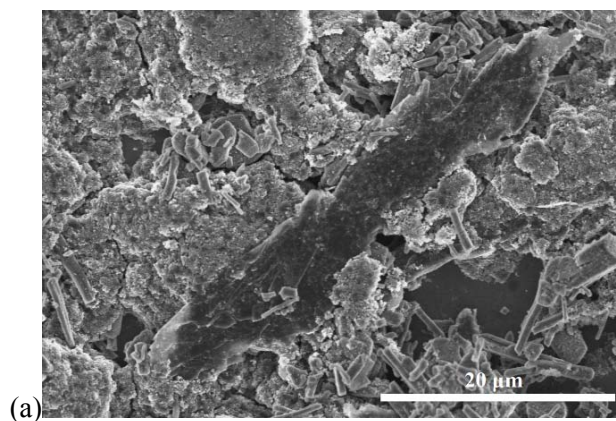


Fig. 2.2.2.6. EIS spectra for CADS micropillar electrode, CADS microwire electrode and CADS nanowire electrode. (The inset is magnification of the semi-circle of CADS Nanowire)

The morphology of CADS micropillar, CADS microwires, and CADS nanowires after 110 cycles were investigated by SEM. As shown in Fig. 2.2.2.7 a, several micro-size short rods can be found around the large size CADS micropillars, demonstrating severe pulverization which occurred after 110 charge/discharge cycles. The CADS microwires maintain their morphology after 110 cycles (Fig. 2.2.2.7 b), but few short CADS rods and microcracks (induced by the large strain during repeated charge/discharge cycles) can still be observed. Different from CADS microwires, CADS nanowires preserve their morphology after 110 cycles in Fig. 2.2.2.7 c, no cracks and pulverization can be observed. The good morphology maintenance of CADS nanowires enables its high

cycling stability. Graphitic illustration was also depicted in Fig. 2.2.2.8. During repeated lithiation/delithiation, CADS will gradually convert to croconic acid dilithium salt through ion exchange, as suggested by theoretical calculation and evidenced by the potential shift in CV scans and reduction of Na^+ concentration in cycled CADS electrode. More importantly, CADS nanowire with small size (150nm) and large surface area, can effectively avoid pulverization and enables stable contact between CADS and carbon black, providing high capacity, high rate capability and long cycling stability. Due to the large size of CADS microwire, large volume change exists and leads to the formation of cracks and microcracks, as evidenced by SEM images of cycled CADS microwires. The microcracks which lose contact with carbon black are not electroactive, resulting in capacity decline in the initial cycles. Therefore, nano-size CADS exhibits much better electrochemical performance than micro-size CADS.



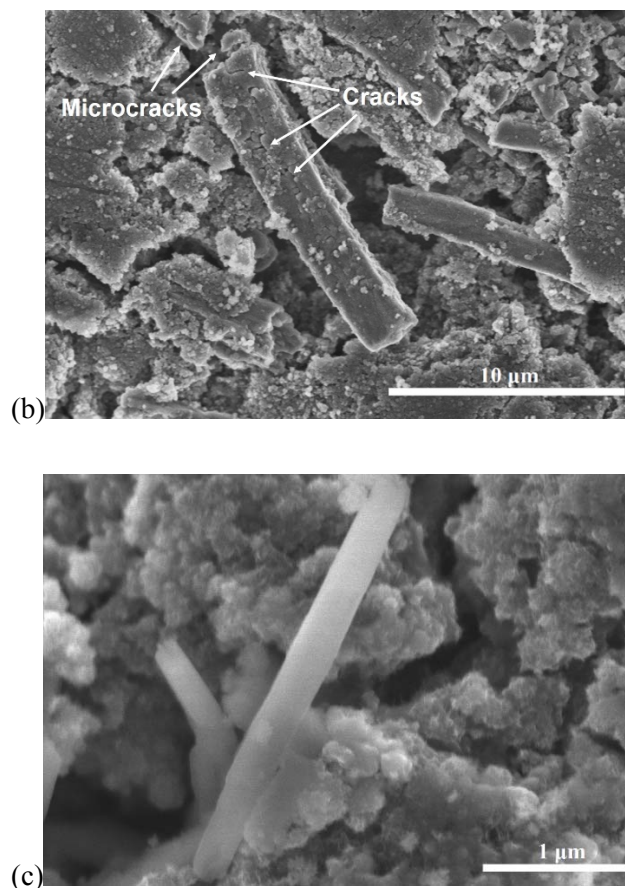


Fig. 2.2.2.7. SEM images for CADS micropillars (a), CADS microwires (b) and CADS nanowires (c) after 100 cycles.

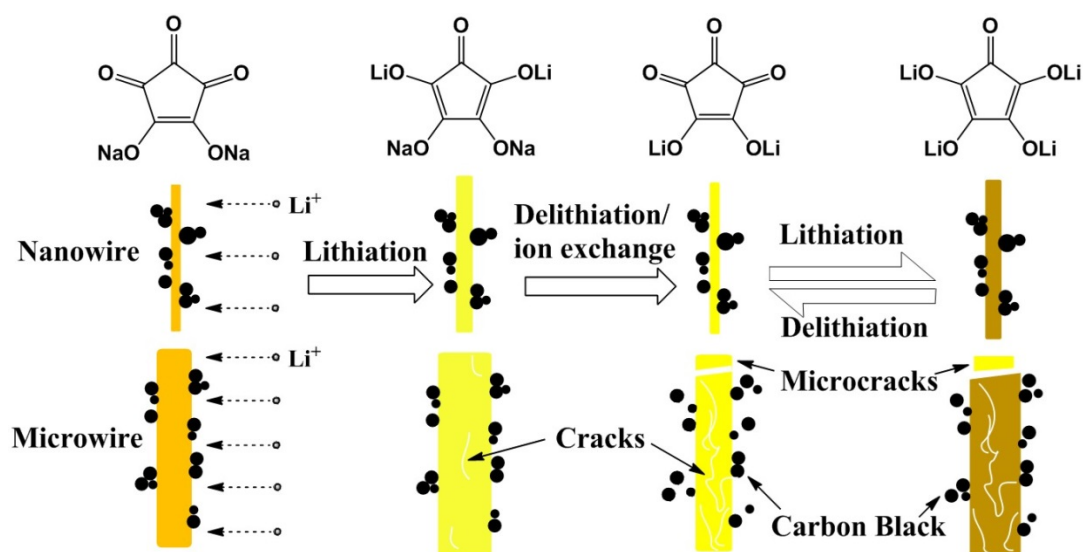


Fig. 2.2.2.8. Schematic illustration of lithiation/de-lithiation mechanism for croconic acid disodium salt.

2.3 Conclusion:

Anti-solvent assembly method was introduced (with and without external nucleus) to the fabrication of organic electrode materials with controlled size. The CADS wires were employed as the model compound to study the size effect of organic electrode materials. The CADS nanowires with small diameter and large surface area showed high capacity, long cycle life, and excellent rate capability, due to their short Li-ion and electron diffusion pathway, large surface area, and low strain. CADS nanowires retained their initial capacity after 110 deep charge/discharge cycles at a low current density of 0.2 C, and delivered a high capacity of 100 mAh g⁻¹ at 6 C. The theoretical calculation shows that the CADS wires gradually will change into a more stable lithium croconate through ion exchange process during lithiation/delithiation. The ion exchange process was confirmed by ICP method, which showed the high content of lithium ion and low content of sodium ion in the cycled CADS electrode. Since the nano-organic material exhibits superior electrochemical performance, our research work paves the way for further improvement of organic battery performance in the future studies.

2.4 Materials and methods:

Materials

Synthesis of Microwave-enabled low oxygen nano graphene (ME-LOGr)

0.2ml water and 20 mg of graphite were mixed with 7ml concentrated sulfuric acid and water in a round-bottom flask. The mixture was then swirled and cooled in an ice bath for approximately 5 mins. 2.8ml concentrated nitric acid was then added. The entire mixture is swirled and mixed for another 30 s and placed into the microwave reactor chamber.

The reaction mixture was subjected to microwave irradiation (300 W) for 30 s. Subsequently, the reaction was quenched with 200 mL of deionized water, filtered through an alumina anodic filter (0.02 μm pore size), and washed with 800 mL of deionized water. The cake on the membrane was then re-dispersed into water with 30 min of bath sonication. The dispersed product was then left undisturbed for five days to let the unexfoliated graphite particles precipitate out.

Synthesis of Nitrogen doped graphene quantum dots

0.21g of Citric Acid (1.1mmols) and 0.18g of Urea (3.5mmols) were dissolved in 1 ml water. The solution was then dried in the vacuum oven at 800⁰C for 2 hour, to remove the majority of water. The mixture was then put into the microwave reaction chamber (CEM, discover). Subsequently, the reaction mixture was subjected to microwave radiation (300W) for 40s. The orange brown powder obtained from the reaction was then dispersed in 25ml water via bath sonication. The quantum dots dispersion was then centrifuged at 8500 rpm for 15mins and the supernatant was collected for dialysis.

Fabrication of CADS nanowires:

The bulk materials were purchased from Sigma Aldrich. 0.75 mL CADS aqueous solution with a concentration of 0.2 mg mL⁻¹ was added into 12 mL acetone in the bath sonication. After 10 minutes of sonication, the yellow precipitation was collected through filtration. Several bottles of above sample were collected for further characterization. CADS microwires were prepared with the same method, (but is not a formal word normally) a higher concentration (2 mg mL⁻¹) of CADS aqueous solution was used.

Fabrication of CADS micropillars: the as received CADS powder was directly dissolved in water to prepare 5mg/ml CADS water solution. Then, the 5mg/ml CADS water solution was cast on the stainless steel foil and kept at room temperature for 48 hours to dry. The resulting sample was collected for further characterization. For the seeding sample, the carbon materials (CNT, ME-LOGr, NQD, and carbon black) were dispersed in acetone with the concentration of 0.1mg/ml. 200 μ l of 0.2mg/ml CA/water solution was added into 12ml of acetone with the existing of carbon material. Sample was collected with filtration for further characterizations. Multi-wall carbon nanotubes (MWCNT) were kindly supplied by Cnano Technology Limited. Carbon black was purchase from MTI Corporation.

Characterizations: Scanning electron microscopy (SEM) image was taken by Hitachi S4800 analytical ultra-high resolution SEM (Japan). X-ray diffraction (XRD) pattern was recorded by Bruker Smart1000 (Bruker AXS Inc., USA), using CuK α radiation.

Inductively Coupled Plasma test: Inductively Coupled Plasma (ICP) test was performed on PerkinElmer Optima 4300 DV ICP-Optical Emission Spectrometer. Both the fresh electrode and cycled electrode were dissolved in deionized water by using bath sonication. The cycled electrode was immersed in diethyl carbonate for 48 hrs to remove the LiPF₆ salt prior to ICP test. Six standard solutions with the Li⁺ or Na⁺ concentration of 0.0 mg L⁻¹, 0.025 mg L⁻¹, 0.05 mg L⁻¹, 0.1 mg L⁻¹, 0.25 mg L⁻¹, and 0.5 mg L⁻¹ were prepared to obtain a standard relationship between peak intensity and the concentrations of lithium ion and sodium ion, using ICP method. The concentration of lithium ion and sodium ion

in fresh electrode and cycled electrodes was obtained, using the standard relationship between peak intensity and the concentrations of lithium ion and sodium ion.

Electrochemical Measurements: The recrystallized CADS, CADS microwires and CADS nanowires were mixed with carbon black and Polyvinylidene fluoride (PVDF) binder to form slurry at the weight ratio of 70:20:10, respectively. The electrode was prepared by casting the slurry onto the aluminum foil, using a doctor blade, and dried in a vacuum oven at 100 °C overnight. The electrode was cut into circular pieces with diameter of 1.2 cm for coin cell testing, with the area mass loading of $\sim 0.8 \text{ mg cm}^{-2}$. Li ion batteries were assembled with lithium metal as the counter electrode, 1 M LiPF_6 in a mixture of ethylene carbonate/diethyl carbonate (EC/DEC, 1:1 by volume) as the electrolyte, and Celgard®3501 (Celgard, LLC Corp., USA) as the separator. Electrochemical performance was tested, using Arbin battery test station (BT2000, Arbin Instruments, USA). Capacity was calculated on the basis of the mass of CADS micropillar, CADS microwires or CADS nanowires. Cyclic voltammogram were recorded at a scan rate of 0.1 mV/s between 0.8 – 2.8 V, using Solatron 1260/1287 Electrochemical Interface (Solatron Metrology, UK). Impedance analysis was also performed by Solatron 1260/1287 Electrochemical Interface.

Calculations were performed with the Amsterdam Density Functional (ADF) suite of software, using a triple-zeta with polarization basis set. ADF uses Slater-type orbitals (STOs), as opposed to most quantum-chemistry codes which use Gaussian-type orbitals. STOs feature correct decay at long distances and accurately describe the nuclear-electron cusp.

2.5 References:

- 1 Song, Z. & Zhou, H. Towards sustainable and versatile energy storage devices: an overview of organic electrode materials. *Energy & Environmental Science* **6**, 2280, doi:10.1039/c3ee40709h (2013).
- 2 Liang, Y., Tao, Z. & Chen, J. Organic Electrode Materials for Rechargeable Lithium Batteries. *Advanced Energy Materials* **2**, 742-769, doi:10.1002/aenm.201100795 (2012).
- 3 Oyama, N., Sarukawa, T., Mochizuki, Y., Shimomura, T. & Yamaguchi, S. Significant effects of poly(3,4-ethylenedioxythiophene) additive on redox responses of poly(2,5-dihydroxy-1,4-benzoquinone-3,6-methylene) cathode for rechargeable Li batteries. *Journal of Power Sources* **189**, 230-239, doi:http://dx.doi.org/10.1016/j.jpowsour.2008.09.052 (2009).
- 4 Han, X., Chang, C., Yuan, L., Sun, T. & Sun, J. Aromatic Carbonyl Derivative Polymers as High-Performance Li-Ion Storage Materials. *Advanced Materials* **19**, 1616-1621, doi:10.1002/adma.200602584 (2007).
- 5 Liu, L. *et al.* Porous polythiophene as a cathode material for lithium batteries with high capacity and good cycling stability. *Reactive and Functional Polymers* **72**, 45-49, doi:http://dx.doi.org/10.1016/j.reactfunctpolym.2011.10.006 (2012).
- 6 Oyaizu, K. & Nishide, H. Radical Polymers for Organic Electronic Devices: A Radical Departure from Conjugated Polymers? *Advanced Materials* **21**, 2339-2344, doi:10.1002/adma.200803554 (2009).
- 7 Nakahara, K., Oyaizu, K. & Nishide, H. Organic radical battery approaching practical use. *Chemistry Letters* **40**, 222-227 (2011).
- 8 Reddy, A. L. M. *et al.* Lithium storage mechanisms in purpurin based organic lithium ion battery electrodes. *Scientific reports* **2** (2012).
- 9 Morita, Y. *et al.* Organic tailored batteries materials using stable open-shell molecules with degenerate frontier orbitals. *Nature materials* **10**, 947-951 (2011).
- 10 Han, X., Chang, C., Yuan, L., Sun, T. & Sun, J. Aromatic Carbonyl Derivative Polymers as High-Performance Li-Ion Storage Materials. *Advanced Materials* **19**, 1616-1621 (2007).
- 11 Song, Z., Zhan, H. & Zhou, Y. Polyimides: Promising Energy-Storage Materials. *Angewandte Chemie* **122**, 8622-8626 (2010).
- 12 Song, Z. *et al.* Polymer-graphene nanocomposites as ultrafast-charge and-discharge cathodes for rechargeable lithium batteries. *Nano letters* **12**, 2205-2211 (2012).
- 13 Genorio, B., Pirnat, K., Cerc-Korosec, R., Dominko, R. & Gaberscek, M. Electroactive Organic Molecules Immobilized onto Solid Nanoparticles as a Cathode Material for Lithium-Ion Batteries. *Angewandte Chemie International Edition* **49**, 7222-7224 (2010).
- 14 Senoh, H., Yao, M., Sakaebe, H., Yasuda, K. & Siroma, Z. A two-compartment cell for using soluble benzoquinone derivatives as active materials in lithium secondary batteries. *Electrochimica Acta* **56**, 10145-10150 (2011).
- 15 Han, X., Qing, G., Sun, J. & Sun, T. How many lithium ions can be inserted onto fused C6 aromatic ring systems? *Angewandte Chemie* **124**, 5237-5241 (2012).
- 16 Hanyu, Y. & Honma, I. Rechargeable quasi-solid state lithium battery with organic crystalline cathode. *Scientific reports* **2** (2012).
- 17 Walker, W. *et al.* Ethoxycarbonyl-based organic electrode for Li-batteries. *Journal of the American Chemical Society* **132**, 6517-6523 (2010).
- 18 Nokami, T. *et al.* Polymer-bound pyrene-4, 5, 9, 10-tetraone for fast-charge and-discharge lithium-ion batteries with high capacity. *Journal of the American Chemical Society* **134**, 19694-19700 (2012).

- 19 Kassam, A., Burnell, D. J. & Dahn, J. Lithiated 1, 4, 5, 8-Naphthalenetetraol Formaldehyde Polymer, An Organic Cathode Material. *Electrochemical and Solid-State Letters* **14**, A22-A23 (2011).
- 20 Pirnat, K. *et al.* Electrochemically stabilised quinone based electrode composites for Li-ion batteries. *Journal of Power Sources* **199**, 308-314 (2012).
- 21 Xu, W. *et al.* Factors affecting the battery performance of anthraquinone-based organic cathode materials. *Journal of Materials Chemistry* **22**, 4032-4039 (2012).
- 22 Pan, H., Hu, Y.-S. & Chen, L. Room-temperature stationary sodium-ion batteries for large-scale electric energy storage. *Energy & Environmental Science* **6**, 2338-2360 (2013).
- 23 Zhao, L. *et al.* Disodium Terephthalate (Na₂C₈H₄O₄) as High Performance Anode Material for Low-Cost Room-Temperature Sodium-Ion Battery. *Advanced Energy Materials* **2**, 962-965 (2012).
- 24 Armand, M. *et al.* Conjugated dicarboxylate anodes for Li-ion batteries. *Nature materials* **8**, 120-125 (2009).
- 25 Suo, L., Hu, Y.-S., Li, H., Armand, M. & Chen, L. A new class of solvent-in-salt electrolyte for high-energy rechargeable metallic lithium batteries. *Nature communications* **4**, 1481 (2013).
- 26 Wang, S. *et al.* Organic Li₄C₈H₂O₆ nanosheets for lithium-ion batteries. *Nano letters* **13**, 4404-4409 (2013).
- 27 Chen, H. *et al.* From Biomass to a Renewable LiXC₆O₆ Organic Electrode for Sustainable Li-Ion Batteries. *ChemSusChem* **1**, 348-355 (2008).
- 28 Adler, A. D., Longo, F. R., Kampas, F. & Kim, J. On the preparation of metalloporphyrins. *Journal of Inorganic and Nuclear Chemistry* **32**, 2443-2445 (1970).
- 29 Liu, H. *et al.* Morphological tuning and conductivity of organic conductor nanowires. *Nanotechnology* **18**, 495704 (2007).
- 30 Mendez-Villuendas, E. & Bowles, R. K. Surface Nucleation in the Freezing of Gold Nanoparticles. *Physical Review Letters* **98**, 185503 (2007).
- 31 Wang, S. *et al.* Graphene as Atomic Template and Structural Scaffold in the Synthesis of Graphene–Organic Hybrid Wire with Photovoltaic Properties. *ACS Nano* **4**, 6180-6186, doi:10.1021/nn101800n (2010).
- 32 Hirai, K. *et al.* Effects of volume strain due to Li–Sn compound formation on electrode potential in lithium-ion batteries. *Acta Materialia* **56**, 1539-1545 (2008).
- 33 Magasinski, A. *et al.* High-performance lithium-ion anodes using a hierarchical bottom-up approach. *Nature materials* **9**, 353-358 (2010).

Chapter 3. Micelle formation of graphene quantum dots and its application as the soft template for the growth of nanomaterial with control size and shape for Lithium ion battery

3.1 Introduction

Development of high energy rechargeable Lithium ion battery has attracted tremendous attention due to the increasing energy demand in the application of portable electronics and electrical vehicles¹⁻³. The currently used inorganic cathode materials (e.g., LiCoO_2 and LiFePO_4) for Lithium ion batteries are restricted by their theoretical specific capacity, making it difficult to improve their energy density. Extensive efforts have been devoted into investigation of alternative cathode materials with high energy density. Among them, element sulfur is an intriguing candidate with theoretical capacity of 1,673mAh/g, more than five times higher than the commercial Lithium transition metal oxide cathode. In addition, element sulfur is naturally abundant, low cost with low toxicity^{4,5}. Current challenges for the practical use of Li-S technology including: poor electronic conductivity of element sulfur; heavy dissolution of intermediate polysulfide and large volume expansion during charge/discharge cycles⁶⁻⁸. In order to alleviate the above problems, major efforts have been focused on fabrication of core-shell structure, using physical barrier to restrain element sulfur and its dissolvable polysulfide intermediate. For example, nanostructured carbon materials (mesoporous carbon, Carbon nanotube and graphene), conducting polymers (polyaniline, polypyrrole, and poly(3,4-

ethylenedioxythiophene) and metal oxide (TiO_2)⁹⁻¹³ have been successfully employed for sulfur cathode fabrication with satisfactory cycle stability. Despite the success in obtaining stable performance in the short term, the sulfur loading is relatively low and the fabrication process is complicated. The construction of core shell structure always involved with multiple steps which are time and energy consuming.

Graphene oxide can be viewed as novel two dimensional amphiphile since it can be easily dispersed in water and certain level of hydrophobic domain can be directly visualized on its basal plane using high resolution TEM¹⁴. Jiaxin Huang et al have reported that graphene oxide can be used as colloidal surfactant to stabilize oil water interface and dispersing agent to solubilize hydrophobic carbon nanotube in water¹⁵. It has also been demonstrated that the liquid crystal phase can be formed in GO aqueous dispersion, which revealed that GO sheets can orient themselves in a certain manner (Nematic phase) in aqueous solution. The property of graphene oxide is highly size dependent. As the size of the graphene oxide decreases, the fraction ratio of GO required for liquid crystal phase formation increases¹⁶. In fact, when size of graphene oxide decreases to nano-meter range, usually referred as graphene quantum dots, no liquid crystal phase formation has been reported. Besides, graphene quantum dots also showed higher charge density and stability in water with high salt concentration, compared with the large size GO¹⁵. Thus, a drastic change of the arrangement behavior of graphene quantum dots in aqueous solution would also be expected.

Herein, we successfully employed graphene quantum dots as the soft template, reporting a one-step, bottom up method for sulfur@graphene core-shell composite fabrication with various shapes (Spherical, nanosheet, nano-wires), by utilizing the

unique amphiphilicity of graphene quantum dots. We found, for the first time, the graphene quantum dots undergo micelle formation in aqueous solution. The size and shape of the graphene micelle can be easily adjusted by changing the solution condition (ionic strength, dielectric constant) and it determine the size and shape of the resulted sulfur@graphene core-shell composite material. Our sulfur source, H_2S , a major air pollutant, was directly converted as the sulfur cathode, which opens up a potential route toward effective pollution control.

3.2 results and discussion

3.2.1 Micelle formation of graphene quantum dots in aqueous solution and its multiple roles in sulfur generation with core-shell structure via one step reaction.

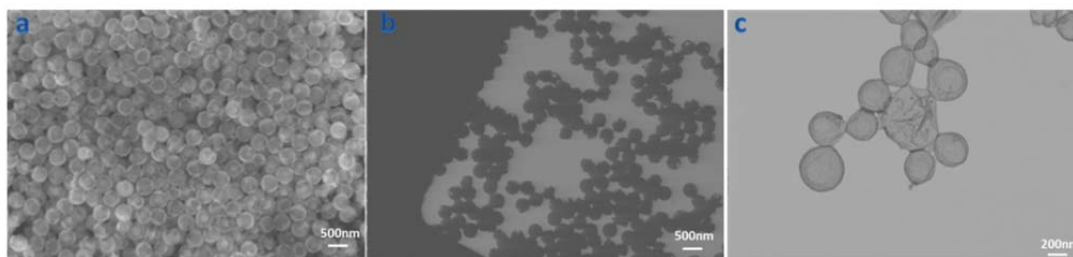


Fig. 3.2.1.1 SEM (a) STEM(b) image of as prepared sulfur particles from H_2S H_2O_2 reaction in the existence of NQD; STEM (c) image of empty shell after sulfur removal via heat treatment.

The sulfur products from H_2S H_2O_2 reaction in pure water are large aggregates of particles with various shapes. Spherical shape of sulfur@graphene core-shell composite was obtained when graphene quantum dots were present. Mono-dispersive S nanospheres with average diameter of 400nm were obtained when H_2S was bubbled into graphene quantum dots water solution (containing 0.5% H_2O_2 as the oxidant) at the flow rate of 75 sccm for one min, as demonstrated by SEM and STEM observation in Fig.3.2.1.1 a and

(b), respectively. More interestingly, the removal of element sulfur by heat treatment result in transparent shell leftovers (Fig.3.2.1.1 c). Thus, core shell sulfur@graphene composite material was directly obtained by a one-step reaction. The size and shape of the final sulfur@graphene composite material was a replication of the size and shape of the pre-formed graphene quantum dots micelle in the solution. In water, the electrostatic repulsion force of the ionizable edge group tends to push all the individual sheets apart. However, if they are pushed too far apart, all of their hydrophobic domain will be accessible by water. The free energy will be increased due to the hydrophobic effect. Thus the hydrophobic effect will tend to keep the graphene quantum dots closely packed while the repulsive (electrostatic) forces tend to push them apart. The balance between these opposing forces will lead to an optimum sheets spacing and orientation. For graphene quantum dots, the repulsion force is adjustable up on changing the solution condition. The characteristic thickness of the electric double layer is the Debye length κ can be predicted by the following equation (1)

$$\kappa^{-1} = \sqrt{\frac{\epsilon_r \epsilon_0 k_B T}{2 N_A e^2 I}}$$

equation3.2.1.1

I is the ionic strength of the electrolyte, ϵ_0 is the permittivity of free space, ϵ_r is the dielectric constant, k_B is the Boltzmann constant, T is the absolute temperature in kelvins, N_A is the Avogadro number. e is the elementary charge. The above equation revealed that the repulsion force between the individual graphene quantum dots will become smaller with the addition of salt (increase of ionic strength) or with the introduction with solvent with relatively low dielectric constant. As a result, aggregation number will be increased since more graphene can be incorporated into micelle formation due to the decrease of

repulsion forces, a change of either the size or shape of the graphene quantum dots micelle can be expected. To prove this concept, we introduced certain level of ionic strength and ethanol for the sulfur generation in the present of graphene quantum dots, respectively.

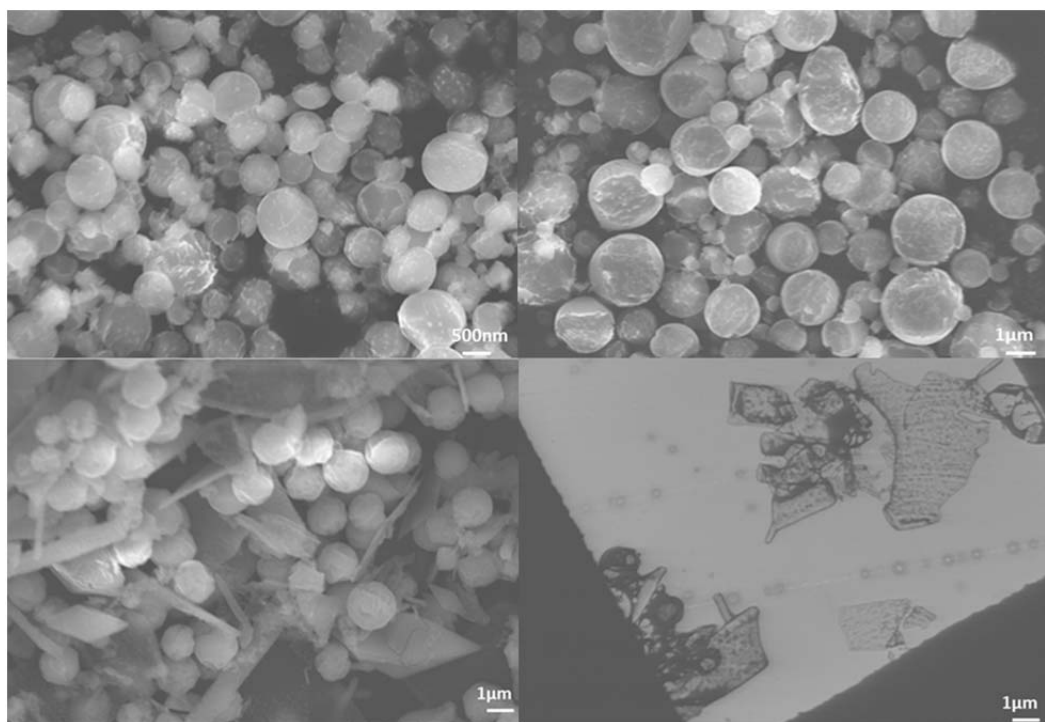


Fig. 3.2.1.2 SEM of sulfur@graphene composite material from H_2S H_2O_2 reaction in the present of graphene quantum dots (a) with the addition of 0.5M Na_3PO_4 , (b) with the addition of 1M Na_3PO_4 , (c) H_2O :Ethanol (1:1) mixed solvent system; STEM (d) image of empty shell after sulfur removal via heat treatment from (c).

With the same graphene quantum dots concentration ($75\mu\text{g/ml}$), the addition of salt leads to dramatic change of the size and uniformity of sulfur product. The obtained sulfur@graphene composites are still spherical in shape. However, the average size of the spheres increase dramatically, 500nm to $1\mu\text{m}$ (Fig.3.2.1.2 a) in the present of 0.5M Na_3PO_4 and $1\mu\text{m}$ to $1.5\mu\text{m}$ (Fig.3.2.1.2 b) in the present of 1M Na_3PO_4 , respectively. In the case of adding ethanol, the dielectric constant of the mixed solvent system decreases

and so does the repulsion force between the individual graphene quantum dots. Very interestingly, sulfur@graphene core-shell composite generated in this solvent media (H_2O_2 : EtOH=1:1) was a mixture of spherical, planner (nano sheet) and cylindrical (nano-wire) shape (Fig.3.2.1.2. c). The graphene shell was again captured by the STEM observation after sulfur removal by heat treatment for the composite material with different geometry (Fig.3.2.1.2 d). The above observations strongly support our assumption that the size and shape of the final sulfur@graphene composite material was a replication of the size and shape of the pre-formed graphene quantum dots micelle in the solution. In fact, traditional polymer micelles were actively employed for the growth of inorganic particles with controlled size and shape. For example, poly-vinylpyrrolidone (PVP) micelle was successfully used as the soft template to grow gold, Si and element sulfur nanoparticles with controlled size and shape^{6,17}.

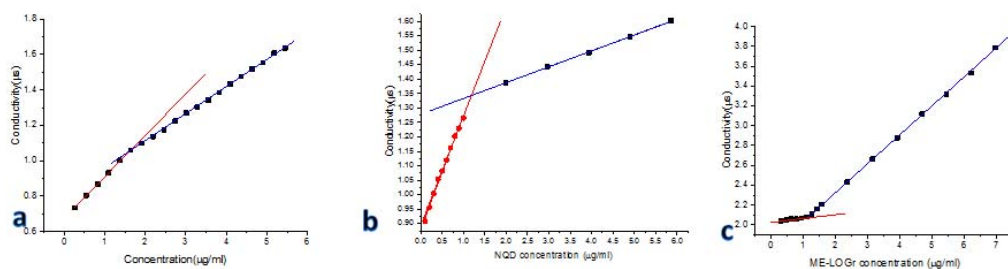


Fig. 3.2.1.3 Critical micelle concentration determined by conductivity measurement: (a) Regular graphene quantum dots; (b) Nitrogen doped graphene quantum dots; (c) Microwave-enabled low oxygen nano graphene.

In colloidal and surface chemistry, the critical micelle concentration (CMC) is defined as the concentration of surfactants above which micelles form and all additional surfactants added to the system go to micelles formation. We used conductivity measurement to determine the CMC of our nano-carbon materials in the aqueous solution. The electrical conductivity of a solution is measured by determining the resistance of the solution between two cylindrical electrodes separated by a fixed distance. An alternating voltage is used in order to avoid electrolysis¹⁸. Below the CMC, the addition of graphene quantum dots to an aqueous solution causes an increase in the number of charge carriers and consequently, an increase in the conductivity. Above the CMC, further addition of graphene quantum dots increases the micelle concentration while the number of separated individual graphene sheet remains approximately constant (at the CMC level). Since a micelle is much different in size and charge density compare with individual sheet, their efficiency of functioning as the charge carrier will also be different. Even though an increase of conductivity will still be observed, the plot of conductivity against graphene quantum dots concentration is, thus expected to show a break at the CMC. Three types of graphene quantum dots were studied for their aggregation behavior in the solution. Nano size graphene oxide, which was referred as regular graphene quantum dots (RQD), was prepared by the top down method from graphite powder via mixed acid and KMnO₄ treatment¹⁹. Nitrogen doped graphene quantum dots (NQD) was obtained from bottom up reaction of citric acid and urea under microwave irradiation. Microwave-enabled low oxygen nano graphene (ME-LOGr) with π -conjugated aromatic structures and properties largely retained was prepared via a one-step reaction we reported previously²⁰. The CMC of RQD, NQD and ME-LOGr has been identified as 1.64 μ g/ml, 1.17 μ g/ml and

1.14 μ g/ml, respectively as shown in Fig. 3.2.1.3. The decrease of the slop for both RQD and NQD revealed that the large size micelle diffuse slower than the individual sheet in electric field, which is consistent with the observation of tradition ionic surfactant such as sodium dodecyl sulfate (SDS). On the contrary, a jump of slop was observed for ME-LOGr. This might due to the fact that the lacks of ionizable edge groups make it a less efficient charge carrier as individual sheet in water. However, since it's conductive by itself, with the increase of its concentration, when percolation threshold was reached where long term connectivity was realized, a drastic increase of conductivity was observed.

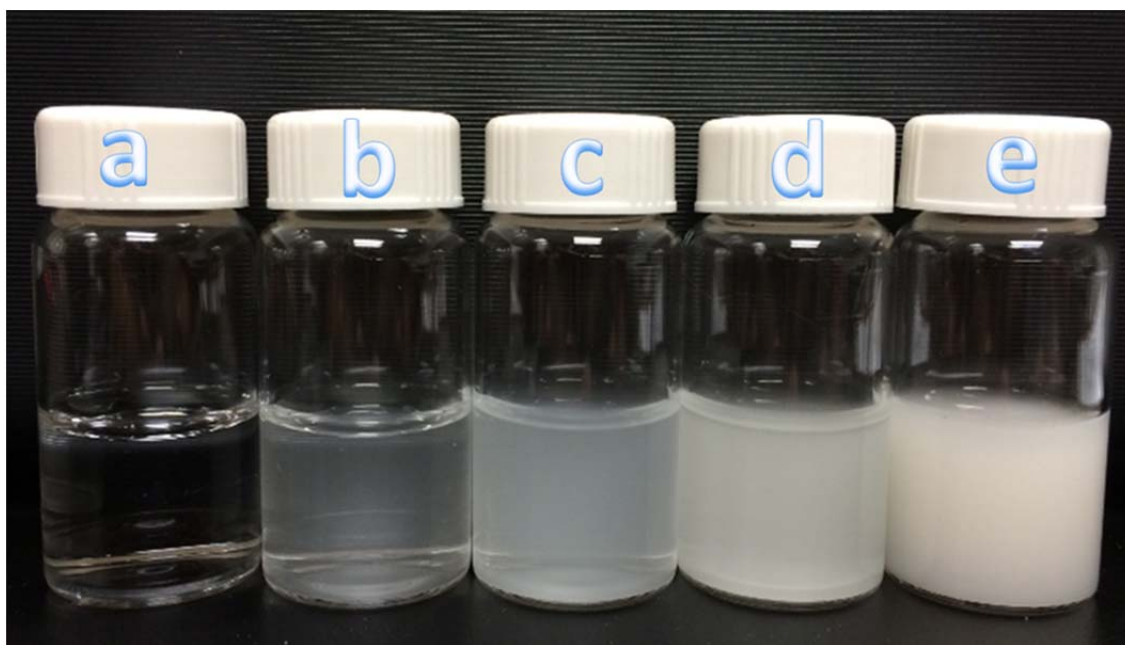


Fig. 3.2.1.4 Camera pictures of a)Pure water; b)no heterogeneous catalyst for H_2S H_2O_2 reaction ; c) Conductive nano graphene as the seeding template and catalyst; d) Regular graphene quantum dots as the seeding template and catalyst; e)Nitrogen doped graphene quantum dots as the seeding template and Catalyst

Apart from being as the soft template for sulfur growth, graphene quantum dots were also found to be able to function as the catalyst for H_2S oxidation reaction with H_2O_2 as an environmental benign oxidant. The catalytic activity of ME-LOGr, RQD, NQD toward this reaction was studied. As illustrated in Fig.3.2.1.4 b, Sulfur generation by bubbling H_2S directly into 0.5% H_2O_2 solution for 30 seconds at the flow rate of 75 sccm is observable compared with Fig. 3.2.1.4 a(pure water), but not efficient. By introducing the ME-LOGr prior for the H_2S bubbling, slightly increased sulfur particle generation is observed (Fig.3.2.1.4 c). With the introduction of RQD (Fig.3.2.1.4 d) or NQD (Fig.3.2.1.4 e), the yield of sulfur particles have been much improved. NQD shows the highest catalytic activity at the same reaction condition. The nature of catalytic activity of these carbon materials may originate from their catalytic ability toward H_2O_2 reduction. In order to verify this, UV/Vis spectroscopy was adopted to study the interaction between the NQD and H_2O_2 .

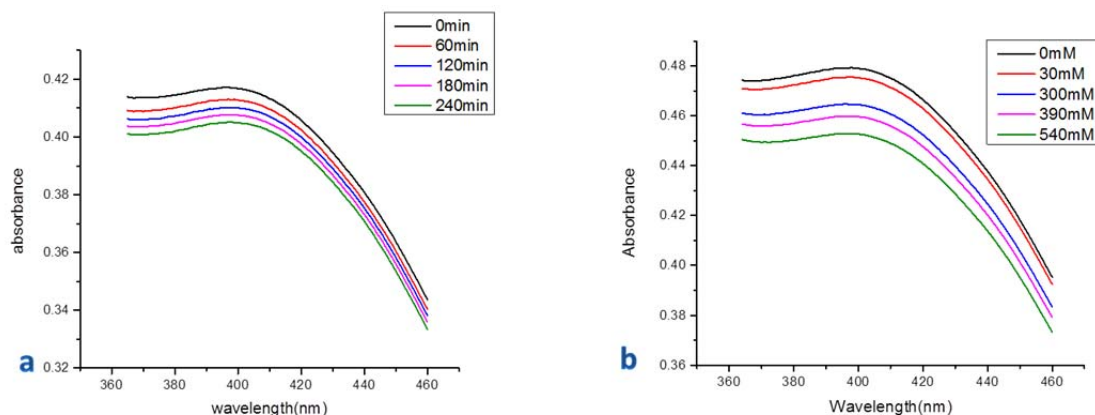


Fig.3.2.1.5 (a) UV/Vis absorption spectra of NQD in a pH 6.8 Phosphate buffer solution, change as a function of time after addition of 300 mM H₂O₂; (b) UV/Vis absorption spectra of NQD in a pH 6.8 phosphate buffer solution, change as a function of H₂O₂ concentration. The concentration of NQD is 27 µg/mL.

Fig. 3.2.1.5 shows a typical set of time dependent and H₂O₂ concentration dependent UV/Vis absorption spectra of NQD at pH=6.8 buffer. The absorption peak at 398nm is ascribed to electron transition of $n \rightarrow \pi^*$ for C=N of NQD²¹. It's found that the absorption intensity of the major peak at 398nm of NQD decreases with increase of both the addition time of H₂O₂ and H₂O₂ concentration, as depicted in Fig. 3.2.1.5 a and Fig. 3.2.1.5 b, respectively. It has been reported that electron transfer from graphene (or other nano carbon materials such as carbon nanotube) could diminish their absorption intensities²². We hypothesized the strong electronic interactions between the NQD and H₂O₂ might have changed the charge density of the NQD, which induced the absorption diminishing. This result indicated that NQDs plays catalytic role in activating the oxidant H₂O₂, which largely facilitates its oxidation H₂S to generate S particles²³.

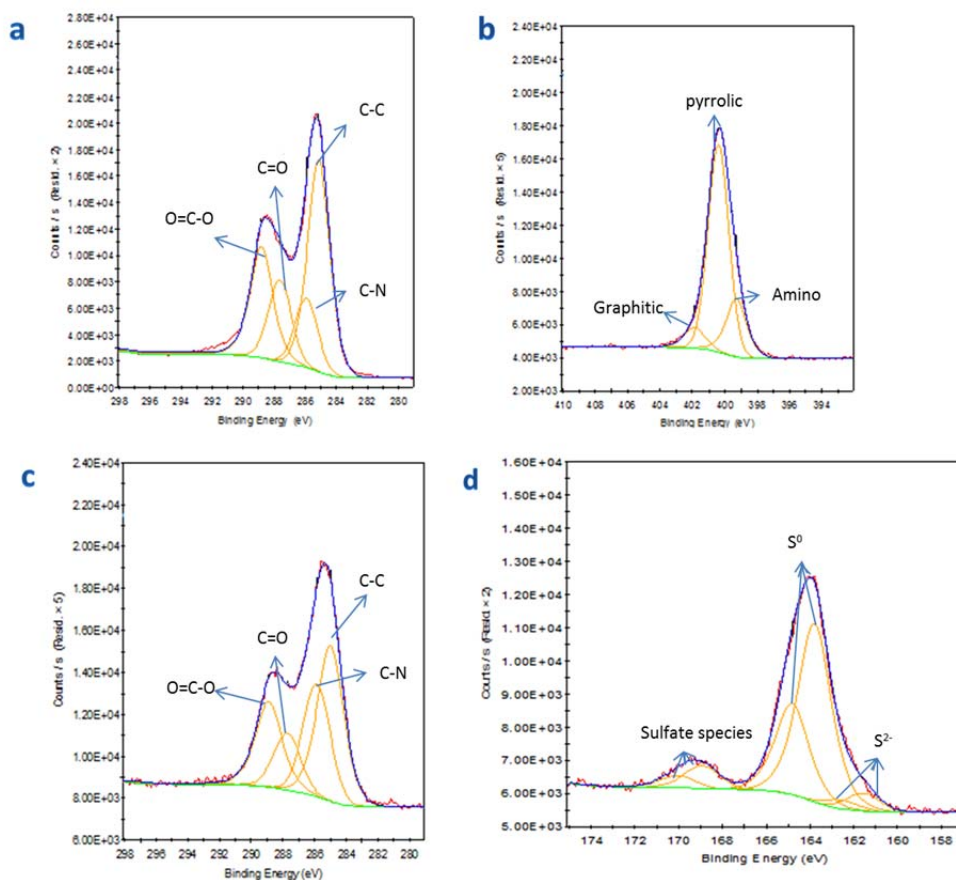


Fig.3.2.1.6 XPS characterization a) C 1s spectrum of nitrogen doped graphene quantum dots; b) N 1s spectrum of nitrogen doped graphene quantum dots; c) C 1s spectrum of sulfur@graphene composite; d) S 2p XPS spectrum and fitted curves for the sulfur@graphene composite.

X-ray photoelectron spectroscopy (XPS) is used to detect the elemental composition and functional groups of the nitrogen doped graphene quantum dots (NQD) and the composite material as shown in Fig.3.2.1.6. In the C 1s spectrum of NQD (Fig.3.2.1.6 a), four peaks at 288.88, 287.73, 285.88, and 285.00 eV, which are indexed to the O=C-O, C=O, C-N, and C-C groups, respectively²⁴. The nitrogen bonding configuration was also studied. In the N 1s spectrum of NQD in Fig.3.2.1.6 b, three main peaks at 401.86, 400.39 and 399.29 eV can be ascribed to graphitic N, pyrrolic N and pyridinic nitrogen in graphene structure, respectively^{25,26}. C 1s spectrum of the composite material revealed

the same carbon environment compared with the original NQD as shown in Fig.3.2.1.6 c. A slight decrease of the intensity of the C=O species might result from the mild reduction of the NQD by the H₂S. Fig. 3.2.1.6 d displays the S 2p XPS spectrum and fitted curves for the sulfur@graphene nanocomposite. This spectrum can be fitted by three components. Each component has a S 2p_{3/2} and 2p_{1/2} doublet with a fixed intensity ratio of 2:1 and an energy separation of 1.2 eV. The fitted S 2p_{3/2} components have binding energies of 161.59, 163.79 and 168.95 eV, which can be ascribed to S²⁻ element sulfur (S⁰) and sulfate species, respectively²⁷⁻²⁹. The weak S²⁻ component may be caused by the residual H₂S during the chemical synthesis process. While the small shoulder at 167.8 eV can be ascribed to the sulphate species formed by oxidation of sulfur in air. Therefore, sulfur@graphene core-shell composite was indeed obtained.

3.2.2 Electrochemical evaluation of as prepared sulfur@graphene composite and composite with additional polymer coating.

The core-shell sulfur@graphene composite materials fabricated here from graphene quantum dots micelle solution could be used to address some of the issues of Li-S battery. For example, the flexible graphene shell can function as a protection layer for accommodation the large volume change of element sulfur upon continuous charge/discharge. The continuous carbon sphere should also be able to serve as the reservoir to trap the soluble intermedia polysulfide species. Nitrogen doping, a strong interaction between the carbon material and polysulfide species was expected³⁰⁻³². Relatively high conductivity offered by the carbon material coating is beneficial to

improve the rate capability of Li-S battery. The as prepared sulfur@graphene composite material was directly used as the cathode material for Li-S battery.

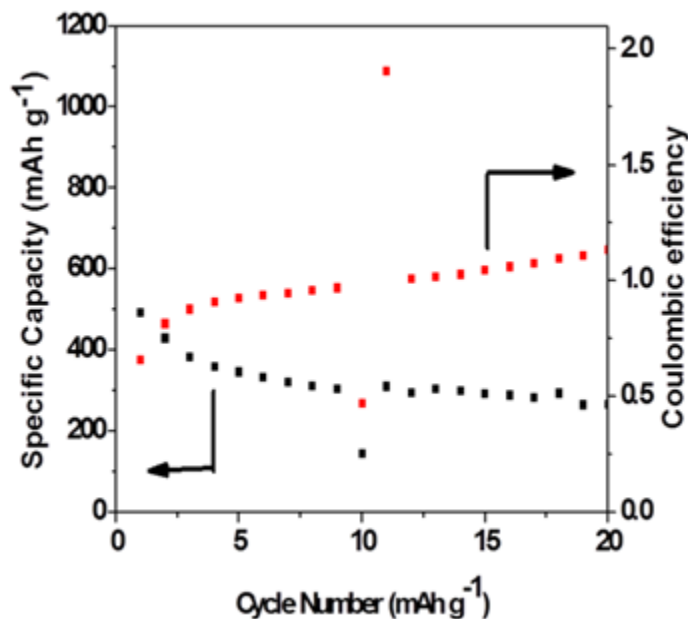


Fig.3.2.2.1 cycle stability of the as prepared sulfur@graphene composite cathode

As presented in Fig.3.2.2.1 very high initial discharge capacity of 500mAh/g (base on the total weight of the composite) was obtained due to the small uniform particles size. Unfortunately, a rapid capacity drop was observed for the following cycles. The rapid capacity fading indicates the loss of active material, element sulfur, is severe during the charge/discharge cycle.

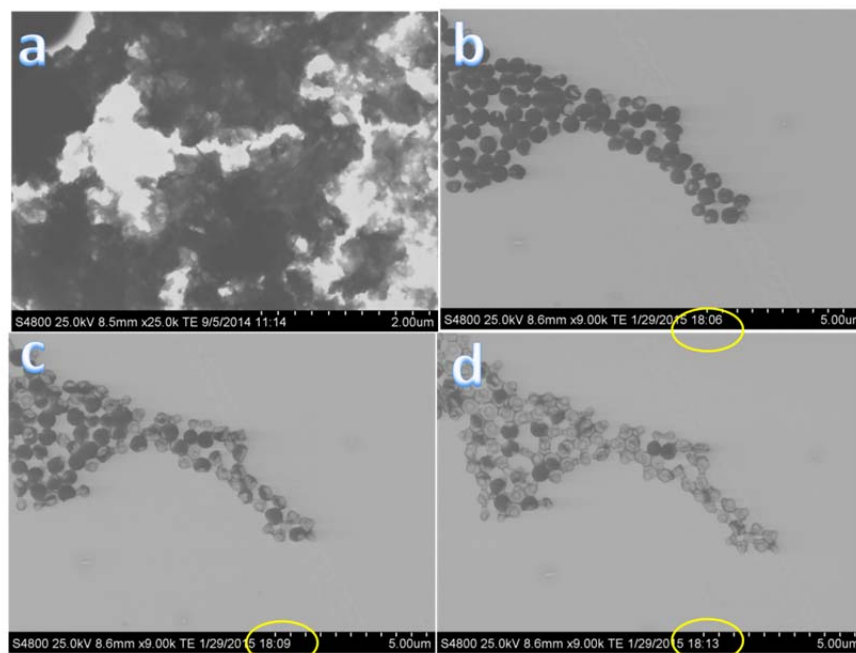


Fig.3.2.2.2 a) STEM image of “carbon shell” after sulfur removal by toluene test; Stability test of sulfur@graphene composite under high vacuum and electron beam irradiation as the function of time b) at 0 min; c) 3 min and d) 7 min

Then stability test of was carried out in toluene, which is a good solvent for the dissolution of element sulfur. As presented in Fig. 3.2.2.2 a, after the sulfur was fully removed, no free standing shell can be observed as we did from the heat treatment. Thus, the disassembly of the carbon sphere in the organic electrolyte might be accountable for the fast capacity fading since no more protection after the graphene shell disassembled. Besides, we found that in the STEM environment (with high vacuum level and electron beam irradiation), element sulfur in the sulfur@graphene sublime automatically after certain period of time (Fig.3.2.2.2 b-d). Therefore, porous structure must be existed in the graphene shell of the as prepared composite. Besides, it should be notice that the as-prepared core-shell composite is stable in aqueous solution since all electron microscopy characterization was carried out after the sample thoroughly clean by distilled water. Therefore, the organic electrolyte and harsh electrochemical testing conditions were

responsible for the disassembly of the graphene shell. In turns, the element sulfur will be fully exposed to the electrolyte once the shell was disassembled. Polysulfide was then can be dissolved into the electrolyte after it was formed during the discharge process. The loss of active material is accountable for the poor cycle stability.

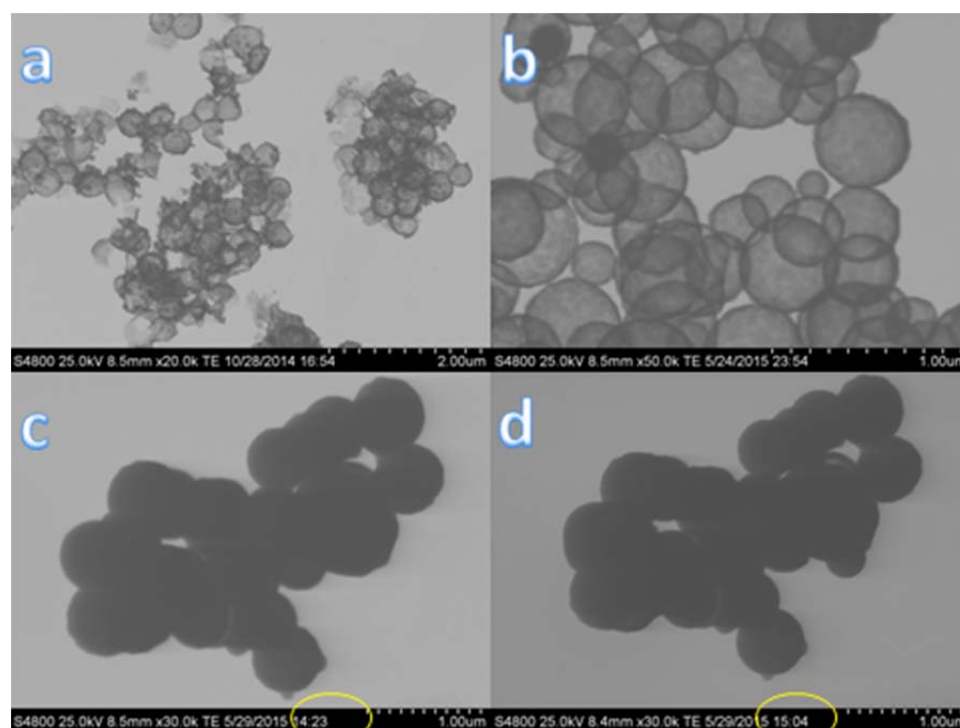


Fig. 3.2.2.3 STEM images of a) left over of Poly(3,4-ethylenedioxythiophene) coated sample after toluene test; b) left over of Poly-dopamine coated sample after toluene test; c) Poly-dopamine coating composite sample before toluene test at 0min; d) Poly-dopamine coating composite sample before toluene test at 40min.

Additional post coating, such as Poly(3,4-ethylenedioxythiophene) (PEDOT) and poly-dopamine, on the existing graphene shell were applied in order to improve the stability of the overall core-shell structure. As presented in Fig. 3.2.2.3 a, after toluene test, the leftover shell still exhibit spherical shape as the original composite particles. However, large amount of disassembled graphene sheet can still be directly observed. On the other hand, sample with additional poly-dompamine coating presents shell integrity

after toluene test as shown in Fig. 3.2.2.3 b. Furthermore, compared with original sulfur@graphene composite, the poly-dopamine coated sample shows much improved stability under high vacuum and electron beam irradiation. Fig. 3.2.2.3c and Fig. 3.2.2.3d present the STEM images of poly-dopamine coated sample at 0min and 41min, respectively after loading into the STEM sample chamber. Even though the STEM observation shows shell integrity, the fact the element sulfur can still be dissolved out of the shell by toluene, indicates that porous structure still existed on the shell. Therefore, upon exposing to solvent/electrolyte, the core materials can still be on direct contact due to the solvent/electrolyte penetration through the porous shell, which leads to dissolution of the core materials out of the shell. Hence, both PEDOT coated sample and poly-dopamine still displayed unsatisfactory cycle stability. Further improvement will be carried out in our group.

3.3 Conclusion

In conclusion, sulfur@graphene core-shell composite was fabricated through a novel one-step, bottom up assembly method. The unique amphiphilicity of graphene quantum dots was employed for the sulfur growth. For the first time, the graphene quantum dots were found to undergo micelle formation in aqueous solution. The size and shape of the graphene micelle can be easily adjusted by changing the solution condition (ionic strength, dielectric constant). When applying for sulfur growth, the size and shape of the graphene micelle determined the size and shape of the resulted sulfur@graphene core-shell composite material. Our sulfur source, H_2S , a major air pollutant, was directly converted as the core-shell composite, which opens up a potential route toward effective

pollution control. Further efforts on exploring this composite material for battery application are undergoing.

3.4 Materials and methods:

Synthesis of Nitrogen doped graphene quantum dots

0.21g Citric Acid (1.1mmols) + 0.18g Urea (3.5mmols) were dissolved in 1ml water. The solution then was dry in the vacuum oven at 800C for 2 hour to remove the majority of water. The mixture was then put into the microwave reaction chamber (CEM discover). Subsequently, the reaction mixture was subjected to microwave radiation (300W) for 40s. The orange brown powder obtained from the reaction was then dispersed in 25ml water via bath sonication. The quantum dots dispersion was then centrifuge at 8500 rpm for 15min and the supernatant was collected for dialysis.

Synthesis of regular graphene quantum dots

75ml concentrated sulfuric acid, 25ml concentrated nitric acid were mixed with 1g of graphite powders in a 250ml flask. The mixture was then stirred at 1000C for 24 hours. After neutralized with NaHCO_3 , the remaining mixture was subjected to filtration (0.02 μm , polycarbonate membrane) to remove the unreacted graphite powder. The filtrate was collected for dialysis.

Synthesis of Microwave-enabled low oxygen nano graphene (ME-LOGr)

0.2ml water and 20 mg of graphite are mixed with 7ml concentrated sulfuric acid and water in a round-bottom flask. The mixture is then swirled and cooled in an ice bath for

approximately 5 min. 2.8ml concentrated nitric acid is then added. The entire mixture is swirled and mixed for another 30 s and placed into a microwave reactor chamber. The reaction mixture is subject to microwave irradiation (300 W) for 30 s. Subsequently, the reaction is quenched with 200 mL of deionized water, filtered through an alumina anodic filter (0.02 μm pore size), and washed with 800 mL of deionized water. The cake on the membrane is then re-dispersed into water with 30 min of bath sonication. The dispersion obtained is then left undisturbed for five days to let the unexfoliated graphite particles precipitate out.

Preparation of sulfur@graphene core-shell nano-composite

9.5ml water, 0.25ml 35%wt hydrogen peroxide water solution was mixed with 0.25ml NQD solution (3mg/ml) in a 20ml glass vial. The mixture was then preheated in water bath at 400C for 2 min prior to the H_2S bubbling. The concentrated H_2S gas was then bubbled into the mixture solution at the flow rate of 75sccm for 60s. The glass vial was then capped after the 60s gas bubbling for 15min with continuous stirring. The resulted mixture was then subjected to repeated centrifugation and water washing to remove unreacted chemicals. The final product was collected by filtration with extensive washing with water.

PEDOT coating

50mg as prepared sulfur@graphene nano-composite particles were dispersed in 50ml of water, to which 55 μ l EDOT monomer, 500g of camphorsulfonic acid and 300mg of $(\text{NH}_4)_2\text{S}_2\text{O}_8$ oxidant was added. The polymerization was then carried out at room temperature for 24 hours. The resulted mixture was then subjected to repeated centrifugation and water washing to remove unreacted chemicals. The final product was collected by filtration with extensive washing with water.

Polydopamine coating:

50mg as prepared sulfur@graphene nano-composite particles were dispersed in 60ml of pH 8.5 Tris buffer, to which 120mg dopamine was added. The polymerization was then carried out at room temperature for 16 hours. The resulted mixture was then subjected to repeated centrifugation and water washing to remove unreacted chemicals. The final product was collected by filtration with extensive washing with water.

Characterization: Lateral dimension and thickness of the carbon materials were studied using a Nanoscope IIIa Multimode scanning probe microscope system (Digital Instruments, Bruker) with a J scanner operated in the “Tapping Mode”. Morphology and particle size of different samples were observed using a Hitachi S4800 field emission scanning electron microscopy (SEM, STEM).

3.5 References

- 1 Whittingham, M. S. Lithium batteries and cathode materials. *Chemical Reviews* **104**, 4271–4301 (2004).
- 2 Goodenough, J. B. & Kim, Y. Challenges for Rechargeable Li Batteries. *Chemistry of Materials* **22**, 587-603, doi:10.1021/cm901452z (2010).
- 3 Guo, Y.-G., Hu, J.-S. & Wan, L.-J. Nanostructured Materials for Electrochemical Energy Conversion and Storage Devices. *Advanced Materials* **20**, 2878-2887, doi:10.1002/adma.200800627 (2008).
- 4 ARUMUGAM MANTHIRAM, YONGZHU FU & SU, Y.-S. Challenges and Prospects of LithiumSulfur Batteries. *ACCOUNTS OF CHEMICAL RESEARCH* **46**, 1125-1134 (2013).
- 5 Sun, L. *et al.* Sulfur Nanocrystals Confined in Carbon Nanotube Network As a Binder-Free Electrode for High-Performance Lithium Sulfur Batteries. *Nano Letters* **14**, 4044-4049, doi:10.1021/nl501486n (2014).
- 6 Li, W. *et al.* High-performance hollow sulfur nanostructured battery cathode through a scalable, room temperature, one-step, bottom-up approach. *Proceedings of the National Academy of Sciences* **110**, 7148-7153, doi:10.1073/pnas.1220992110 (2013).
- 7 Guo, J., Xu, Y. & Wang, C. Sulfur-Impregnated Disordered Carbon Nanotubes Cathode for Lithium–Sulfur Batteries. *Nano Letters* **11**, 4288-4294, doi:10.1021/nl202297p (2011).
- 8 Zhang, W. *et al.* A Li⁺-conductive microporous carbon–sulfur composite for Li-S batteries. *Electrochimica Acta* **87**, 497-502, doi:10.1016/j.electacta.2012.09.086 (2013).
- 9 Liang, C., Dudney, N. J. & Howe, J. Y. Hierarchically Structured Sulfur/Carbon Nanocomposite Material for High-Energy Lithium Battery. *Chemistry of Materials* **21**, 4724-4730, doi:10.1021/cm902050j (2009).
- 10 Xiulei Ji, K. T. L. a. L. F. N. A highly ordered nanostructured carbon–sulphur cathode for lithium–sulphur batteries. *NATURE MATERIALS* **8**, 500-506, doi:10.1038/nmat246010.1038/NMAT2460 (2009).
- 11 Kim, J. *et al.* An Advanced Lithium-Sulfur Battery. *Advanced Functional Materials* **23**, 1076-1080, doi:10.1002/adfm.201200689 (2013).
- 12 Li, W. *et al.* Understanding the Role of Different Conductive Polymers in Improving the Nanostructured Sulfur Cathode Performance. *Nano Letters* **13**, 5534-5540, doi:10.1021/nl403130h (2013).
- 13 Wei Seh, Z. *et al.* Sulphur–TiO₂ yolk–shell nanoarchitecture with internal void space for long-cycle lithium–sulphur batteries. *Nature Communications* **4**, 1331, doi:10.1038/ncomms2327 (2013).
- 14 Erickson, K. *et al.* Determination of the Local Chemical Structure of Graphene Oxide and Reduced Graphene Oxide. *Advanced Materials* **22**, 4467-4472, doi:10.1002/adma.201000732 (2010).
- 15 Cote, L. J. *et al.* Graphene oxide as surfactant sheets. *Pure and Applied Chemistry* **83**, doi:10.1351/pac-con-10-10-25 (2010).
- 16 Kim, J. E. *et al.* Graphene Oxide Liquid Crystals. *Angewandte Chemie International Edition* **50**, 3043-3047, doi:10.1002/anie.201004692 (2011).

- 17 Mao, P. Q. a. C. Biomimetic Branched Hollow Fibers Templated by Self-Assembled Fibrous Polyvinylpyrrolidone Structures in Aqueous Solution. *ACS NANO* **4**, 1573-1579 (2010).
- 18 Inoue, T., Ebina, H., Dong, B. & Zheng, L. Electrical conductivity study on micelle formation of long-chain imidazolium ionic liquids in aqueous solution. *Journal of Colloid and Interface Science* **314**, 236-241, doi:10.1016/j.jcis.2007.05.052 (2007).
- 19 Minati, L., Torrenzo, S., Maniglio, D., Migliaresi, C. & Speranza, G. Luminescent graphene quantum dots from oxidized multi-walled carbon nanotubes. *Materials Chemistry and Physics* **137**, 12-16, doi:10.1016/j.matchemphys.2012.08.071 (2012).
- 20 Mehulkumar A. Patel, H. Y., Pui Lam Chiu, Daniel D. T. Mastrogiovanni, Carol R. Flach,, Keerthi Savaram, L. G., Ashley Hemnarine, Richard Mendelsohn, Eric Garfunkel, & Huabei Jiang, and Huixin He. Direct Production of Graphene Nanosheets for Near Infrared Photoacoustic Imaging. *ACS NANO* **7**, 8147-8157 (2010).
- 21 Nie, H. *et al.* Carbon dots with continuously tunable full-color emission and their application in ratiometric pH sensing. *Chemistry of Materials* **26**, 3104-3112 (2014).
- 22 Ma, Y. *et al.* The electronic role of DNA-functionalized carbon nanotubes: Efficacy for in situ polymerization of conducting polymer nanocomposites. *Journal of the American Chemical Society* **130**, 7921-7928 (2008).
- 23 Song, Y., Qu, K., Zhao, C., Ren, J. & Qu, X. Graphene oxide: intrinsic peroxidase catalytic activity and its application to glucose detection. *Advanced Materials* **22**, 2206-2210 (2010).
- 24 Liu, S. *et al.* Hydrothermal Treatment of Grass: A Low-Cost, Green Route to Nitrogen-Doped, Carbon-Rich, Photoluminescent Polymer Nanodots as an Effective Fluorescent Sensing Platform for Label-Free Detection of Cu (II) Ions. *Advanced Materials* **24**, 2037-2041 (2012).
- 25 Zhang, C., Hao, R., Liao, H. & Hou, Y. Synthesis of amino-functionalized graphene as metal-free catalyst and exploration of the roles of various nitrogen states in oxygen reduction reaction. *Nano Energy* **2**, 88-97 (2013).
- 26 Hu, T. *et al.* Rapid synthesis of nitrogen-doped graphene for a lithium ion battery anode with excellent rate performance and super-long cyclic stability. *Physical Chemistry Chemical Physics* **16**, 1060-1066 (2014).
- 27 Schaufuß, A. G. *et al.* Incipient oxidation of fractured pyrite surfaces in air. *Journal of Electron Spectroscopy and Related Phenomena* **96**, 69-82 (1998).
- 28 Liang, X. *et al.* A highly efficient polysulfide mediator for lithium–sulfur batteries. *Nature communications* **6** (2015).
- 29 Zhang, L. *et al.* Electronic structure and chemical bonding of a graphene oxide–sulfur nanocomposite for use in superior performance lithium–sulfur cells. *Physical Chemistry Chemical Physics* **14**, 13670-13675 (2012).
- 30 Sun, X.-G., Wang, X., Mayes, R. T. & Dai, S. Lithium-Sulfur Batteries Based on Nitrogen-Doped Carbon and an Ionic-Liquid Electrolyte. *ChemSusChem* **5**, 2079-2085, doi:10.1002/cssc.201200101 (2012).

- 31 Wang, X., Zhang, Z., Qu, Y., Lai, Y. & Li, J. Nitrogen-doped graphene/sulfur composite as cathode material for high capacity lithium–sulfur batteries. *Journal of Power Sources* **256**, 361-368, doi:10.1016/j.jpowsour.2014.01.093 (2014).
- 32 Song, J. *et al.* Nitrogen-Doped Mesoporous Carbon Promoted Chemical Adsorption of Sulfur and Fabrication of High-Areal-Capacity Sulfur Cathode with Exceptional Cycling Stability for Lithium-Sulfur Batteries. *Advanced Functional Materials* **24**, 1243-1250, doi:10.1002/adfm.201302631 (2014).

Chapter 4. Anti-solvent assisted graphene oxide coating on various electrochemical active materials and its application toward flexible electrode fabrication

4.1 Introduction

Current commercial graphite anode has already reached its theoretical limit (372mAh g^{-1}). The exploration of alternative anode materials with high charge/discharge rates, reversible capacity, long cycle life and low cost has become an urgent task in order to meet the increasing demands of consumer electronics, electric vehicles and energy storage stations. SnO_2 has been reported as a promising candidate due to its high theoretical capacity (782mAh g^{-1}), nontoxicity and natural abundance^{1,2}. Its capacity for Lithium storage contributed to the reversible conversion reaction mostly from reversible alloying/ de-alloying processes of Sn with $\text{Li}^{3,4}$. Recently, SnO_2 anodes with specific capacity higher than its theoretical capacity have been reported, mainly due to the partial reversible conversion of Sn to SnO_2 coupled with a synergistic effect with carbonaceous materials or other nanomaterials⁵⁻⁸. That is, the theoretical specific capacity of SnO_2 can be increased from 782 to 1493mAh g^{-1} if the reaction is fully reversible (based on 8.4 Li ions). However, its practical application is limited by the severe volume change (up to 259%^{9,10}) during charge/discharge cycles, poor electronic conductivity and the aggregation of Sn clusters during cycling, which lead to poor cycle stability^{1-4,9-11}.

Compared with general strategies such as reducing particles size¹²⁻¹⁴ or dispersing active material into the solid matrix¹⁵⁻¹⁷, little attention has been devoted to binders. Traditional binders are insulating and electrochemically inactive, such as PVDF. They

were used to provide mechanical connections between active materials, conductive additives, and the current collector. However, the presence of the binder decreases the overall electrical conductivity and increases the polarization of the electrode. Recent works have demonstrated that polymeric conductive binders with strong mechanical binding force with the active material even with self-healing capability can be employed to address the large volume effect of anode materials. They also eliminated the need for the addition of conductive carbon¹⁸⁻²⁰. However, the synthesis of those conductive polymer binders usually necessitates complex coupling reactions requiring noble metal catalysts and stringent reaction conditions, which were not cost effective. Moreover, metallic current collectors (copper foil with mass density of 8.96g/cm³) were still needed for electrode fabrication. Therefore, 50% or more of the mass of these anodes can be considered as inactive components. Meanwhile, the relative low mass loading also results in limited area specific capacity.

Graphene has been extensively studied in the area of energy storage, especially in LIBs, due to its unique 2D structure, flexibility, and excellent mechanical strength, chemical stability, along with its thermal and electrical conductivity. Further, the capability of largescale production with various methods at low cost, makes graphene and its hybrids available as high performance electrode materials in energy storage^{2,21-27}. Graphene was also believed to be the perfect coating agent for high capacity anode material, such as SnO₂ and Si, offers fast transport channel of both lithium ions and electrons and elastic buffer space to accommodate the volume change upon cycling^{24,28-30}. Free standing, additive free graphene/active material sandwich paper can be fabricated simply via filtration. However, no wrinkled structure can be introduced to graphene in

this process. Therefore, the “buffering” capability of graphene is limited. Additionally, due to the different stability of the suspension and diffusion rate of different particles and graphene/graphene oxide during the filtration process, the distribution of particles in the graphene matrix was not uniform, which also leads to limited specific capacity and cycle stability^{2,31,32}. Recently, aerosol spray drying process³³ and solution ionic strength engineering³⁴ have been demonstrated as the general route for achieving graphene base core-shell composite. However, the products from both methods are generally isolated “particles”. Besides, the conductivity of graphene was not nicely recovered. Therefore, the fabrication of electrodes still needs the addition of conductive carbon and polymer binders. It would be interesting to explore assembly methods to produce graphene based composite anodes (e.g. SnO₂), for which a certain level of wrinkle structure was introduced to the graphene coating to maximize its “buffering” capability. In the meantime all graphene can still be interconnected in a way that no other component is needed, functioning as conductive binder. Graphene is also electrochemically active at low voltage window vs Li. Therefore, all components will contribute to the total capacity.

In this work, we developed a novel approach to rapidly and efficiently fabricate graphene based free standing, flexible and additive free electrode materials. This assembly approach is inspired by a frequently used method to purify and/or concentrate RNA, DNA in biochemistry. The synergy of ionic strength and dielectric constant change induced by a salt of low concentrations and ethanol/acetone allows for controllably engineering the assembled structures of graphene oxide and active materials. A free-standing, flexible SnO₂@Graphene composite anode was fabricated and used as an example for high energy lithium ion battery. In this composite anode material, the

graphene matrix not only functions as conductive binder and current collector, but also contributes to the total capacity. Additionally, the unique assembly approach generates a large amount of wrinkles and voids, which are beneficial for the accommodation of the large volume expansion of SnO₂ during the repeated charge/discharge cycles, which developed during this assembly process. A high specific capacity of 726 mAh g⁻¹ (calculated by the total mass) or area specific capacity of 2.2mAh cm⁻² was retained after 50 cycles for SnO₂@Graphene composite anode at the current density of 500mA/g. The assembly method developed in this study is general, robust and easy to apply to other functional materials rather than battery material, which opens up an easy path to fabricate flexible devices.

4.2: Result and discussion

4.2.1: Anti-solvent precipitation method as a general route to induce graphene coating on various particles with different size and shape

An anti-solvent precipitation method, especially ethanol precipitation, has been widely used to purify and/or concentrate RNA, DNA in biochemistry. This is accomplished by adding salt and ethanol to a solution containing DNA or RNA. RNA and DNA are water soluble due to their highly charged hydrophilic phosphate backbone. For water, with a high dielectric constant of 80.1 (at 20 °C), electrostatic forces between charged particles are considerably lower in aqueous solution than they are in vacuum or in air due to the following equation:

$$F = \frac{1}{4\pi\epsilon_r\epsilon_0} \frac{q_1q_2}{r^2} \quad 4.2.1.1$$

For which, ϵ_0 is the permittivity of free space, ϵ_r is the dielectric constant of the solvent. With the presence of small amount of cations, the relatively weak net electrostatic force prevents them from forming stable ionic bonds with phosphate groups and precipitating out of solution. The introduction of ethanol, with a dielectric constant of only 4.3 (at 25 °C), will largely disrupt the screening of charges by water, therefore the columbic force of attraction increases between the cations and the negatively charged nucleic acid backbone. If enough ethanol is added, the electrical attraction between phosphate groups and any positive ions present in solution becomes strong enough to form stable ionic bonds and then RNA/DNA will be precipitated^{35,36}. Previous study has demonstrated by Zeta potential measurement that GO is highly negatively charged when dispersed in water as a result of the ionization of $-\text{COOH}$ and $-\text{OH}$ edge functional group³⁷⁻⁴⁰. Therefore, we believed similar rules would apply for GO dispersion.

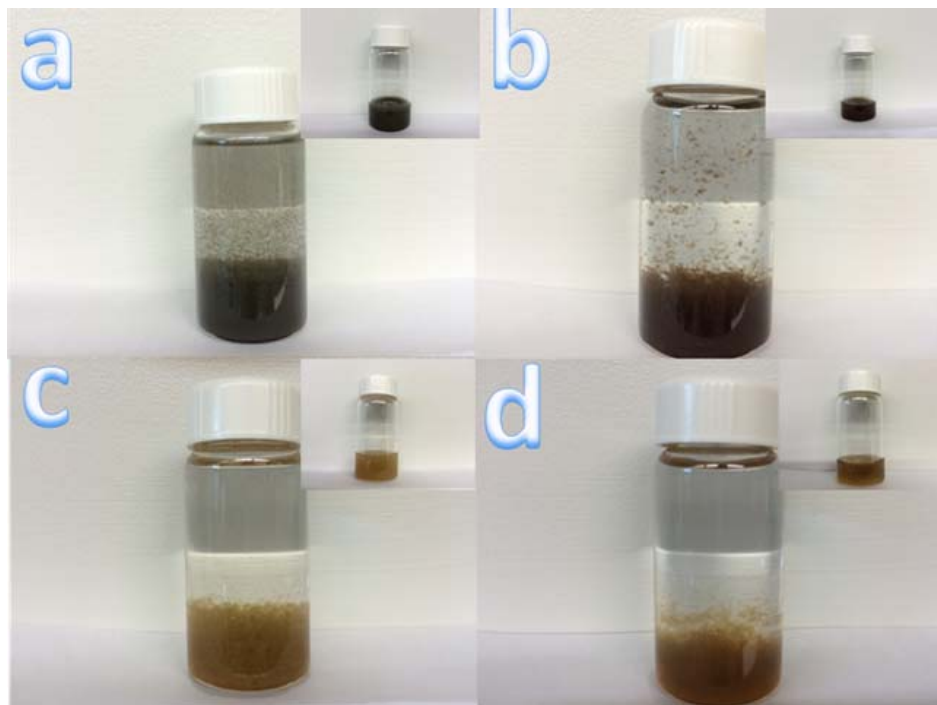


Fig. 4.2.1.1 camera picture of anti-solvent precipitation induced GO coating on a) metallic Sn; b) Lithium excess oxide ($\text{Li}_{1.2}\text{Mn}_{0.5}\text{Ni}_{0.3}\text{Co}_{0.3}\text{O}_2$); c) Element Si; d) SnO_2 , before (small picture) and after (large picture) addition of anti-solvent.

In our method, particles of different types, sizes and shapes were first dispersed with GO via ultra-sonication. Due to the amphiphilicity of GO, the resulting suspension were more stable than the suspension without the existence of GO. GO crumbling and coating on to dispersed particles was realized by the addition of a small amount of salt followed by the introduction of anti-solvent (ethanol, acetone) as shown in the Fig. 4.2.1.1. Without the addition of salt, the introduction of anti-solvent only results in uniform suspension in a larger volume in the mixed solvent system. When 10mM LiCl was added to the GO/particles suspension, part of the large particles precipitate at the bottom within two days, while GO stayed as uniformly dispersion in the solution over weeks due to the limited screening effect of low salt concentration. On the other hand, with addition of

10mM LiCl, instant GO precipitation together with the existing particles was observed within 5 seconds after anti-solvent (ethanol, acetone) addition, leaving the top solution to be transparent. With the introduction of anti-solvent, the dielectric constant of the mixed solvent was drastically decreased. In turn, the columbic attraction force increased between the cations and the negatively charged GO. The electronic repulsion among GO was screened when more cations were absorbed on the GO surface. Thus, the stable GO dispersion was disturbed. In this situation, with the existence of nanoparticles, GO tends to become crumpled, folded or directly coated onto the nanoparticles' to minimize its surface energy. As a result, the GO shrinking and wrapping can be realized within 5 seconds when anti-solvent was introduced, which is efficient for sample preparation.

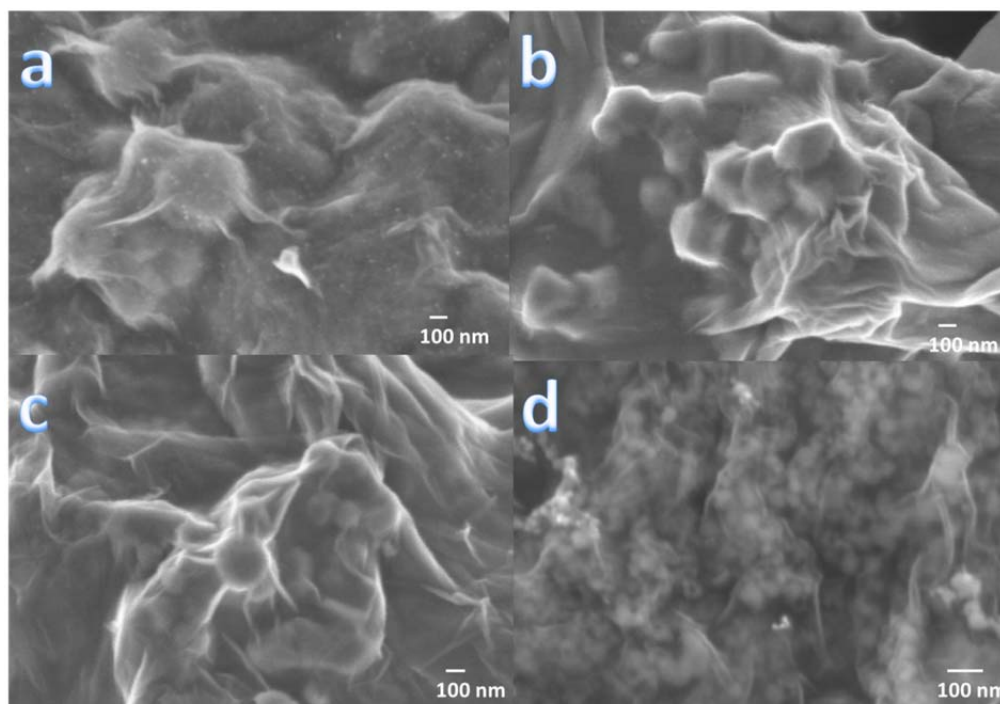
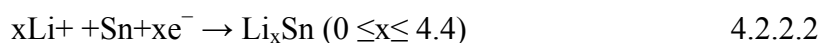


Fig. 4.2.1.2 SEM of anti-solvent precipitation induce GO coating on a) metallic Sn; b) Lithium excess oxide ($\text{Li}_{1.2}\text{Mn}_{0.5}\text{Ni}_{0.3}\text{Co}_{0.3}\text{O}_2$); c) Element Si; d) SnO_2

Although the amount of salt added is small, certain level of solubility of the chosen salt in the anti-solvent is still required to prevent co-precipitation of salt with GO and dispersed particles. The morphology of the GO coated particles via anti-solvent precipitation was examined by scanning electron microscope as shown in Fig. 4.2.1.2, when LiCl (10mM) was chosen as the added salt and acetone was employed as the anti-solvent. Metallic Sn, Lithium excess oxide ($\text{Li}_{1.2}\text{Mn}_{0.5}\text{Ni}_{0.3}\text{Co}_{0.3}\text{O}_2$), element Si and SnO_2 were all completely and tightly coated by graphene oxide sheets as shown in Fig. 4.2.1.2. Wrinkled structures of GO were observed at the void space in all cases. Our method reported here is not limited to ionic solute; molecule solute such as $\text{NH}_3\cdot\text{H}_2\text{O}$ and acetic acid (1M) can also be employed as the inducer for the anti-solvent precipitation of GO/particle suspension.

4.2.2: Electrochemical evaluation of free standing, additive free SnO_2 @Graphene composite anode for Lithium ion battery

SnO_2 has been reported as promising candidate as anode material due to its high theoretical capacity, nontoxicity and natural abundance^{1,2}. Its capacity for Lithium storage contributed to the reversible conversion reaction mostly resulting from reversible alloying/ de-alloying processes of Sn with Li ^{3,4}.



During the first Lithiation process, 1 mole of SnO_2 will react with 4 mols of Lithium ions and being converted to metallic Sn (reaction 4.2.2.1) followed by the subsequent alloying reaction with additional 4.4 mols of Lithium ions (reaction 4.2.2.2). However, the irreversibility of the reaction 4.2.2.1 leads to a specific capacity of only 782mAh/g for

SnO₂. Recently, SnO₂ anode with specific capacity higher than its theoretical capacity has been reported mainly due to the partial reversible conversion of Sn to SnO₂ coupled with a synergistic effect with carbonaceous material or other nanomaterials⁵⁻⁸. That is, the theoretical specific capacity of SnO₂ can be increased from 782 to 1493mAh/g if the reaction is fully reversible (based on 8.4 Li ions). Graphene based core-shell structure fabrication has been demonstrated as an effective strategy to obtain improved electrode performance, in terms of cycle stability and rate performance, for which graphene sheets can serve as structural cushion layer to accommodate the huge mechanical stress induced during cycling and to prevent the aggregation of SnO₂ nanoparticles^{2,8,27,41}. As we demonstrated earlier, the time needed for the graphene based core-shell structure fabrication method reported here is as short as 16min (15min for particles and GO dispersion via ultra-sonication and one min for salt and anti-solvent addition). In fact, sample collection via filtration is also efficient for this reported fabrication route due to the depletion of hydration layer of GO by anti-solvent addition. The obtained product can be easily peeled off from the filter paper as an integrated piece.

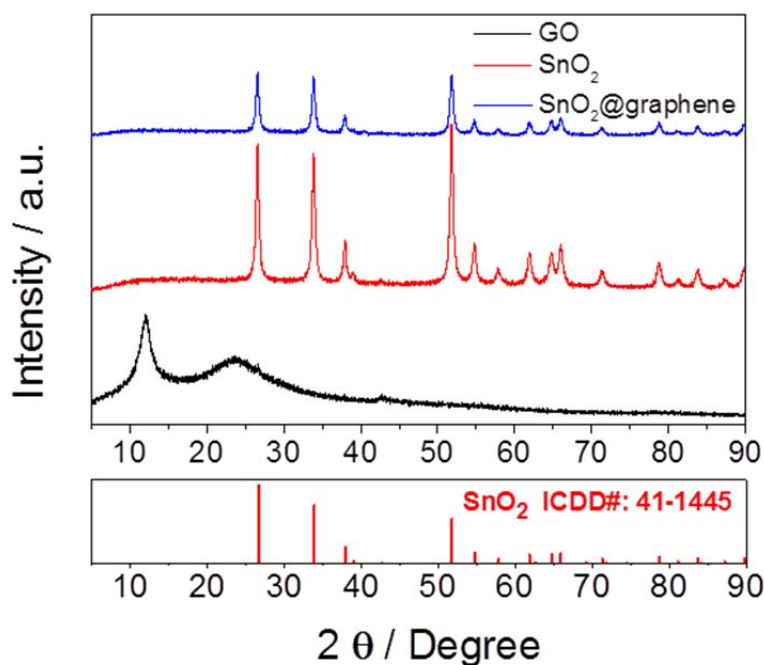


Fig. 4.2.2.1 XRD pattern of GO(black),bare SnO₂(red) and SnO₂@Graphene composite(blue)

To identify the crystalline structure, the XRD pattern of the GO powder, SnO₂ powder and SnO₂@Graphene nano-composite were investigated (Fig. 4.2.2.1). The recorded XRD pattern of SnO₂ powder can be well indexed to the tetragonal rutile structure of SnO₂ particles (JCPDS 41-1445). For the GO powder, the sharp peak at 12° (002) is a typical peak of GO, indicating an increase in interlayer spacing due to the oxidation and water intercalation in-between graphene layers. A broad peak at 23°, which is more common for reduced GO, was also observed in the GO powder. The observation of this broad peak might result from the drying process, which partially removed the intercalated water molecule, when heated in the oven at 70 degree. As for the SnO₂@Graphene nano-composite, all diffraction peaks can also be well indexed to the tetragonal rutile structure of SnO₂ particles. There are no obvious diffraction peaks of

graphene/graphene oxide observed in the pattern of $\text{SnO}_2@\text{RGO}$ nanocomposite paper, implying that the SnO_2 are homogeneously dispersed on graphene sheet and in between each graphene layer.

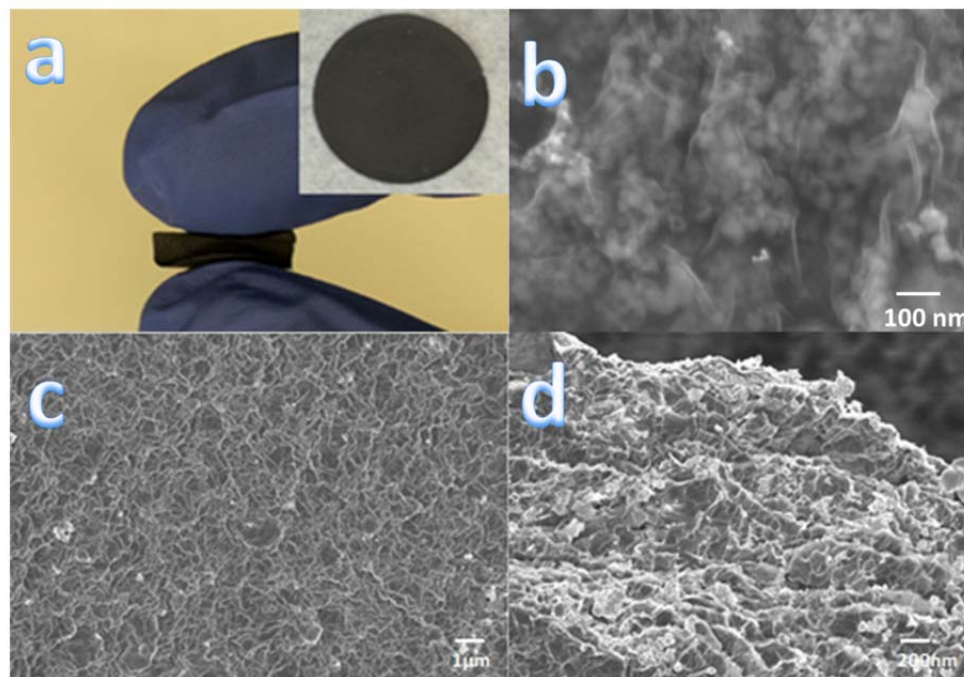


Fig. 4.2.2.2 a) Camera pictures of Free standing $\text{SnO}_2@\text{Graphene}$ composite anode after thermal annealing at 2000°C ; b) SEM(zoom in) of free standing $\text{SnO}_2@\text{Graphene}$ composite anode ; c) SEM picture(zoom out) of free standing $\text{SnO}_2@\text{Graphene}$ composite anode, top view; d) SEM pictures of free standing $\text{SnO}_2@\text{Graphene}$ composite anode, side view(intersection)

After thermal annealing (500°C for three hours), a free standing $\text{SnO}_2@\text{Graphene}$ composite electrode was obtained. The as-prepared composite is also flexible as presented in Fig. 4.2.2.2 a. The zoomed in SEM picture of composite film was shown in Fig. 4.2.2.2 b. The corresponding zoomed out SEM picture of its top view (Fig. 4.2.2.2 c) and side view (Fig. 4.2.2.2 d) revealed that less than 5% of SnO_2 were exposed outside the graphene matrix. Then, the as-prepared $\text{SnO}_2@\text{Graphene}$ composite was directly used as free standing, carbon black, binder and current collector free flexible anode for

Lithium ion battery. If all the graphene sheets are strictly monolayer, LiC_3 structures can be formed in which lithium is stored on both sides of the graphene sheet, delivered the theoretical capacity of 744mAh/g ⁴¹. Thermal analysis(Fig. 4.2.2.3) shows that the weight percentage of SnO_2 in the composite material is 67%. Therefore, the theoretical capacity of $\text{SnO}_2@\text{graphene}$ composite electrode can be calculated as:

$$\text{Total capacity} = C_{\text{SnO}_2} * 67\% + C_{\text{graphene}} * 33\% = 1493 * 67\% + 744 * 33\% = 1245\text{mAh/g}$$

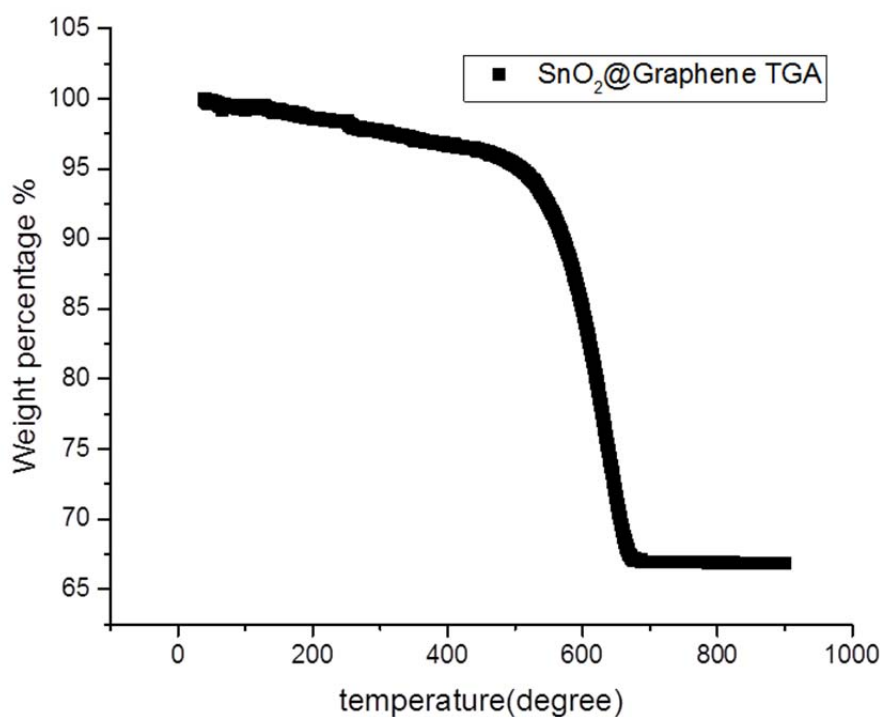


Fig. 4.2.2.3 Thermal gravimetric analysis (TGA) of $\text{SnO}_2@\text{Graphene}$ composite anode

It is notable that free-standing $\text{SnO}_2@\text{Graphene}$ composite film can be directly used as the anode for lithium ion batteries, in which there is no conductive carbon, polymer binder and even the copper current collector. Such configuration of the anode offers a promising application of lithium ion batteries for micro-structured and flexible devices.

The electrochemical properties and performances of SnO₂@Graphene composite anode are evaluated in the CR2025-type coin cell with the metallic lithium foil as the counter and reference electrode. For the comparative propose, the bare RGO film is also fabricated by using the same synthetic process for SnO₂@Graphene composite film, and the bare SnO₂-based anode is composed of 70 wt.% SnO₂ nanoparticles as the active material, 20 wt.% acetylene black as the conductive carbon and 10 wt.% polyvinylidene fluoride (PVDF) as the binder. Fig. 4.2.2.4a shows the cyclic voltammetric (CV) curves of SnO₂@Graphene composite anode in the first five cycles at a scan rate of 0.1 mV/s in a voltage range of 0.01-3.0 V vs. Li/Li⁺. The initial cathodic peak of SnO₂@Graphene anode at 0.74 V in high intensity in the first CV discharge is mostly attributed to the conversion reaction of SnO₂ to the metallic Sn and Li₂O, as described in equation 4.2.2.1^{42,43,44,45}. The subsequent broad cathodic peak below 0.5 V reveals the synergetic effects from the successive formation of Li_xSn (0<x<4.4) alloys (equation 4.2.2.2), lithium intercalation into the graphene layers and the formation of solid electrolyte interphase (SEI) film at the surface of the working electrode⁴⁶. Correspondingly, in the following charge process, a weak anodic shoulder peak at 0.2 V can be probably assigned to the reversible Li extraction from the expended layers of graphene⁴¹. The predominant anodic peak positioned at 0.55 V corresponds to the dealloy of as-formed Li_xSn compounds^{15,47,48}. It is interesting to find a very wide anodic park cross a voltage range between 1.0 and 2.2 V. As reported in literatures^{49,50}, such electrochemical performance in CV measurements results from the partially reversible reaction in reaction 4.2.2.1. Accordingly, a wide peak within the range of 0.75-1.5 V appears in the second CV cycle instead of the initial cathodic peak, supporting our speculation of the partial reversibility

of SnO_2 -Sn conversion. The following two cathodic peaks located at 0.2 and 0.01V are ascribed to the process of Sn alloyed with lithium ions and intercalation of lithium ions into graphene layers along with continuous growth of SEI film, respectively. The CV profiles in the subsequent cycles are almost identical to each other after the initial electrochemical activation of SnO_2 @Graphene composite anode, indicating its excellent electrochemical reversibility. SnO_2 @Graphene composite anode in significantly manifest the mutually beneficial relationship of graphene and SnO_2 anode materials, resulting in satisfactory electrochemical performances of the composite anode.

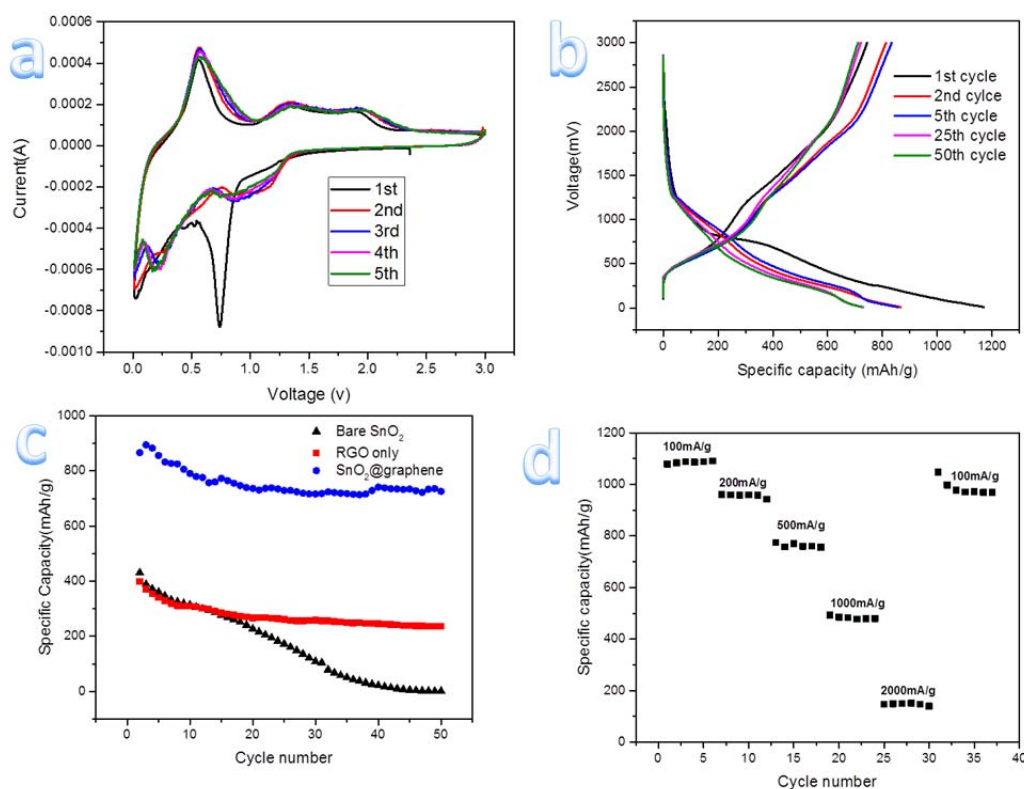


Fig. 4.2.2.4 a) Cyclic Voltammetry of SnO_2 @Graphene composite anode 1st to 5th cycle in the voltage range of 0.01v to 3v, at the scan rate of 0.1mv/s. b) Galvanostatic charge/discharge profiles of the 1st, 2nd, 5th, 25th, and 50th cycles at the current density of 500mA g⁻¹ of SnO_2 @Graphene composite anode; c) Cycling performance of bare SnO_2 , bare RGO and SnO_2 @Graphene composite anode at the current density of 500mA g⁻¹; d) rate performance of Free standing SnO_2 @Graphene composite anode

Fig. 4.2.2.4 b presents the galvanostatic charge/discharge profiles of $\text{SnO}_2@\text{Graphene}$ composite anode at 1st, 2nd, 5th, 25th, and 50th cycles at a current density of 500 mA g^{-1} between 0.01 and 3.0 V. This composite anode can deliver specific discharge and charge capacities of 1169 and 744 mA g^{-1} in the first cycle, respectively, with an initial columbic efficiency of 63.6%. The initial irreversible capacity is attributed to the undesirable formation of SEI film and the consumption of lithium ions to form Li_2O during the conversion reaction from SnO_2 to metallic Sn in the first discharge process. The voltage plateaus of discharge and charge curves are highly consistent with the cathodic and anodic peaks in CV measurements. As shown in Fig. 4.2.2.4 c, the $\text{SnO}_2@\text{Graphene}$ composite anode reveals much higher specific capacity and better cycling stability in comparison with bare RGO and SnO_2 anodes. The SEM image in Fig. 4.2.2.2 b demonstrates the structure of $\text{SnO}_2@\text{Graphene}$ composite material, in which numerous SnO_2 nanoparticles are tripped between wrinkled graphene layers. Such fabrication significantly contributes to improved cycleability of SnO_2 anode materials, because the pristine RGO anode exhibits outstanding cycling performance in Fig.4c, while the bare SnO_2 anode significantly loses its capacity after 20 cycles. After initial five cycles, $\text{SnO}_2@\text{Graphene}$ anode material shows the columbic efficiencies of approximately 100% in subsequent cycles, and retains a capacity of 726 mAh g^{-1} in the 50th cycle, corresponding to the capacity retention of 97.6%

Accordingly, Fig. 4.2.2.4 d reveals the rate capability of free-standing $\text{SnO}_2@\text{Graphene}$ composite material as the anode at various current densities. The $\text{SnO}_2@\text{Graphene}$ composite anode delivers high capacity of 1085, 958, 758, 480, and 150 mAh g^{-1} at the current density of 100, 200, 500, 1000 and 2000 mA g^{-1} , respectively. The

specific capacity of 1000 mAh g^{-1} can be reversed when the composite anode is cycled back to low current density after rate trials. The remarkable electrochemical performance of $\text{SnO}_2@\text{Graphene}$ composite anode can be attributed to: (1) graphene sheets in the as-fabricated composite film provide multiple functions to act as not only the conductive carbon but also the binder, which can facilitate lithium ion diffusion and charge transfer; (2) As shown in Fig. 4.2.2.2 b, SnO_2 nanoparticles are tightly captured within graphene layers. The flexible graphene framework can serve as an elastic “buffer” to accommodate the volume change, and thus effectively releases the reaction strains during the alloy and dealloy processes of Li_xSn ; and (3) Fig. 4.2.2.4 has demonstrated the significantly enhanced cycling stability of SnO_2 anode materials within $\text{SnO}_2@\text{Graphene}$ composite materials, indicating that graphene sheets are favorable to restrict the pulverization and aggregation of converted metallic Sn particles upon electrochemical cycling^{24,28-30}. On the other hand, SnO_2 nanoparticles between graphene layers with uniform distribution can prevent the restacking of graphene sheets. The expended space between graphene layers is beneficial for accommodation of electrolyte and lithium ions, which may contribute to the unexpected capacity of $\text{SnO}_2@\text{Graphene}$ composite material, higher than the theoretical capacity either of RGO or SnO_2 anode materials. All reasons discussed above come together and result in excellent cycling and rate performance of $\text{SnO}_2@\text{Graphene}$ composite anode.

4.3 Conclusion:

In summary, an anti-solvent precipitation method has been demonstrated as an efficient assembly method to fabricate graphene based free standing, flexible and additive free electrode materials. The fabricated $\text{SnO}_2@\text{Graphene}$ composite was directly

employed as additive free and current collector free anode for high-energy Lithium ion batteries. A specific capacity of 726 mAh g^{-1} (calculated by the total mass) and an area specific capacity of 2.2 mAh cm^{-2} was retained after 50 cycles for $\text{SnO}_2@\text{Graphene}$ composite anode at the high current density of 500 mA/g . $\text{SnO}_2@\text{Graphene}$ composite anode can also deliver a high capacity of 1085, 958, 758, 480, and 150 mAh g^{-1} at the current density of 100, 200, 500, 1000 and 2000 mA g^{-1} , respectively. The high specific capacity and excellent rate capability of the composite anode was enabled by its unique structure. All SnO_2 particles were coated by interconnected wrinkled graphene which result from the synergistic effect of ionic strength and dielectric constant during the assembly process. The graphene matrix not only functions as conductive binder and current collector, but also contributes to the total capacity. The assembly method developed in this study is general, robust and easy to apply on other functional materials rather than battery material, which opens up an easy path to fabricate flexible devices.

4.4 Materials and methods:

Preparation of graphene oxide: Graphene oxide was prepared via improved method⁵¹. Typically a 9:1 mixture of concentrated $\text{H}_2\text{SO}_4/\text{H}_3\text{PO}_4$ (90:10 mL) was added to a mixture of graphite flakes (0.75 g, 1 wt equiv) and KMnO_4 (4.5 g, 6 wt equiv). The reaction was then heated to 50°C and stirred for 12 h. The reaction was cooled to room temperature and poured onto ice (100 mL) with 30% H_2O_2 (1 mL). The obtained slurry was first centrifuged and washed repeatedly with 10% HCl for the removal of Mn^{2+} . Then obtained GO was then washed by acetone to remove the majority of Cl^- . For

complete removal of all the ions, deionized water was used for GO washing until no precipitate was observed when mixing the supernatant after centrifuge and 10mM AgNO₃ solution.

Anti-solvent induced GO wrapping on various particles: Various types of particles (metallic Tin, Tin oxide, element Si and Li_{1.2}Mn_{0.5}Ni_{0.3}Co_{0.3}O₂) of different sizes and shapes were dispersed with GO via ultra-sonication for 15min in 15ml de-ionized water, respectively. LiCl salt (30mM) was directly added to the suspension with additional sonication for 1 min. 60ml acetone was poured into the above suspension at one time shot.

Preparation of SnO₂@graphene free standing electrode: 4mg of SnO₂ (Sigma Aldrich 549657) was dispersed with 8.8mg GO in 15ml de-ionized water for 15min. 20mg LiCl salt was directly added. The suspension was then sonicated for additional 1 min. 60ml acetone was poured into the above suspension at one time shot. The resulted mixture was then collected via vacuum filtration (15mm in diameter) using PTFE filter paper with the pore size of 0.2μm (Sterlitech). The filter cake was then dry out in the vacuum oven at 60⁰C for 2 hours. The composite film was then peeled off from the PTFE filter paper using tweezer. The conductivity of the composite film was recovered via thermal annealing (temperature was increase step by step, one hour stay at 100⁰C, 200⁰C, 300⁰C, 400⁰C, respectively then 3 hours stay at 500⁰C) . Typical mass of the electrode is 5.6mg after thermal annealing, corresponding to loading density of 3.1mg/cm².

Sample characterization: Lateral dimension and thickness of the graphene oxide was studied using a Nanoscope IIIa Multimode scanning probe microscope system (Digital Instruments, Bruker) with a J scanner operated in the “Tapping Mode”. Structure and morphology were observed using a Hitachi S4800 field emission scanning electron

microscopy (SEM, STEM). Crystallographic structures were examined by a Panalytical X'pert Diffractometer with Cu K α radiation. TGA was performed on a SII STA7300 analyzer at a heating rate of 5°C/min in air.

Electrochemical Measurement: Electrochemical measurements were carried out using CR2025 coin-type cells. The SnO₂@Graphene composite was directly used as the working electrode after thermal annealing. The coin cells were assembled inside a glove box filled with pure argon, using lithium metal as the counter/reference electrode and Celgard3501 as the separator. The electrolyte was 1 M LiPF₆ dissolved in a mixture of ethylene carbonate, dimethyl carbonate and diethyl carbonate and (4:3:3 in volume). Galvanostatic charge-discharge curves of the cells were recorded by MTI BST8-MA-battery analyzer in a voltage range of 0.01 – 3.0 V *vs.* Li/Li⁺. Cyclic voltammetric (CV) curves of cathodes were recorded at a scanning rate of 0.1 mVs⁻¹ between 0.01 and 3 V *vs.* Li/Li⁺, and EIS data were obtained by applying an AC voltage of 5 mV in the frequency range of 0.01–100 kHz using an electrochemical analyzer (CHI 760C).

4.5 References

- 1 Lou, X. W., Li, C. M. & Archer, L. A. Designed synthesis of coaxial SnO₂@ carbon hollow nanospheres for highly reversible lithium storage. *Advanced Materials* **21**, 2536-2539 (2009).
- 2 Wang, X. *et al.* N-Doped Graphene-SnO₂ Sandwich Paper for High-Performance Lithium-Ion Batteries. *Advanced Functional Materials* **22**, 2682-2690 (2012).
- 3 Poizot, P., Laruelle, S., Grugeon, S., Dupont, L. & Tarascon, J. Nano-sized transition-metal oxides as negative-electrode materials for lithium-ion batteries. *Nature* **407**, 496-499 (2000).
- 4 Huang, J. Y. *et al.* In situ observation of the electrochemical lithiation of a single SnO₂ nanowire electrode. *Science* **330**, 1515-1520 (2010).
- 5 Chen, J. & Yano, K. Highly Monodispersed Tin Oxide/Mesoporous Starburst Carbon Composite as High-Performance Li-Ion Battery Anode. *ACS applied materials & interfaces* **5**, 7682-7687 (2013).
- 6 Zhu, J. *et al.* Synergetic approach to achieve enhanced lithium ion storage performance in ternary phased SnO 2–Fe 2 O 3/rGO composite nanostructures. *Journal of Materials Chemistry* **21**, 12770-12776 (2011).
- 7 Kim, W.-S. *et al.* SnO₂@ Co₃O₄ hollow nano-spheres for a Li-ion battery anode with extraordinary performance. *Nano Research* **7**, 1128-1136 (2014).
- 8 Wang, Y. *et al.* Designed hybrid nanostructure with catalytic effect: beyond the theoretical capacity of SnO₂ anode material for lithium ion batteries. *Scientific reports* **5** (2015).
- 9 Courtney, I. A. & Dahn, J. Electrochemical and in situ X-ray diffraction studies of the reaction of lithium with tin oxide composites. *Journal of the Electrochemical Society* **144**, 2045-2052 (1997).
- 10 Lee, S. H., Mathews, M., Toghiani, H., Wipf, D. O. & Pittman, J., Charles U. Fabrication of carbon-encapsulated mono-and bimetallic (Sn and Sn/Sb Alloy) nanorods. Potential lithium-ion battery anode materials. *Chemistry of Materials* **21**, 2306-2314 (2009).
- 11 Wang, D. *et al.* Layer by layer assembly of sandwiched graphene/SnO 2 nanorod/carbon nanostructures with ultrahigh lithium ion storage properties. *Energy & Environmental Science* **6**, 2900-2906 (2013).
- 12 Chen, C. *et al.* Assembling tin dioxide quantum dots to graphene nanosheets by a facile ultrasonic route. *Langmuir* **29**, 4111-4118 (2013).
- 13 Liu, L., An, M., Yang, P. & Zhang, J. Superior cycle performance and high reversible capacity of SnO₂/graphene composite as an anode material for lithium-ion batteries. *Sci Rep* **5**, 9055, doi:10.1038/srep09055 (2015).
- 14 Wang, Y. *et al.* Designed hybrid nanostructure with catalytic effect: beyond the theoretical capacity of SnO₂ anode material for lithium ion batteries. *Sci Rep* **5**, 9164, doi:10.1038/srep09164 (2015).
- 15 Xu, Y., Guo, J. & Wang, C. Sponge-like porous carbon/tin composite anode materials for lithium ion batteries. *Journal of Materials Chemistry* **22**, 9562-9567 (2012).

- 16 Demir-Cakan, R., Hu, Y.-S., Antonietti, M., Maier, J. & Titirici, M.-M. Facile one-pot synthesis of mesoporous SnO₂ microspheres via nanoparticles assembly and lithium storage properties. *Chemistry of Materials* **20**, 1227-1229 (2008).
- 17 Ramasamy, E. & Lee, J. Ordered Mesoporous SnO₂- Based Photoanodes for High-Performance Dye-Sensitized Solar Cells. *The Journal of Physical Chemistry C* **114**, 22032-22037 (2010).
- 18 Liu, G. *et al.* Polymers with tailored electronic structure for high capacity lithium battery electrodes. *Advanced Materials* **23**, 4679-4683 (2011).
- 19 Park, S. J. *et al.* Side-chain conducting and phase-separated polymeric binders for high-performance silicon anodes in lithium-ion batteries. *J Am Chem Soc* **137**, 2565-2571, doi:10.1021/ja511181p (2015).
- 20 Wu, M. *et al.* Toward an ideal polymer binder design for high-capacity battery anodes. *J Am Chem Soc* **135**, 12048-12056, doi:10.1021/ja4054465 (2013).
- 21 Zeng, Y., Zhou, Y., Kong, L., Zhou, T. & Shi, G. A novel composite of SiO₂ 2-coated graphene oxide and molecularly imprinted polymers for electrochemical sensing dopamine. *Biosensors and Bioelectronics* **45**, 25-33 (2013).
- 22 Chen, S., Chen, P., Wu, M., Pan, D. & Wang, Y. Graphene supported Sn-Sb@ carbon core-shell particles as a superior anode for lithium ion batteries. *Electrochemistry Communications* **12**, 1302-1306 (2010).
- 23 Li, X. *et al.* Synthesis of 3D hierarchical Fe₃O₄/graphene composites with high lithium storage capacity and for controlled drug delivery. *The Journal of Physical Chemistry C* **115**, 21567-21573 (2011).
- 24 Zhou, G. *et al.* Graphene-wrapped Fe₃O₄ anode material with improved reversible capacity and cyclic stability for lithium ion batteries. *Chemistry of Materials* **22**, 5306-5313 (2010).
- 25 Zhou, W. *et al.* A general strategy toward graphene@ metal oxide core-shell nanostructures for high-performance lithium storage. *Energy & Environmental Science* **4**, 4954-4961 (2011).
- 26 Park, S., Dikin, D. A., Nguyen, S. T. & Ruoff, R. S. Graphene oxide sheets chemically cross-linked by polyallylamine. *The Journal of Physical Chemistry C* **113**, 15801-15804 (2009).
- 27 Kim, H. *et al.* Graphene-based hybrid electrode material for high-power lithium-ion batteries. *Journal of the Electrochemical Society* **158**, A930-A935 (2011).
- 28 Paek, S.-M., Yoo, E. & Honma, I. Enhanced cyclic performance and lithium storage capacity of SnO₂/graphene nanoporous electrodes with three-dimensionally delaminated flexible structure. *Nano letters* **9**, 72-75 (2008).
- 29 Mai, Y. *et al.* CuO/graphene composite as anode materials for lithium-ion batteries. *Electrochimica Acta* **56**, 2306-2311 (2011).
- 30 Yang, S., Feng, X., Ivanovici, S. & Müllen, K. Fabrication of graphene-encapsulated oxide nanoparticles: towards high-performance anode materials for lithium storage. *Angewandte Chemie International Edition* **49**, 8408-8411 (2010).
- 31 Gao, T. *et al.* Free-standing SnO₂ nanoparticles@ graphene hybrid paper for advanced lithium-ion batteries. *Ceramics International* **40**, 6891-6897 (2014).
- 32 Li, N., Zhou, G., Fang, R., Li, F. & Cheng, H.-M. TiO₂/graphene sandwich paper as an anisotropic electrode for high rate lithium ion batteries. *Nanoscale* **5**, 7780-7784 (2013).

- 33 Chen, Y. *et al.* Aerosol synthesis of cargo-filled graphene nanosacks. *Nano letters* **12**, 1996-2002 (2012).
- 34 Rong, J., Ge, M., Fang, X. & Zhou, C. Solution ionic strength engineering as a generic strategy to coat graphene oxide (GO) on various functional particles and its application in high-performance lithium-sulfur (Li-S) batteries. *Nano letters* **14**, 473-479 (2013).
- 35 Zeugin, J. A. & Hartley, J. L. Ethanol precipitation of DNA. *Focus* **7**, 1-2 (1985).
- 36 Crouse, J. & Amorese, D. Ethanol precipitation: ammonium acetate as an alternative to sodium acetate. *Focus* **9**, 3-5 (1987).
- 37 Li, D., Müller, M. B., Gilje, S., Kaner, R. B. & Wallace, G. G. Processable aqueous dispersions of graphene nanosheets. *Nature nanotechnology* **3**, 101-105 (2008).
- 38 Lerf, A., He, H., Forster, M. & Klinowski, J. Structure of graphite oxide revisited. *The Journal of Physical Chemistry B* **102**, 4477-4482 (1998).
- 39 Szabó, T. *et al.* Evolution of surface functional groups in a series of progressively oxidized graphite oxides. *Chemistry of materials* **18**, 2740-2749 (2006).
- 40 Cote, L. J. *et al.* Graphene oxide as surfactant sheets. *Pure and Applied Chemistry* **83**, 95-110 (2010).
- 41 Wang, G. *et al.* Sn/graphene nanocomposite with 3D architecture for enhanced reversible lithium storage in lithium ion batteries. *Journal of Materials Chemistry* **19**, 8378-8384 (2009).
- 42 Moon, T., Kim, C., Hwang, S.-T. & Park, B. Electrochemical properties of disordered-carbon-coated SnO₂ nanoparticles for Li rechargeable batteries. *Electrochemical and solid-state letters* **9**, A408-A411 (2006).
- 43 Park, M. S. *et al.* Preparation and Electrochemical Properties of SnO₂ Nanowires for Application in Lithium-Ion Batteries. *Angewandte Chemie* **119**, 764-767 (2007).
- 44 Lou, X. W., Chen, J. S., Chen, P. & Archer, L. A. One-pot synthesis of carbon-coated SnO₂ nanocolloids with improved reversible lithium storage properties. *Chemistry of Materials* **21**, 2868-2874 (2009).
- 45 Wen, Z., Wang, Q., Zhang, Q. & Li, J. In Situ Growth of Mesoporous SnO₂ on Multiwalled Carbon Nanotubes: A Novel Composite with Porous-Tube Structure as Anode for Lithium Batteries. *Advanced Functional Materials* **17**, 2772-2778 (2007).
- 46 Chang, C.-C., Liu, S.-J., Wu, J.-J. & Yang, C.-H. Nano-tin oxide/tin particles on a graphite surface as an anode material for lithium-ion batteries. *The Journal of Physical Chemistry C* **111**, 16423-16427 (2007).
- 47 Zhang, W.-M. *et al.* Tin-nanoparticles encapsulated in elastic hollow carbon spheres for high-performance anode material in lithium-ion batteries. *Advanced Materials* **20**, 1160-1165 (2008).
- 48 Deng, D. & Lee, J. Y. Reversible Storage of Lithium in a Rambutan-Like Tin-Carbon Electrode. *Angewandte Chemie International Edition* **48**, 1660-1663 (2009).
- 49 Rai, A. K., Anh, L. T., Gim, J., Mathew, V. & Kim, J. Low temperature synthesis of porous tin oxide anode for high-performance lithium-ion battery. *Electrochimica Acta* **109**, 461-467 (2013).

- 50 Zhang, H., Song, H., Chen, X., Zhou, J. & Zhang, H. Preparation and electrochemical performance of SnO₂@ carbon nanotube core-shell structure composites as anode material for lithium-ion batteries. *Electrochimica Acta* **59**, 160-167 (2012).
- 51 Marcano, D. C. *et al.* Improved synthesis of graphene oxide. *ACS nano* **4**, 4806-4814 (2010).

Chapter 5: Ion Exchange Promoted Phase Transformation of Li-rich Layered Cathode Materials and Related Electrochemical Performance for High-Energy Lithium-Ion Batteries

5.1 Introduction

The rechargeable lithium-ion battery has been demonstrated as a highly effective power supply for electric transportation and portable electronic devices. Performance of lithium ion batteries crucially relies on energy and power densities of electrode materials¹. Recently, tremendous research efforts focus on developing advanced cathode materials, which can offer high energy density and operating voltage, and outstanding cycling stability and rate capability^{2,3,4}. The Mn-based Li-rich layered transition metal oxides have attracted a great deal of research attentions due to their high lithium storage capability and working potential. These cathode materials with the formula of $\text{Li}[\text{Li}_x\text{Mn}_y\text{M}_z]\text{O}_2$ (M= Co and Ni; $x+y+z=1$ and $y>0.5$) can be cycled over a broad voltage range of 2.0 - 4.8 V vs. Li/Li^+ and deliver specific capacities higher than 250 mAh/g, along with providing other merits including low cost, environmental friendliness and safety⁵⁻¹⁸.

$\text{Li}[\text{Li}_{0.2}\text{Mn}_{0.54}\text{Ni}_{0.13}\text{Co}_{0.13}]\text{O}_2$ (marked as LMNCO) belongs to above Li-rich and Mn-rich category. Such material has an impressive theoretical capacity of 321 mAh/g and a high operating voltage up to 4.8 V vs. Li/Li^+ ¹⁸. As reported in literatures⁶⁻⁸, Li-rich layered LMNCO is composed of two integrated components, i.e., the structural

intergrowth of layered lithium-inactive Li_2MnO_3 (space group C2/m) and layered lithium-active $\text{LiMn}_{1/3}\text{Ni}_{1/3}\text{Co}_{1/3}\text{O}_2$ (space group R-3m) at a molar ratio of 1:1 ($0.5\text{Li}_2\text{MnO}_3 \cdot 0.5\text{LiMn}_{1/3}\text{Ni}_{1/3}\text{Co}_{1/3}\text{O}_2$). The high capacity of LMNCO can be achieved via the electrochemical activation of inert Li_2MnO_3 during the initial charge above 4.5 V vs. Li/Li^+ , during which Li_2MnO_3 is decomposed to Li_2O and MnO_2 caused by electrochemical extraction of lithium ions. This process simultaneously results in an irreversible oxygen loss and creation of lithium ion vacancies in the layered structure of LMNCO^{6,10}. As a result, $\text{Mn}^{3+}/\text{Mn}^{4+}$ redox in the activated layered MnO_2 contributes to the higher capacity in subsequent electrochemical cycles. In comparison with the original material, additional capacity contribution can come from the reduced oxidation state of transition metal ions at the end of the initial discharge to 2.0 V vs. Li/Li^+ , due to the existence of oxygen deficiencies in the activated cathode materials. Despite the high capacity resulting from activation of the inert Li_2MnO_3 component, such electrochemical activation leads to a significant irreversible capacity loss, i.e., low columbic efficiency in the initial charge/discharge cycle. Another consequential phenomenon induced by electrochemical activation of Li_2MnO_3 is the unavoidable layered-to-spinel phase conversion in the activated layered LMNCO. Such a phase transition is highly feasible due to structural compatibility of cubic close-packed oxygen arrays between layered and spinel structures^{7,9,13,19,20}. Formation of a cubic spinel phase within the parent layered structure is effectively promoted in the highly-charged state during subsequent electrochemical cycles, in which transition metal ions migrate to reside on vacant lithium ion sites permanently, resulting in irreversible phase transformation to a stable layered-spinel composite phase^{8,21}. Overall, electrochemical activation of Li_2MnO_3 component

causes structural instability and phase transition, which accounts for the inferior rate capability and poor reversibility of Li-rich layered cathode materials⁹.

On the other hand, it has recently been reported that the phase transition in Li-rich layered cathode materials, during and after activating the Li_2MnO_3 component when electrochemically cycled, can significantly contribute to the unexpectedly high-rate capability^{7,8,22}. Both Li_2MnO_3 and $\text{LiMn}_{1/3}\text{Ni}_{1/3}\text{Co}_{1/3}\text{O}_2$ components simultaneously undergo phase conversion from the original layered to reconstructed spinel structures, but through different pathways. Within the Li_2MnO_3 domain, removal of Li^+ and O^{2-} during initial electrochemical activation triggers phase transition from layered Li_2MnO_3 to the spinel phase due to the existence of lithium ion and oxygen vacancies. As a result, layered Li_2MnO_3 transforms to numerous spinel grains integrated in an amorphous matrix⁹. Although such transformation breaks down the parent lattice and induces lattice strains, the newly-formed spinel phase exhibits higher capacity and better rate capability, owing to its lithium-active characteristic, and higher electronic conductivity and facile lithium ion diffusivity⁷. It has been suggested that structural rearrangement within the $\text{LiMn}_{1/3}\text{Ni}_{1/3}\text{Co}_{1/3}\text{O}_2$ region takes place through migration of transition metal ions to lithium ion layers, yielding spinel grains on the surface of a predominantly layered structure during initial electrochemical cycles^{20,21}. Such structural evolution can progress via continuous lithiation and delithiation, and consumes the parent layered phase to grow the spinel phase until a complex layered-spinel composite structure is stabilized^{13,15}. The formation of the spinel phase in Li-rich layered cathode materials has been demonstrated by high resolution STEM observations²¹, high resolution TEM images with selected area electron diffraction (SAED) patterns⁷, in-situ X-ray diffraction patterns¹³, X-ray

absorption spectroscopic and Raman studies^{15,23}, and is also reflected on charge/discharge curves²², differential capacity plots¹⁴, and cyclic voltammetric (CV) profiles^{7,24}. The intergrowth of spinel-layered phases tends to alleviate the electrochemical inferiority of Li-rich layered cathode materials. However, structural details of these phases in the cycled electrodes have not been comprehensively understood yet. The crystal phase of the spinel formed in Li-rich layered oxides is always reported as “spinel” or “spinel-like” phase. The effects of such a phase transformation (whether to improve or deteriorate performance of spinel-layered composite cathodes) are currently under debate. It is very important to explore these effects in order to understand the fundamental electrochemical behavior of the emerging high-capacity Li-rich layered cathode materials.

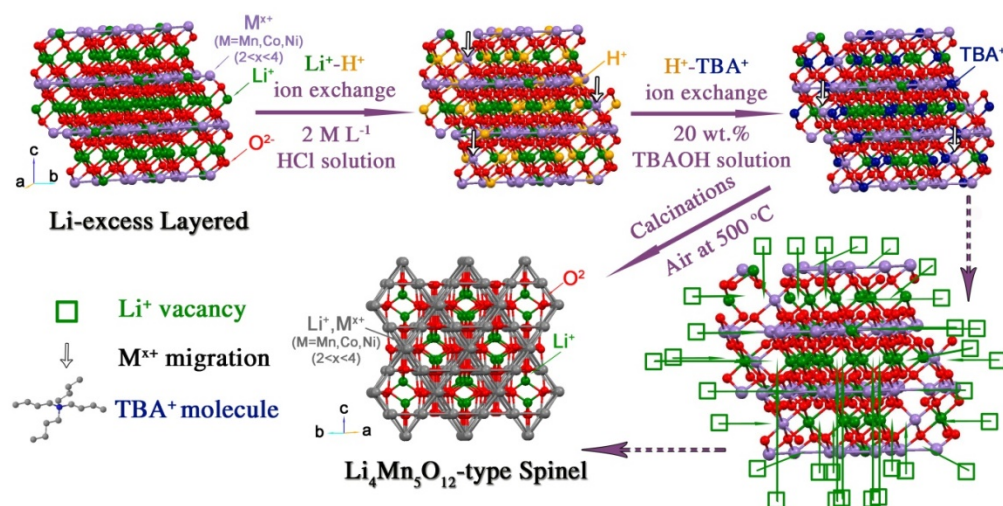
As reported in literatures^{16,25}, Li-rich layered cathode materials can be chemically activated via protonation (H^+ - Li^+ exchange) in an acidic environment, followed by removing H^+ ions in a post-annealing treatment in air. Such *ex-situ* chemical activation also causes the release of Li_2O from the inert Li_2MnO_3 component during H^+ - Li^+ ion exchange to yield lithium-active MnO_2 , and further forms a Mn-based spinel phase after burning away protons by heat treatments. As a result, the activated cathode materials show significantly improved specific capacity and initial columbic efficiency in the first cycle. Although H^+ - Li^+ ion exchange can induce the formation of the spinel phase, the amount of spinel-structured domains is very limited on the surface of Li-rich layered cathode materials. Consequently, the phase transition continuously occurs within partially activated spinel-layered composite cathodes during subsequent electrochemical cycles, giving rise to structural instability and inferior cycleability²⁵. As referred to other ion-

exchange reports^{26,27,28,29}, alkylammonium hydroxides, such as tetrabutylammonium hydroxide ($\text{TBA}^+\cdot\text{OH}^-$) and tetramethylammonium hydroxide ($\text{TMA}^+\cdot\text{OH}^-$), have been extensively used to exfoliate protonated layered materials into two-dimensional (2D) nanosheets. Due to the organic characteristics and larger molecular size of alkylammonium cations in comparison with protons and lithium ions, $\text{TBA}^+\cdot\text{OH}^-$ can be utilized for the second ion exchange ($\text{TBA}^+\cdot\text{H}^+$) of protonated Li-rich layered cathode materials, in order to realize a complete layered form-to-spinel phase conversion.

Herein, we intentionally promote the layered-to-spinel phase transition of Li-rich $\text{Li}[\text{Li}_{0.2}\text{Mn}_{0.54}\text{Ni}_{0.13}\text{Co}_{0.13}]\text{O}_2$ by employing *ex-situ* ion-exchange and post-annealing processes. This approach not only allows the comprehensive study of electrochemical effects resulting from the growth of a spinel phase within Li-rich layered cathode materials, but also offers a feasible route to precisely identify the crystal structure of newly-formed spinel phase. It is interesting to find that the completely-converted material shows a $\text{Li}_4\text{Mn}_5\text{O}_{12}$ -type spinel structure rather than commonly-reported LiMn_2O_4 spinel. Electrochemical performances indicate that introduction of a spinel phase significantly increases the specific capacity up to $\sim 100 \text{ mAh g}^{-1}$ and results in much better rate capability in comparison with original Li-rich layered cathode materials, but reduces the working voltage from 4.0 V to 3.0 V due to the activation of $\text{Mn}^{3+}/\text{Mn}^{4+}$ redox pair.

5.2 Results and discussion

5.2.1 Ex-situ phase transition of Li-excess layered cathode materials promoted by two-step ion exchanges followed by post annealing



Scheme 5.2.1.1 Schematics showing structural reconstruction of Li-excess layered $\text{Li}[\text{Li}_{0.2}\text{Mn}_{0.54}\text{Ni}_{0.13}\text{Co}_{0.13}]\text{O}_2$ to realize a $\text{Li}_4\text{Mn}_5\text{O}_{12}$ -type spinel phase via ion-exchange processes in two steps, followed by calcination.

The phase transition of Li-rich layered $\text{Li}[\text{Li}_{0.2}\text{Mn}_{0.54}\text{Ni}_{0.13}\text{Co}_{0.13}]\text{O}_2$ are comprehensively studied via *ex-situ* chemical ion exchanges, followed by post-annealing treatments (scheme 5.2.1.1). Ion-exchange processes are as follows: First, the protonation of original LMNCO, i.e., $\text{Li}^+ - \text{H}^+$ exchange, is carried out in acidic HCl solution under vigorous magnetic stirring, resulting in a protonated intermediate (marked as LHMNCO). Secondly, the continuous substitution of protons in LHMNCO is performed by using tetrabutylammonium (TBA^+) cations to promote $\text{H}^+ - \text{TBA}^+$ exchange under violent vortex; the resulting derivative is named as LHMNCO TBA. Finally, $\text{TBA}^+ - \text{Li}^+$ ion exchange is taken place on LHMNCO TBA in a basic LiOH solution to tentatively study the

reversibility of ion-exchange procedures, and the final product is denoted as LHMNCO TBA Li.

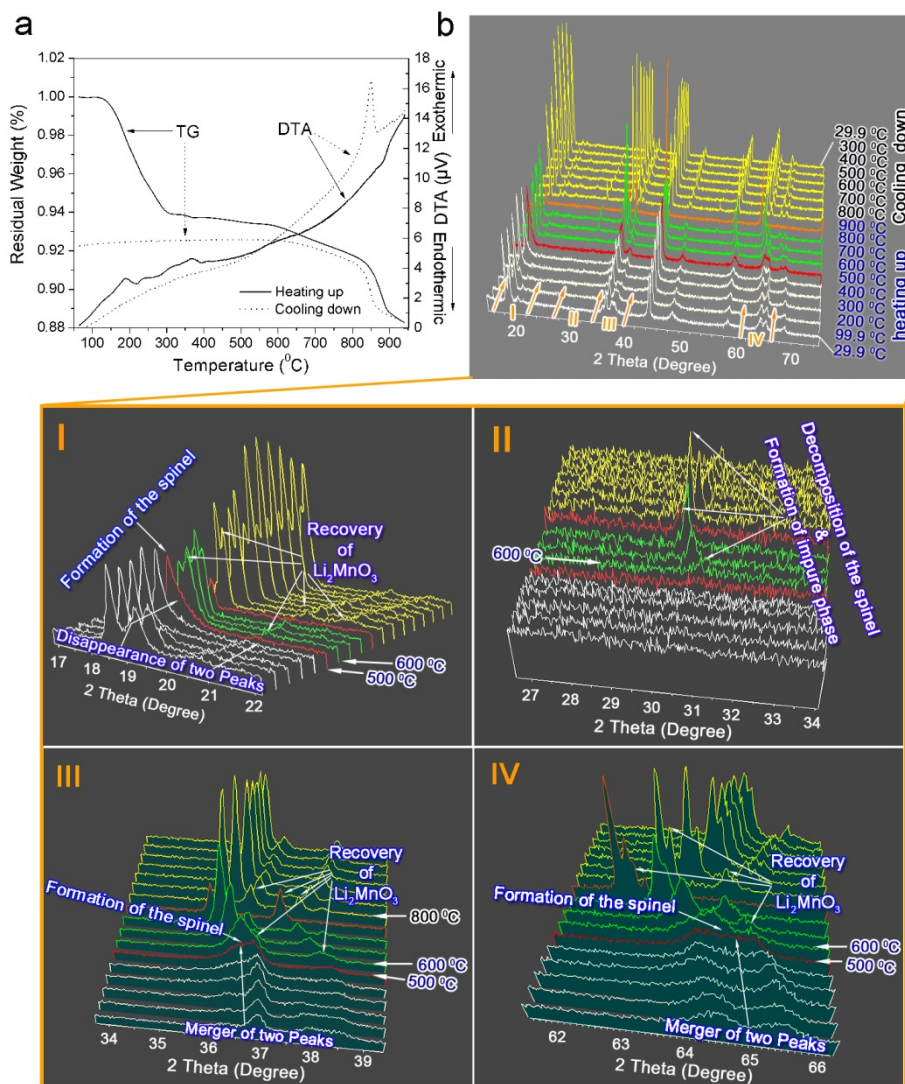


Fig. 5.2.1.1 In situ characterizations to identify phase transition of LHMNCO TBA during heat treatments. (a) TG/DTA curves showing weight loss and heat transfer when LHMNCO TBA is heated from room temperature to 950 $^{\circ}\text{C}$ (solid lines) and cooled back to ambient temperature (dashed lines) in air, (b) in situ XRD patterns of LHMNCO powders when heated to 900 $^{\circ}\text{C}$ and subsequently cooled down to room temperature, with selected portions shown from I to IV.

After ion exchange process, foreign cations (H^{+} and TBA^{+}) occupy the lithium ion sites between the transition metal layers. In order to generate sufficient lithium ion

vacancies within an ion-exchanged layered material at a time and promote the layered-to-spinel phase transition to a maximum extent, we remove the embedded TBA^+ cations, protons and/or other byproducts (e.g., hydrates and OH^- anions), by air sintering. TG/DTA and in-situ XRD were carried out to optimize the sintering temperature. Fig. 5.2.1.1a shows TG/DTA curves of LHMNCO TBA heated from room temperature to 950°C (solid lines), and subsequently cooled to ambient temperature (dashed lines) in air. In order to determine the intermediate phases during the heating-cooling cycle, the dynamic structure of LHMNCO TBA was characterized via in-situ XRD accordingly as shown in Fig. 5.2.1.1b. The major weight loss of 6.1% in TG heating curve between 150 and 300°C is mostly attributed to pyrolysis of TBA^+ ions and removal of residual H^+ , OH^- , hydrates, etc. As a result, numerous vacancies are generated at the original lithium ion sites via burning away foreign substituents, which facilitates and accelerates migrations of transition metal ions into these vacant sites, leading to a distinct layered-to-spinel phase transformation. As temperature increases, one TG plateau with a corresponding broad concave DTA peak appears at 300 - 600°C , indicating possible formation of a stable spinel structure in this temperature range. The in-situ XRD patterns in Fig. 5.2.1.1b demonstrate stabilization of the pure spinel phase at $\sim 500^\circ\text{C}$. The continuous phase conversions can be more easily observed from the enlarged selected 2θ portions (I to IV) in Fig. 5.2.1.1. As shown in portion I, the complete merger of the two peaks at $2\theta = 18 - 20^\circ$ at 300°C results in one characteristic XRD peak representing (111)s crystal planes in the cubic spinel phase. The slight shift of the (111)s peak to a lower 2θ can be ascribed to the thermal expansion effect in the crystal structure at elevated temperature during in-situ XRD characterizations. Furthermore, the intensity of the $(020)_\text{M}$ peak at $2\theta = 20.8^\circ$

continues to decrease when the temperature is increased up to 500°C, indicating consumption of the layered Li_2MnO_3 component. As shown in Fig. 5.2.1.1c, the predominantly ordered layered structure of the $\text{LiMn}_{1/3}\text{Ni}_{1/3}\text{Co}_{1/3}\text{O}_2$ component can be inferred from peak splitting in the $(006)_\text{R}$ - $(012)_\text{R}$ ($2\theta = 36 - 38^\circ$) and $(108)_\text{R}$ - $(110)_\text{R}$ ($2\theta = 64 - 66^\circ$) doublets. In contrast, it is found that these two pairs of well-separated peaks are combined into broad $(222)_\text{S}$ and $(440)_\text{S}$ peaks at 500°C in portions III and IV, respectively, revealing a complete layered-to-spinel phase transformation. Increasing the annealing temperature above 600°C causes undesired decomposition of the newly-formed spinel structure, resulting in a MnCo_2O_4 impurity and recovery of layered Li_2MnO_3 , which is consistent with the continuous mass reduction in the TG curves during the heating segment. Formation of MnCo_2O_4 is apparently detected at 600°C in portion II at $2\theta = 30 - 31^\circ$, and the restored layered Li_2MnO_3 (at $2\theta = 20 - 23^\circ$) is confirmed by the obvious intensity increase of its XRD peaks in portions I, III and IV. Therefore, optimized annealing temperature was determined as 500°C.

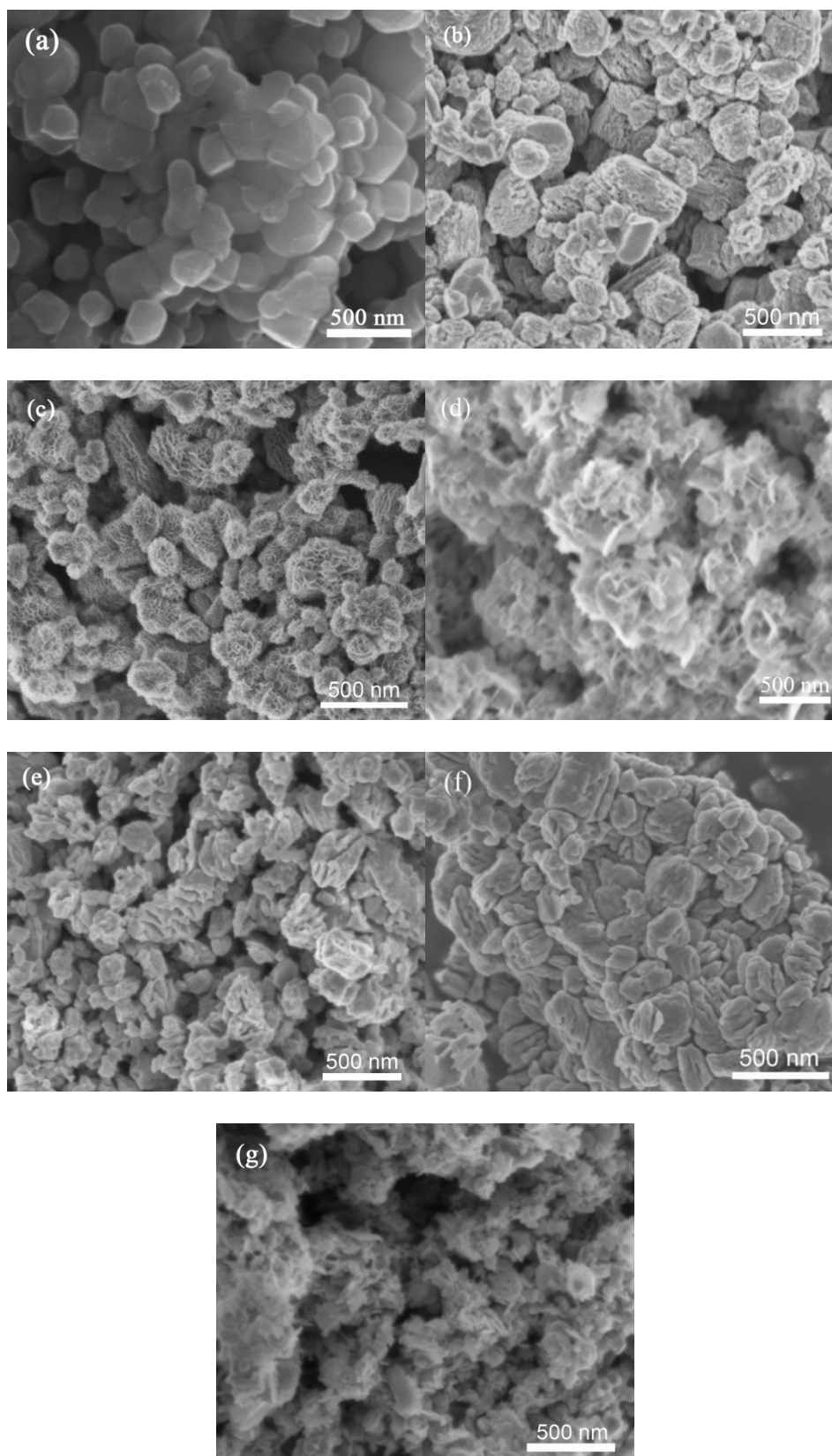
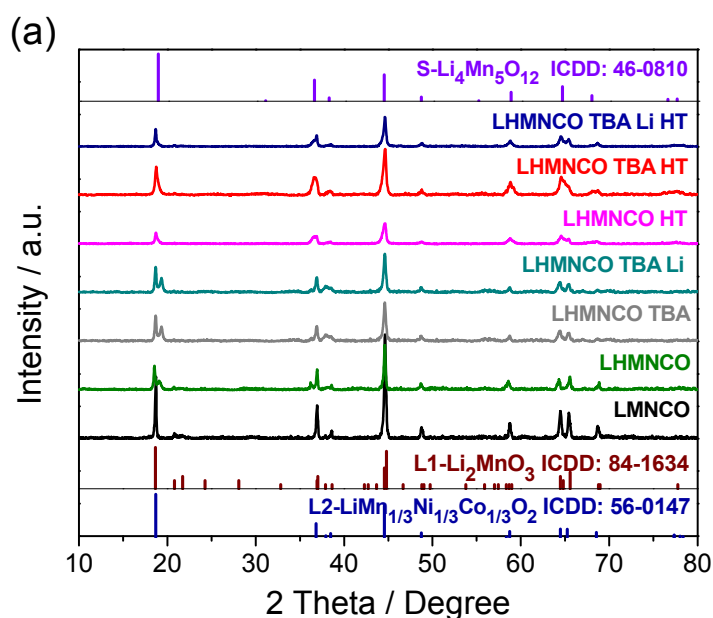


Fig. 5.2.1.2. SEM images of (a) LMNCO, (b) LHMNCO, (c) LHMNCO TBA, (d) LHMNCO TBA Li, (e) LHMNC HT, (f) LHMNCO TBA HT and (g) LHMNCO TBA Li HT.

Three ion-exchanged derivatives were then annealed at 500°C in air, in order to promote the formation of spinel phase under this optimal sintering temperature. Subsequently, the structural phase and electrochemical performances of corresponding materials after heat treatments (LHMNCO HT, LHMNCO TBA HT and LHMNCO TBA Li HT) are evaluated in comparison with the original LMNCO. As shown in Fig. 5.2.1.2, ion-exchange processes and calcinations lead to dramatically morphological changes of different derivatives. The pristine Li-rich $\text{Li}[\text{Li}_{0.2}\text{Mn}_{0.54}\text{Ni}_{0.13}\text{Co}_{0.13}]\text{O}_2$ particles in Fig. 5.2.1.2a exhibit polyhedral shapes with an average particle size of ~250 nm and a distinct aggregation, while H^+ - Li^+ ion exchange in acidic environment results in distinct layered cake-shaped blocks of LHMNCO. We speculate that an ordered layered structure of LMNCO would induce formation of a multilayer morphology in LHMNCO (Fig. 5.2.1.2b). As reported in literatures^{26,29,31}, protonation is the prerequisite for the second H^+ - TBA^+ ion-exchange process. After shaking the as-prepared LHMNCO/HCl mixture (i.e., LHMNCO powders dispersed in HCl solution after protonation) in a TBA·OH aqueous solution at a volumetric ratio of 1:5 via violent vortexes, the collected LHMNCO TBA shows exquisite nanoflower-shaped particles (Fig. 5.2.1.2c). Each particle is composed of numerous ultrathin nano-petals. This phenomenal morphology change can probably be attributed to the synergistic effects of the TBA-assisted exfoliation and the turbulence-induced reaction environment. It is interesting that further Li^+ - TBA^+ ion

exchange in a basic solution extensively unfolds petals of LHMNCO TBA nanoflowers into nanosheet stacks of LHMNCO TBA Li as shown in Fig. 5.2.1.2d. Fig. 5.2.1.2e-g reveal the effects of post-heat treatments on tailoring morphologies of ion-exchanged derivatives, which apparently cause aggregations and coarse structures of LHMNCO HT, LHMNCO TBA HT and LHMNCO TBA Li HT, respectively, after the removal of H^+ and TBA^+ ions, along with other byproducts, such as H_3O^+ and OH^- .



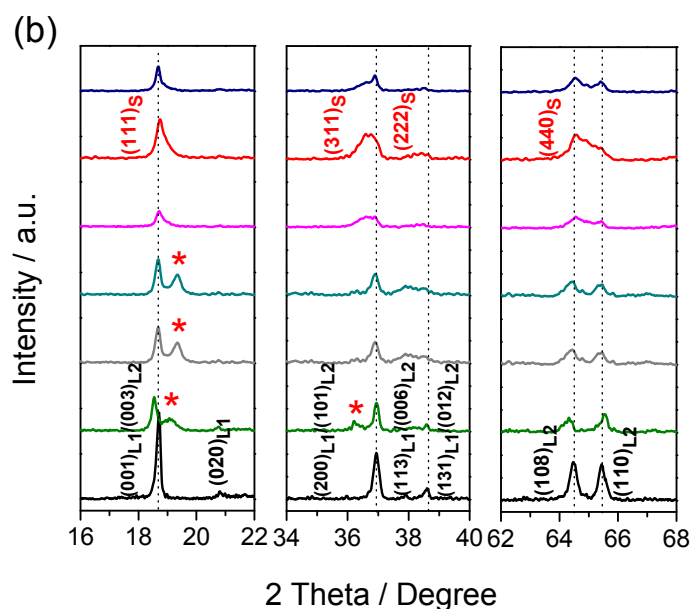


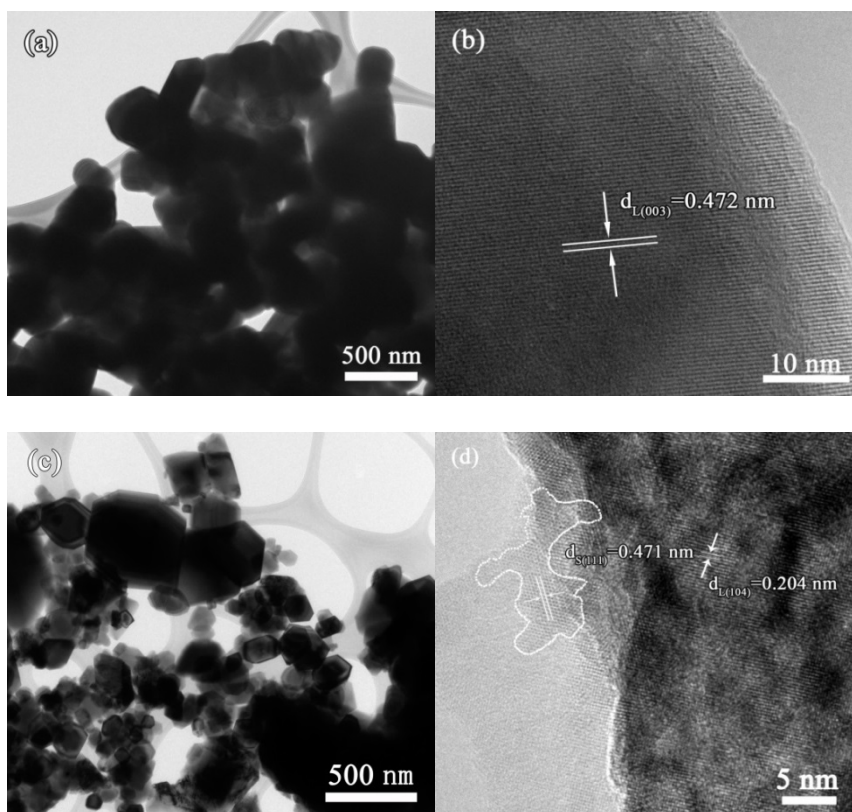
Fig. 5.2.1.3 XRD patterns of pristine Li-rich layered $\text{Li}[\text{Li}_{0.2}\text{Mn}_{0.54}\text{Ni}_{0.13}\text{Co}_{0.13}]\text{O}_2$ nanoparticles and corresponding derivatives in (a) full 2θ range and (b) enlarged 2θ portions between $16\text{--}22^\circ$, $34\text{--}40^\circ$ and $62\text{--}68^\circ$. LMNCO: pristine $\text{Li}[\text{Li}_{0.2}\text{Mn}_{0.54}\text{Ni}_{0.13}\text{Co}_{0.13}]\text{O}_2$ nanoparticles; LHMNCO: LMNCO treated in 2M HCl solution for protonation; LHMNCO TBA: protonated LHMNCO shaken in TBA·OH solution via violent vortex; LHMNCO TBA Li: LHMNCO TBA treated in 1M LiOH solution for Li^+ -TBA $^+$ ion exchange; LHMNCO HT, LHMNCO TBA HT and LHMNCO TBA Li HT: LHMNCO, LHMNCO TBA and LHMNCO TBA Li sintered at 500°C in 3h, respectively.

Accordingly, the phase transition and structural reconstruction accompanying with morphology evolution from initial layered LMNCO to different converted derivatives have been studied from XRD patterns and TEM observations in Fig. 5.2.1.3 and Fig. 5.2.1.4, respectively. In good agreement with other XRD patterns of Li-rich layered materials^{7,8,17,18}, pristine LMNCO in Fig. 5.2.1.3 a exhibits typical XRD peaks showing intergrowth of monoclinic Li_2MnO_3 with C2/m symmetry and rhombohedral $\text{LiMn}_{1/3}\text{Ni}_{1/3}\text{Co}_{1/3}\text{O}_2$ with R-3m symmetry within an ordered layered structure⁷. Two peak splits of $(006)_{\text{L}2}$ - $(012)_{\text{L}2}$ reflections at $2\theta = 36 - 38^\circ$ and $(108)_{\text{L}2}$ - $(110)_{\text{L}2}$ reflections at $2\theta = 64 - 66^\circ$ are characteristic of the predominant layered structure of $\text{LiMn}_{1/3}\text{Ni}_{1/3}\text{Co}_{1/3}\text{O}_2$.

The weak $(020)_{L1}$ reflection at $2\theta = 20 - 23^\circ$ is characteristic of the layered Li_2MnO_3 phase, the superstructure being grown within the parent layered structure¹⁷. The integrated growth of these two layered components can be inferred from the other five peaks at $2\theta = 18.7^\circ, 36.9^\circ, 37.9^\circ, 38.5^\circ$ and 44.5° , which combine diffraction effects from $(001)_{L1}/(003)_{L2}$, $(200)_{L1}/(101)_{L2}$, $(113)_{L1}/(006)_{L2}$, $(131)_{L1}/(012)_{L2}$, and $(202)_{L1}/(104)_{L2}$, respectively. In contrast, the XRD pattern of LHMNCO shows a spinel-like impure phase marked with asterisks, which is consistent with results reported in the literatures^{7,22}. As such, the merger of well-separated $(113)_{L1}/(006)_{L2}$ and $(131)_{L1}/(012)_{L2}$ doublets indicates a certain degree of distortion in the layered structure, while the peak splits of $(108)_{L2}$ - $(110)_{L2}$ pair are preserved, showing that the layered structure is mainly retained in the protonated intermediate²². Furthermore, XRD pattern of LHMNCO TBA powder indicates the growth of spinel-like phase within the parent layered structure during $\text{TBA}^+ - \text{H}^+$ exchange, since the intensity of one representative XRD peak at $2\theta = 19.3^\circ$ (marked with an asterisk in LHMNCO) from the newly-formed spinel phase increases. Structural compatibility of cubic close packed oxygen arrays between layered and spinel configurations is the principal factor that facilitates phase transition in Li-rich layered transition metal oxides, via migration of transition metal ions into lithium ion layers when lithium ion vacancies exist during ion-exchange processes^{13,20}. LHMNCO TBA Li shows identical XRD pattern to that of LHMNCO TBA, indicating that limited reversibility of phase transition. However, peak splitting of $(108)_{L2}$ - $(110)_{L2}$ doublets in XRD patterns reveal the prominent layered structure of ion-exchanged derivatives, although the spinel phase has been detected. Post-annealing treatment has been demonstrated as an effective way to remove H^+ and TBA^+ substituents in air, resulting in the generation of

corresponding Li^+ vacancies in lithium layers³⁰. Such facile process can accelerate the diffusion of transition metal ions into lithium ion sites, and thus promote the layered-to-spinel phase transition. The enlarged selected 2θ portions in Fig. 5.2.3 b at $2\theta=16-20^\circ$, $34-40^\circ$ and $62-68^\circ$ illustrate the phase conversion when different ion-exchanged samples are subjected to air calcinations. The merge of two separate peaks around $2\theta=19^\circ$ into one peak occurs for LHMNCO, LHMNCO TBA and LHMNCO TBA Li, respectively, indicating dramatic phase transitions resulting from the removal of foreign H^+ and TBA^+ cations during the sintering. It is surprising to find that the coupled $(108)_{\text{L2}}-(110)_{\text{L2}}$ pair of LHMNCO TBA has merged into to one broad peak for LHMNCO TBA HT with a lower 2θ position, while LHMNCO HT and LHMNCO TBA Li HT still show distinguishing peak splits of $(108)_{\text{L2}}-(110)_{\text{L2}}$ between $2\theta=62^\circ$ and 64° . As mentioned before, the peak split of $(108)_{\text{L2}}-(110)_{\text{L2}}$ doublets is the dominant characteristic of layered structure, which is distinguished from the spinel phase showing the $(440)_{\text{s}}$ reflection at the same position. As a result, XRD pattern of LHMNCO TBA HT can be indexed to the spinel $\text{Li}_4\text{Mn}_5\text{O}_{12}$ phase with a $Fd-3m$ space group, indicating the complete layered-to-spinel phase transition from original Li-rich layered LMNCO to $\text{Li}_4\text{Mn}_5\text{O}_{12}$ -type spinel compound after ion exchange and heat treatments. In contract, XRD patterns of LHMNCO HT and LHMNCO TBA Li HT both reveal the coexistence of layered and spinel phases (Fig. 5.2.1.3). It is suggested that a second TBA^+-H^+ ion exchange is crucial to realize a complete phase conversion. We speculate that due to the larger size of TBA^+ cations than protons, TBA^+ substituents can increase c -axis of ion-exchanged layered derivative in comparison with the effect from H^+ ions, which will increase the structure instability that significantly facilitate migrations of transition metal ions when TBA^+ are burned away in

air calcinations. On the other hand, Li^+ can be partially restored in the lithium layers through the Li^+ - TBA^+ ion exchange. Therefore, incomplete phase transition was observed for LHMNCO TBA Li HT.



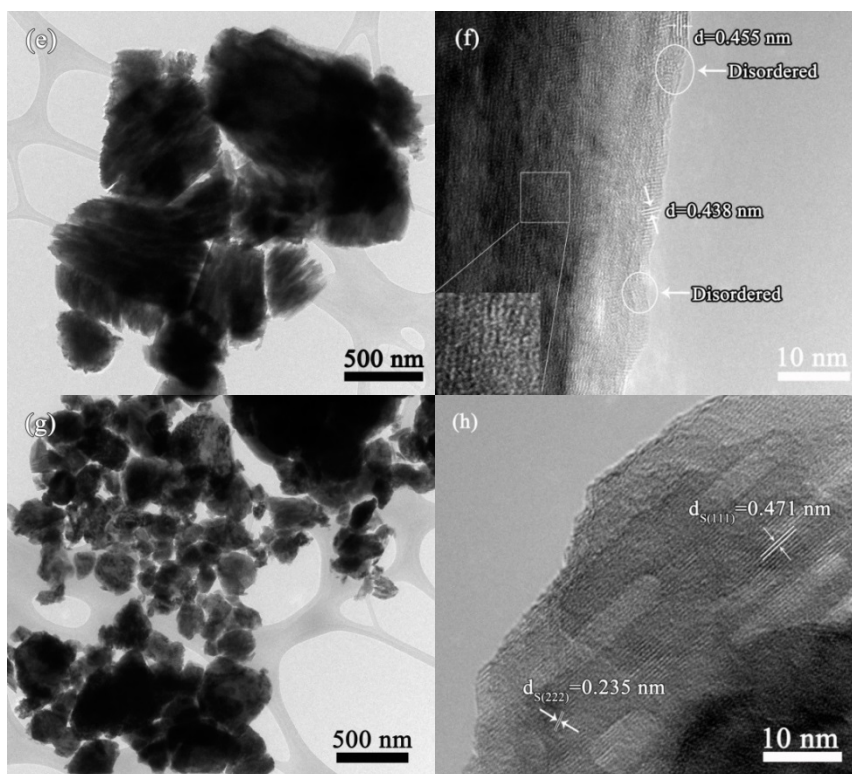


Fig.5.2.1.4. TEM and HRTEM images of (a and b) LMNCO, (c and d) LHMNCO, (e and f) LHMNCO TBA, and (g and h) LHMNCO TBA HT.

Fig. 5.2.1.4 shows the structural reconstruction during the complete phase transition from the pristine layered LMNCO to the converted $\text{Li}_4\text{Mn}_5\text{O}_{12}$ -type LHMNCO TBA HT spinel via TEM observations. In consistence with SEM image in Fig. 5.2.1.2 a, LMNCO nanoparticles have the solid structure with an average particle size of ~ 250 nm. The lattice fringe as shown in Fig. 5.2.1.4b indicates the high crystallinity of pristine Li-rich layered materials, due to the high synthetic sintering temperature at 900°C . The characteristics of overlapped sheets can be observed in Fig. 5.2.1.4c of LHMNCO after $\text{H}^+ - \text{Li}^+$ ion exchange in an acidic HCl solution. The formation of spinel phase during this process at the surface of particle is identified in HRTEM image (Fig. 5.2.1.4d), which is

in agreement with XRD results in Fig. 5.2.1.3. The continuous $\text{TBA}^+ \text{-H}^+$ ion exchange not only tailors LHMNCO TBA to nanoflower-like shapes, but also generates porous structure as shown in Fig. 5.2.1.4 e. Furthermore, due to the violent exfoliation effect of TBA^+ cations, HRTEM image in Fig. 5.2.1.4 f shows disordered lattice fringes both at the surface and in the bulk of LHMNCO TBA; the other reason leading to such disordered structure possibly results from the partial decomposition of organic TBA^+ cations under the attack of high-energy electron beam during HRTEM observations. On the other hand, fringes with the smaller d -space ($d=0.455$ and 0.438 nm in Fig. 5.2.1.4f) at the surface of the specimen may also be attributed to the partial decomposition of TBA^+ substituents. As shown in Fig. 5.2.1.2c and 5.2.1.2f, mono-dispersive LHMNCO TBA nanoflowers convert to LHMNCO TBA HT particles with irregular shapes after post-annealing processes due to the fold of nanopetals. Accordingly, the removal of TBA^+ cations also contributes to the porous structure of LHMNCO TBA HT as shown in TEM image (Fig. 5.2.1.4g). In agreement with the XRD result in Fig. 5.2.1.3, HRTEM image in Fig. 5.2.1.4h shows the spinel crystal structure of LHMNCO TBA HT with a d -space of $(111)_s$ equal to 0.471 nm. In general, *ex-situ* ion- exchange and heat treatments result in the complete phase transition from the layered LMNCO to a $\text{Li}_4\text{Mn}_5\text{O}_{12}$ -type spinel material, along with intriguing morphological and structural evolutions.

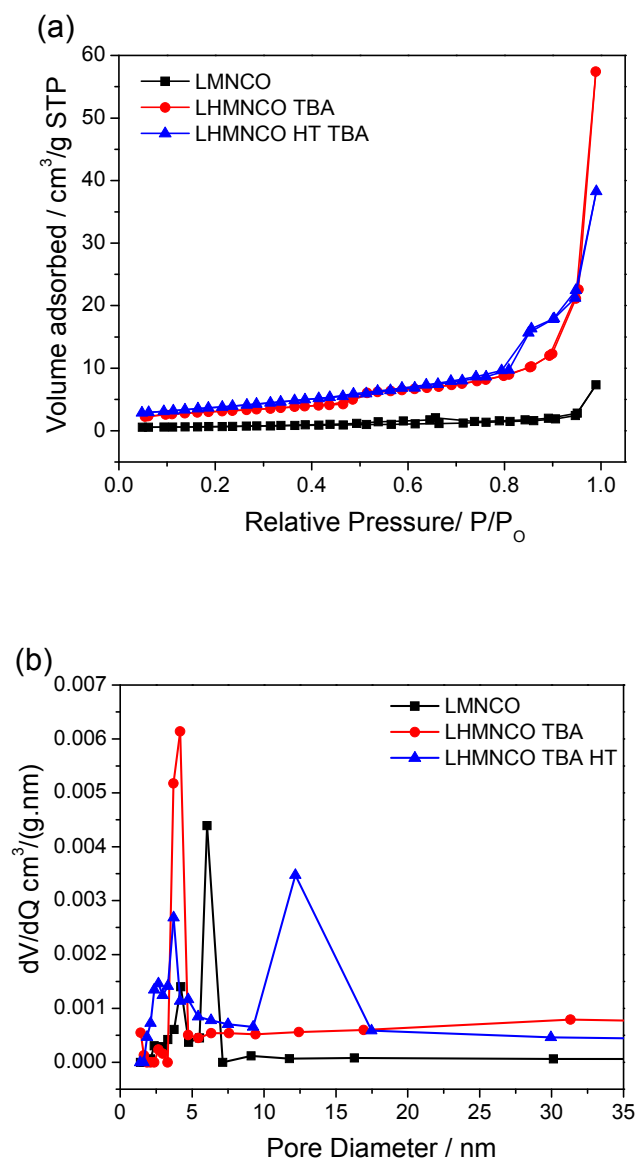


Fig. 5.2.1.5. (a) Nitrogen adsorption/desorption isotherms and (b) corresponding pore size distributions of LMNCO and LHMNCO TBA and LHMNCO TBA HT.

The nitrogen adsorption and desorption isotherms and pore size distributions of pristine Li-rich layered LMNCO, ion-exchanged LHMNCO TBA and annealed LHMNCO TBA HT are shown in Fig. 5.2.1.5a and 5b, respectively. The corresponding porous characteristics in terms of surface area, pore volume and relative pore size are summarized in Table 5.2.1, along with Li/Mn/Ni/Co ratios of three samples. It is clear

that substitution of Li^+ ions within LMNCO by H^+ cations, followed by continuous replacement with TBA^+ cations results in significantly increased surface area to $11.109 \text{ m}^2 \text{ g}^{-1}$ of LHMNCO TBA, almost four times higher than that of original LMNCO particles ($2.327 \text{ m}^2/\text{g}$), which can be attributed to the exfoliation effect from TBA^+ cations as shown in SEM (Fig. 5.2.2c) and TEM (Fig. 5.2.1.4e) images^{27,31}. Accordingly, LHMNCO TBA also has a larger pore volume of $8.880\text{e}^{-2} \text{ cm}^3 \text{ g}^{-1}$ in comparison with $1.133\text{e}^{-2} \text{ cm}^3 \text{ g}^{-1}$ from LMNCO nanoparticles. Both SEM and TEM observations indicate that the pore volume of LMNCO powder is from special gaps between numerous agglomerated LMNCO nanoparticles (Fig. 5.2.1.2a and Fig. 5.2.1.4a), while the higher pore volume of LHMNCO TBA mostly arises from the porous structure of individual LHMNCO TBA nanoflowers (Fig. 5.2.1.2c and Fig. 5.2.1.4e). Therefore, agglomerated LMNCO nanoparticles give rise to a relatively higher pore size distribution of $\sim 6 \text{ nm}$ in Fig. 5.2.1.4b in comparison with $\sim 4 \text{ nm}$ from LHMNCO TBA nanoflowers with monodisperse characteristic. As aforementioned in XRD characterizations in Fig. 5.2.1.3, the post-annealing treatment plays a crucial role to realize a complete layered-to-spinel phase transition, and the morphological and structural changes have been observed in SEM (Fig. 5.2.1.2f) and TEM (Fig. 5.2.1.4g) images, respectively. As a result, sintering LHMNCO TBA contributes to further increased surface area to $13.725 \text{ m}^2 \text{ g}^{-1}$ of LHMNCO TBA HT. Its reduced pore volume is probably due to the folded nanopetals to form an internal porous structure (Fig. 5.2.1.4 g) and the obvious aggregation (Fig. 5.2.1.2 f) after post-heat treatment, resulting in two pore size distributions of ~ 3 and $\sim 12 \text{ nm}$ in Fig. 5.2.1.5b. The chemical compositions of these three samples are compared in Table 5.2.1 in the form of Li/Mn/Ni/Co ratios. In comparison with the theoretical ratio of

Li/Mn/Ni/Co=1.2/0.54/0.13/0.13, the as-prepared LMNCO shows less quantity of lithium component, which can be assigned to the lithium loss during air calcinations at 900°C. After two step ion exchanges via H^+ - Li^+ and TBA^+ - H^+ replacements, LHMNCO TBA preserves 52.7% of the original lithium ions in LMNCO. As reported in the literature²⁹, layered transition metal oxides can be fully exchanged and teared into transition metal oxide nanosheets. In our case, the partial ion exchange possibly is attributed to the formation of spinel phase at the surface of layered derivatives as shown in XRD results (Fig. 5.2.1.3) and HRTEM image (Fig. 5.2.1.4d). The detectable Ni loss in LHMNCO TBA after the ion-exchange processes may result from the cationic Li^+ - Ni^{2+} disorder in LMNCO. Consequently, a few Ni^{2+} ions occupied in lithium sites in the lithium layer are replaced with H^+ and TBA^+ cations. No significant change in chemical composition after the heat treatment, resulting in Li/M (M=Mn+Ni+Co)=0.75. Such value is much close to the Li/Mn ratio of 0.8 in $Li_4Mn_5O_{12}$ spinel in comparison with 0.5 of $LiMn_2O_4$ spinel, which is consistent with the XRD result being indexed to $Li_4Mn_5O_{12}$ -type spinel for LHMNCO TBA HT. In short summary, *ex-situ* ion-exchange processes along with post-heat treatments offer a feasible approach not only to tailor morphology and structure of Li-rich layered transition metal oxides, but also to control the phase evolution between layered and spinel phases. We speculate that the nanoarchitected LHMNCO TBA HT spinel material can benefit for facile electrolyte penetration and accommodation, maximized electrochemical sites and reaction strain release during lithiation and delithiation, and thus are favorable for lithium ion diffusion and structural stability; LHMNCO TBA HT with a pure spinel phase and porous structure is expected to exhibit enhanced rate capability and cycleability as compared with the pristine Li-rich layered

LMNCO, and integrated composite LHMNCO HT and LHMNCO TBA Li HT with an intergrowth of layered and spinel phases.

Table 5.2.1. Porous characteristics and elemental composition of LMNCO, LHMNCO TBA and LHMNCO TBA HT.

Samples	Porous characteristics			ICP elemental compositions			
	Surface area (m ² g ⁻¹)	Pore volume (cm ³ g ⁻¹)	Pore size (nm)	Li	Mn	Ni	Co
Pristine LMNCO	2.327	1.133e-02	~6	1.111	0.540	0.129	0.128
Ion-exchanged LHMNCOTBA	11.109	8.880e-02	~4	0.586	0.540	0.119	0.126
Annealed LHMNCO TBA HT	13.725	5.921e-02	~3 & ~12	0.585	0.540	0.118	0.126

5.2.2 Electrochemical evaluation of final spinel cathode material for high capacity

Lithium ion battery

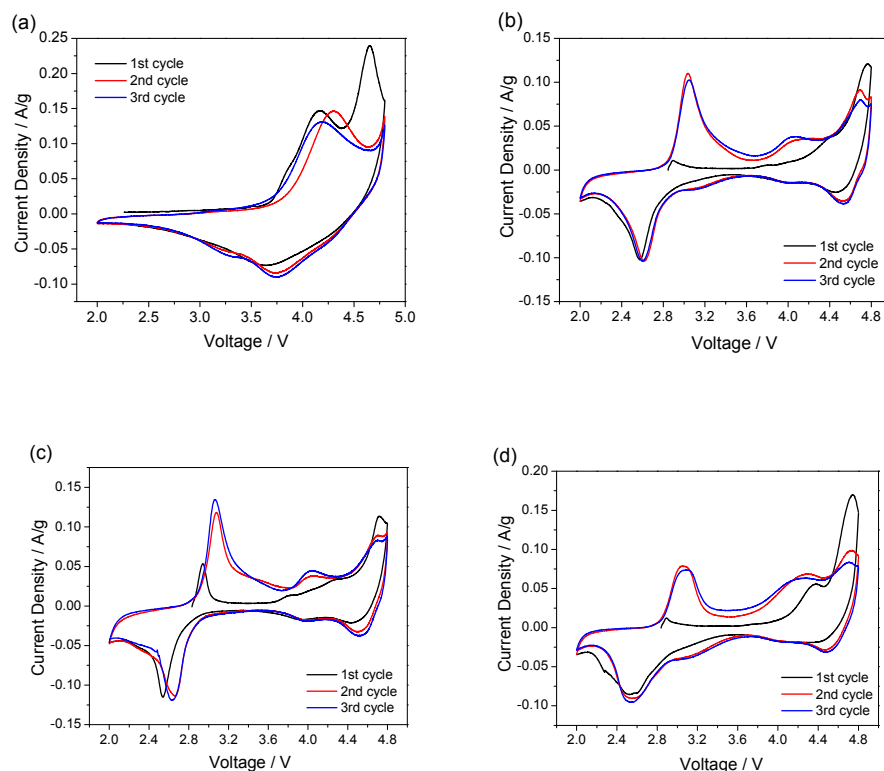


Fig. 5.2.2.1 Cyclic voltammetric (CV) curves of (a) LMNCO, (b) LHMNCO HT, (c) LHMNCO TBA HT and (d) LHMNCO TBA Li HT in the first three cycles at a scanning rate of 0.1 mV/s in a voltage range of 2.0-4.8 V vs. Li/Li⁺.

The cyclic voltammetric (CV) measurements of LHMNCO HT, LHMNCO TBA HT and LHMNCO TBA Li HT are carried out in comparison with the pristine LMNCO, in order to study electrochemical properties related to phase transitions from Li-rich layered (LMNCO) to either layered-spinel (LHMNCO HT and LHMNCO TBA Li) or Li₄Mn₅O₁₂-type spinel (LHMNCO TBA HT) phase. Fig. 5.2.2.1 shows the CV curves in first three cycles of four different samples. As shown in Fig. 5a, LMNCO reveals the typical electrochemical characteristics of Li-rich layered cathode materials. The first anodic peak at 4.17 V in the initial charge curve is associated with the oxidation of Ni²⁺ to Ni⁴⁺, followed by Co³⁺ to Co⁴⁺, whereas Mn still remains as tetravalent in LiMn_{1/3}Ni_{1/3}Co_{1/3}O₂ component³². The second anodic peak at 4.66 V corresponds to the

electrochemical activation of inert Li_2MnO_3 component, i.e., the decomposition of Li_2MnO_3 to Li_2O and lithium-active MnO_2 , along with the unavoidable decomposition of electrolyte and the formation of solid electrolyte interphase (SEI) at such high potential $>4.5 \text{ V}^{10}$. Although such electrochemical activation process leads to the low Coulombic efficiency in the first cycle, but significantly results in high capacity of Li-excess layered cathode materials in the successive cycles. Correspondingly, the reduction of $\text{Co}^{4+}/\text{Co}^{3+}$ and $\text{Ni}^{4+}/\text{Ni}^{3+}/\text{Ni}^{2+}$ redox occurs at 3.66 V in the initial discharge curve. In the second cycle, the anodic peak at 4.66 V disappears in comparison with the first cycle, while an additional cathodic peak at 3.26 V appears which can be assigned to the reduction of Mn^{4+} to Mn^{3+} from the as-activated MnO_2 component. The third cycle shows the similar profile to the second cycle in less polarization and higher current density, indicating improved electrochemical reversibility after the electrochemical activation of Li-rich layered LMNCO. It is clear to see that CV curves of LHMNCO HT, LHMNCO TBA HT and LHMNCO TBA Li HT are very similar to each other, but apparently different from that of LMNCO. Those three materials all show the dominant redox pair around 3.0 V in CV curves, together with two minor redox couples located near 4.0 and 4.6 V. Such performance is consistent with the typical electrochemical characteristics of Ni/Co-doped $\text{Li}_4\text{Mn}_5\text{O}_{12}$ -type spinel in a wide voltage range³³. The CV responses of LHMNCO HT, LHMNCO TBA HT and LHMNCO TBA Li HT support XRD results in Fig. 5.2.1.3, which reveal the $\text{Li}_4\text{Mn}_5\text{O}_{12}$ -type spinel structure of newly-formed spinel phase within the original layered structure of LMNCO after ion-exchange and post-annealing processes. The appearance of an anodic peak at $\sim 4.6 \text{ V}$ in the initial CV charges of LHMNCO HT and LHMNCO TBA Li HT indicate the existence of preserved layered

structure, in accordance with XRD characterizations (Fig. 5.2.1.3). In contrast, LHMNCO TBA HT reveals much lower current density of such anodic peak in the first CV charge. Furthermore, an more intensive anodic peak at 2.95 V is generated, which can be attributed to the more complete phase transition of LHMNCO TBA HT in comparison with LHMNCO HT and LHMNCO TBA HT. LHMNCO TBA HT shows identical CV curves of second and third cycles, indicating outstanding electrochemical reversibility of this spinel materials. The predominant redox pair, anodic peak at 3.07 V and cathodic peak at 2.63 V, can be ascribed to oxidation and reduction reactions of $\text{Mn}^{3+}/\text{Mn}^{4+}$ redox pair, related to extraction and insertion of lithium ions on 16c sites in the spinel structure¹. Two small redox couples at ~4.0 and ~4.6 V probably result from the $\text{Co}^{3+}/\text{Co}^{4+}$ and $\text{Ni}^{2+}/\text{Ni}^{3+}/\text{Ni}^{4+}$ redox, respectively.

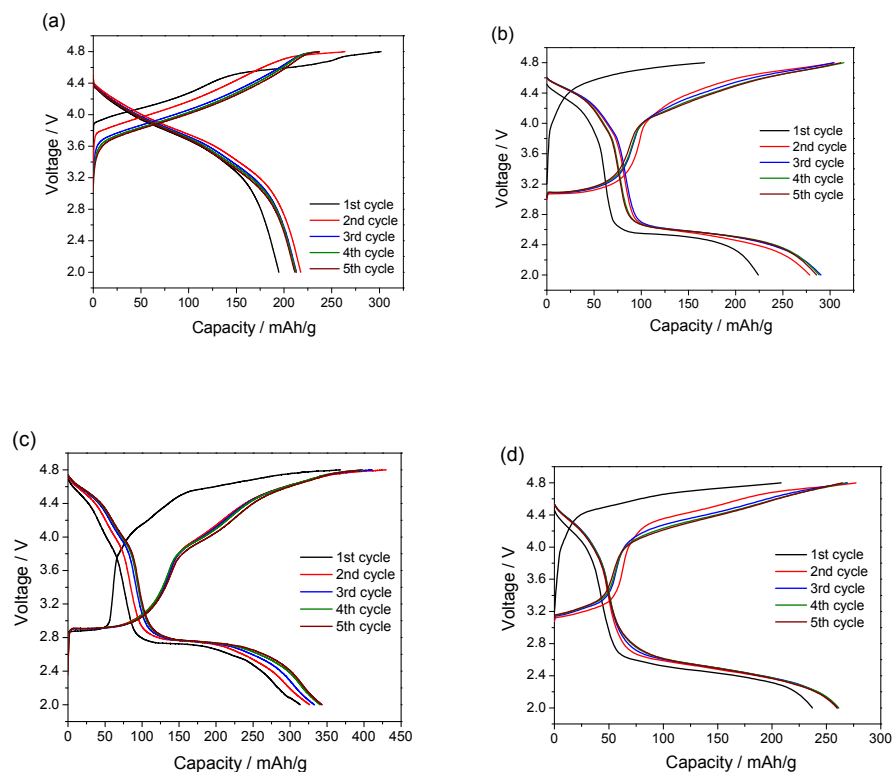


Fig. 5.2.2.2 Charge and discharge curves of (a) LMNCO, (b) LHMNCO HT, (c) LHMNCO TBA HT and (d) LHMNCO TBA Li HT in the first five cycles at a current density of 0.1 C in a voltage range of 2.0–4.8 V vs. Li/Li⁺.

Fig. 5.2.2.2 exhibits charge and discharge curves of four cathodes in the first five cycles at 0.1 C in a voltage range of 2.0–4.8 V vs. Li/Li⁺, which are in well accordance with CV profiles in Fig. 5.2.2.1. It is noticeable that introduction of a spinel phase with Li-rich layered cathode materials can significantly increase the specific capacity. Since charge/discharge curves of the fourth and fifth cycle are almost identical as shown in Fig. 5.2.2.2 a–d for all cathodes, it is suggested that the cathode becomes stable after five electrochemical cycles. The pristine Li-rich layered LMNCO delivers a specific discharge capacity of 211.3 mAh g^{−1} at the fifth cycle with a voltage plateau around 3.7 V, revealing typical electrochemical behavior of Li-rich layered cathode materials. The

XRD result in Fig. 5.2.1.3 a demonstrates the coexistence of layered and spinel phases of LHMNCO HT after *ex-situ* ion-exchange and post-heat treatments, in which the spinel phase is dominant; hence LHMNCO HT shows a higher discharge capacity of 285.8 mAh g⁻¹ but along with a predominant voltage plateau at 2.6 V as well as a minor one at 4.4 V. The former voltage stage is due to the active Mn³⁺/Mn⁴⁺ redox in the spinel component, and the latter probably results from the Co⁴⁺/Co³⁺ and Ni⁴⁺/Ni³⁺/Ni²⁺ redox reactions in the reversed layered component. Furthermore, employing TBA⁺ cations for the second ion exchange of LHMNCO have contributed to the complete phase conversion of Li-rich layered LMNCO, resulting in the spinel LHMNCO TBA HT with the Li₄Mn₅O₁₂-type spinel characteristics (Fig. 5.2.1.3) and a mesoporous structure (Fig. 5.2.1.4g and Fig. 5.2.1.5b). As a result, an unexpectedly high discharge capacity of 343.2 mAh g⁻¹ is achieved in the fifth cycle of LHMNCO TBA HT. There are three voltage plateaus located at 4.6, 4.0 and 2.8 V, respectively, which is distinctly different from the profile of LHMNCO HT, again revealing different structural characteristics between LHMNCO TBA HT and LHMNCO HT. Those three voltage stages can be attributed to reductions from Ni⁴⁺/Ni³⁺/Ni²⁺, Co⁴⁺/Co³⁺ and Mn³⁺/Mn⁴⁺ redox pairs in the spinel structure and are favorable to preserve high-voltage performances of LHMNCO TBA HT. As shown in Fig. 5.2.1.4 g, the nanoarchitected spinel cathode has a porous mesoporous structure that can facilitate accommodation of electrolyte and effectively release strains during lithiation/delithiation processes. The improved capacity may also be attributed to absorption and desorption of lithium ions within the porous structure^{34,35}. In contrast, LHMNCO TBA Li HT shows similar electrochemical performance to LHMNCO HT with the intergrowth of layered and spinel structures, delivering a reduced capacity of

259.9 mAh g⁻¹. This might result from the partially recovered layered structure via Li⁺-TBA⁺ ion exchange of LHMNCO TBA in LiOH aqueous solution.

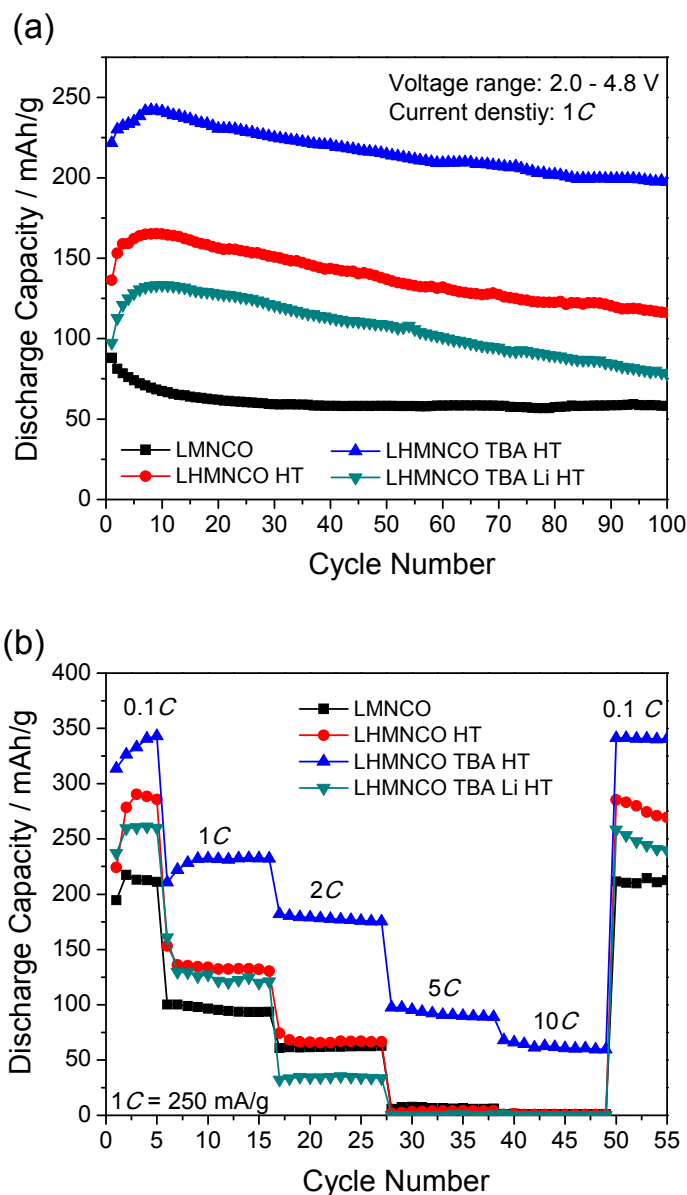


Fig. 5.2.2.3. (a) Cycling performance at 1 C and (d) high-rate performance at different currents of LHMNCO HT, LHMNCO TBA HT LHMNCO TBA Li HT in comparison with the pristine layered LMNCO in a voltage range of 2.0-4.8 V vs. Li/Li⁺.

Fig. 5.2.2.3a and 5.2.2.3b show cycling and high-rate performances of modified LHMNCO HT, LHMNCO TBA HT and LHMNCO TBA Li HT cathodes in comparison with the pristine Li-rich layered LMNCO, respectively. The effects from the introduced spinel phase within the layered LMNCO cathode material on improving specific capacity, cycling stability and rate capability are more phenomenal when cycled at higher current densities. As shown in Fig. 5.2.2.3a, LHMNCO TBA HT can retain a very high discharge capacity of 197.5 mAh g^{-1} with a corresponding capacity retention of 89.1% after 100 electrochemical cycles at 1C, much better than 58.1 mAh g^{-1} and 65.9% of pristine layered LMNCO, 116.1 mAh/g and 85.1% of LHMNCO HT, and 77.9 mAh g^{-1} and 80.0% of LHMNCO TBA Li HT. Moreover, LHMNCO TBA HT delivers initial capacities of 313.6, 267.2, 203.9, 180.7, 126.3, and 89.4 mAh g^{-1} at 0.1, 0.5, 1, 2, 5, and 10C, respectively, as exhibited in Fig. 5.2.2.3b. Such remarkable cyclability and high-rate capability of LHMNCO TBA HT can be attributed to reconstructed spinel phase and hierarchical mesoporous structure for facile accommodation and diffusion of lithium ions, and effectively releasing reaction strains in the “buffer” structure in high porous characteristics. Overall, generation of a spinel phase within Li-rich layered cathode materials can considerably increase the specific capacity and rate capability, but has to sacrifice the working voltage. Doping transition metal cations, such as Ni^{2+} , Co^{3+} and Fe^{3+} ions, can contribute to the high-voltage performance. Ion-exchange method offers a desirable way to obtain enhanced electrochemical performance of Li-rich layered cathode materials.

5.3 Conclusions

This work sheds light on fundamental understanding of layered-to-spinel phase transition and relative electrochemical performances of Li-rich layered cathode materials via *ex-situ* ion-exchange processes, followed by post-annealing treatments. Employing TBA⁺ cations for the second ion exchange of protonated Li-rich layered oxides is critical to realize a complete phase transition, resulting in a Li₄Mn₅O₁₂-type spinel-structured material converted from Li-rich layered Li[Li_{0.2}Mn_{0.54}Ni_{0.13}Co_{0.13}]O₂. Ion-exchange procedure also tailor the morphology and structure of solid Li[Li_{0.2}Mn_{0.54}Ni_{0.13}Co_{0.13}]O₂ nanoparticles into nanostructured spinel material with high surface area and mesoporous porosity. In comparison with the pristine Li-rich layered cathode material, the final converted spinel cathode material with hierarchical porous structure reveals significantly increased specific capacity, better cycling stability and rate capability. This work opens up a new route to maximize electrochemical performance of Li-excess layered cathode materials for high-power and high-energy lithium ion batteries.

5.4 Materials and Methods

Synthesis of original Li-rich Li[Li_{0.2}Mn_{0.54}Ni_{0.13}Co_{0.13}]O₂ nanoparticles

Li-rich Li[Li_{0.2}Mn_{0.54}Ni_{0.13}Co_{0.13}]O₂ nanoparticles were synthesized using surfactant-assisted dispersion in a sol-gel method. We first prepared three precursor solutions: 5.4 mmol F127 (EO₁₀₆PO₇₀EO₁₀₆) in 50 mL ethanol, 0.08 mol transition metal acetate tetrahydrates (a molar ratio of Mn²⁺:Ni²⁺:Co²⁺=0.54:0.13:0.13) in 50 mL ethanol, and 0.12 mol lithium hydroxide in 20 mL DI water. The molar ratio of F127/Mn²⁺ was 0.01. The transition metal precursor solution was added dropwise into the F127/ethanol solution under continuous stirring at 40°C, and then the lithium precursor solution was

added. The mixed solution was heated at 80°C until the solvent was completely evaporated. Afterwards, the mixture was dried in air at 120°C for 12 h. Heat treatment of the dried mixture was carried out in air at 300°C for 3 h, followed by sintering at 900°C for 12 h. $\text{Li}[\text{Li}_{0.2}\text{Mn}_{0.54}\text{Ni}_{0.13}\text{Co}_{0.13}]\text{O}_2$ nanoparticles were collected after cooling to room temperature.

Ion exchanges in Li-rich layered $\text{Li}[\text{Li}_{0.2}\text{Mn}_{0.54}\text{Ni}_{0.13}\text{Co}_{0.13}]\text{O}_2$, and post-heat treatment of its ion-exchanged derivatives

The $\text{H}^+ - \text{Li}^+$ ion exchange of $\text{Li}[\text{Li}_{0.2}\text{Mn}_{0.54}\text{Ni}_{0.13}\text{Co}_{0.13}]\text{O}_2$ particles (1 g) was performed in aqueous HCl (150 mL, 2M) at ambient temperature. In order to promote protonation, the HCl solution was refreshed every 2 days for 10 days. As a result, a brown suspension was obtained, consisting of residual protonated intermediates in 150 mL aqueous HCl. The second ($\text{TBA}^+ - \text{H}^+$) exchange was conducted employing a 20 wt.% aqueous tetrabutylammonium ($\text{TBA} \cdot \text{OH}$) solution (Sigma Aldrich). A 1 mL suspension was added to a 5 mL $\text{TBA} \cdot \text{OH}$ solution and mixed in a vortex stirrer for 30 min. The third ($\text{Li}^+ - \text{TBA}^+$) exchange was performed in 1 M LiOH aqueous solution. All resulting ion-exchanged particles were washed with DI water and collected via centrifugation three times, followed by heating at 80°C in vacuum overnight. Finally, heat treatment of ion-exchanged derivatives was carried out at 500°C for 3h in air at a temperature ramp of 1°C min^{-1} .

Characterizations

Crystallographic structures of pristine Li-rich layered material and its derivatives were examined by a Panalytical X'pert Diffractometer with Cu K α radiation. Morphology and particle size of different samples were observed using a Hitachi S4800 field emission scanning electron microscopy (FESEM). Transmission electron microscopic (TEM) images were captured on a FEI Tecnai G2 FEG instrument at an acceleration voltage of 300 kV, to examine structures of different samples. Specific surface area of powders was measured by nitrogen adsorption/desorption at 77 K on a Quantachrome AS-1 instrument using the Brunauer-Emmet-Teller (BET) method. Chemical compositions of specimens were determined with inductively coupled plasma atomic emission spectrometry (ICP-AES) on a SPCTRO CIROS elemental analyzer.

Electrochemical measurements

The working electrodes were composed of 80 wt.% pristine Li[Li_{0.2}Mn_{0.54}Ni_{0.13}Co_{0.13}]O₂ cathode material or its derivatives, 10 wt.% acetylene black (conductive carbon, Alfa Aesar, 99.5%), and 10 wt.% poly-vinylidene fluoride (PVDF, Alfa Aesar) as the binder. These cathodes were assembled into two-electrode CR2032-type coin cells for electrochemical measurements, with metallic lithium foil as anode, and Celgard-2320 membrane as separator. The electrolyte was 1 M LiPF₆ dissolved in ethylene carbonate (EC), dimethyl carbonate (DMC) and diethyl carbonate (DEC) at a volumetric ratio of 1:1:1. Galvanostatic charge and discharge were performed at different current densities in a voltage range of 2.0 - 4.8 V vs. Li/Li⁺ using an 8-channel battery analyzer (MTI Corporation). Theoretical capacities of different cathode materials are all set to 250 mAh g⁻¹, i.e., current density corresponding to 1 C is 250 mA

g^{-1} . Cyclic voltammetric (CV) curves of cathodes were recorded at a scanning rate of 0.1 mV/s between 2.0 and 4.8 V vs. Li/Li⁺ using an electrochemical analyzer (CHI 605C).

5.5 References

- 1 Goodenough, J. B. & Park, K. S. The Li-ion rechargeable battery: a perspective. *Journal of the American Chemical Society* **135**, 1167-1176, doi:10.1021/ja3091438 (2013).
- 2 Sun, Y. *et al.* High-energy cathode material for long-life and safe lithium batteries. *Nature materials* **8**, 320-324 (2009).
- 3 Manthiram, A., Chemelewski, K. & Lee, E.-S. A perspective on the high-voltage $\text{LiMn}_{1.5}\text{Ni}_{0.5}\text{O}_4$ spinel cathode for lithium-ion batteries. *Energy & Environmental Science* **7**, 1339-1350, doi:10.1039/c3ee42981d (2014).
- 4 Lung Hao Hu, Wu, F. Y., Lin, C. T., Khlobystov, A. N. & Li, L. J. Graphene-modified LiFePO_4 cathode for lithium ion battery beyond theoretical capacity. *Nature communications* **4**, 1687, doi:10.1038/ncomms2705 (2013).
- 5 Jiang, M., Key, B., Meng, Y. S. & Grey, C. P. Electrochemical and Structural Study of the Layered, "Li-Excess" Lithium-Ion Battery Electrode Material $\text{Li}[\text{Li}_{1/9}\text{Ni}_{1/3}\text{Mn}_{5/9}]\text{O}_2$. *Chemistry of Materials* **21**, 2733-2745, doi:10.1021/cm900279u (2009).
- 6 Yabuuchi, N., Yoshii, K., Myung, S. T., Nakai, I. & Komaba, S. Detailed studies of a high-capacity electrode material for rechargeable batteries, $\text{Li}_2\text{MnO}_3\text{-LiCo}(1/3)\text{Ni}(1/3)\text{Mn}(1/3)\text{O}_2$. *Journal of the American Chemical Society* **133**, 4404-4419, doi:10.1021/ja108588y (2011).
- 7 Song, B. *et al.* High rate capability caused by surface cubic spinels in Li-rich layer-structured cathodes for Li-ion batteries. *Scientific reports* **3**, 3094, doi:10.1038/srep03094 (2013).
- 8 Ates, M. N. *et al.* Mitigation of Layered to Spinel Conversion of a Li-Rich Layered Metal Oxide Cathode Material for Li-Ion Batteries. *Journal of the Electrochemical Society* **161**, A290-A301, doi:10.1149/2.040403jes (2013).
- 9 Gu, M. *et al.* Formation of the Spinel Phase in the layered composite cathode used in Li ion batteries. *ACS Nano* **7**, 760-767 (2013).
- 10 Hy, S., Felix, F., Rick, J., Su, W. N. & Hwang, B. J. Direct in situ observation of Li_2O evolution on Li-rich high-capacity cathode material, $\text{Li}[\text{Ni}(x)\text{Li}((1-2x)/3)\text{Mn}((2-x)/3)]\text{O}_2$ ($0 \leq x \leq 0.5$). *Journal of the American Chemical Society* **136**, 999-1007, doi:10.1021/ja410137s (2014).
- 11 Jarvis, K. A., Deng, Z., Allard, L. F., Manthiram, A. & Ferreira, P. J. Atomic Structure of a Lithium-Rich Layered Oxide Material for Lithium-Ion Batteries: Evidence of a Solid Solution. *Chemistry of Materials* **23**, 3614-3621, doi:10.1021/cm200831c (2011).
- 12 Fell, C. R. *et al.* Correlation Between Oxygen Vacancy, Microstrain, and Cation Distribution in Lithium-Excess Layered Oxides During the First Electrochemical Cycle. *Chemistry of Materials* **25**, 1621-1629, doi:10.1021/cm4000119 (2013).
- 13 Mohanty, D. *et al.* Structural transformation of a lithium-rich $\text{Li}_{1.2}\text{Co}_{0.1}\text{Mn}_{0.55}\text{Ni}_{0.15}\text{O}_2$ cathode during high voltage cycling resolved by in situ X-ray diffraction. *Journal of Power Sources* **229**, 239-248, doi:10.1016/j.jpowsour.2012.11.144 (2013).

- 14 Lee, E.-S., Huq, A., Chang, H.-Y. & Manthiram, A. High-Voltage, High-Energy Layered-Spinel Composite Cathodes with Superior Cycle Life for Lithium-Ion Batteries. *Chemistry of Materials* **24**, 600-612, doi:10.1021/cm2034992 (2012).
- 15 Hy, S., Su, W.-N., Chen, J.-M. & Hwang, B.-J. Soft X-ray Absorption Spectroscopic and Raman Studies on $\text{Li}_{1.2}\text{Ni}_{0.2}\text{Mn}_{0.6}\text{O}_2$ for Lithium-Ion Batteries. *The Journal of Physical Chemistry C* **116**, 25242-25247, doi:10.1021/jp309313m (2012).
- 16 Johnson, C. S., Li, N., Lefief, C., Vaughey, J. T. & Thackeray, M. M. Synthesis, Characterization and Electrochemistry of Lithium Battery Electrodes: $x\text{Li}_2\text{MnO}_3 \cdot (1-x)\text{LiMn}_{0.333}\text{Ni}_{0.333}\text{Co}_{0.333}\text{O}_2$. *Chemistry of Materials* **20**, 6095-6106 (2008).
- 17 Amalraj, F. *et al.* Synthesis of integrated cathode materials $x\text{Li}_2\text{MnO}_3 \cdot (1-x)\text{LiMn}_{1/3}\text{Ni}_{1/3}\text{Co}_{1/3}\text{O}_2$ ($x=0.3, 0.5, 0.7$) and studies of their Electrochemical behavior. *Journal of The Electrochemical Society* **157**, A1121-A1130, doi:10.1149/1.3463782 (2010).
- 18 Wu, Y. & Manthiram, A. High capacity, surface-modified layered $\text{Li}[\text{Li}_{(1-x)/3}\text{Mn}_{(2-x)/3}\text{Ni}_{x/3}\text{Co}_{x/3}]\text{O}_2$ cathodes with low irreversible capacity loss. *Electrochemical and Solid-State Letters* **9**, A221-A224, doi:10.1149/1.2180528 (2006).
- 19 Lee, J. *et al.* Unlocking the Potential of Cation-Disordered Oxides for Rechargeable Lithium Batteries. *Science* **343**, 519-522 doi:10.1126/science.1246432 (2014).
- 20 Lin, F. *et al.* Surface reconstruction and chemical evolution of stoichiometric layered cathode materials for lithium-ion batteries. *Nature communications* **5**, 3529, doi:10.1038/ncomms4529 (2014).
- 21 Boulineau, A. *et al.* Evolutions of $\text{Li}_{1.2}\text{Mn}_{0.61}\text{Ni}_{0.18}\text{Mg}_{0.01}\text{O}_2$ during the Initial Charge/Discharge Cycle Studied by Advanced Electron Microscopy. *Chemistry of Materials* **24**, 3558-3566, doi:10.1021/cm301140g (2012).
- 22 Wang, D., Belharouak, I., Zhou, G. & Amine, K. Nanoarchitecture Multi-Structural Cathode Materials for High Capacity Lithium Batteries. *Advanced Functional Materials* **23**, 1070-1075, doi:10.1002/adfm.201200536 (2013).
- 23 Amalraj, F. *et al.* Study of the Lithium-Rich Integrated Compound $x\text{Li}_2\text{MnO}_3 \cdot (1-x)\text{LiMO}_2$ (x around 0.5; $M = \text{Mn, Ni, Co}$; 2:2:1) and Its Electrochemical Activity as Positive Electrode in Lithium Cells. *Journal of the Electrochemical Society* **160**, A324-A337, doi:10.1149/2.070302jes (2012).
- 24 Song, B., Lai, M. O., Liu, Z., Liu, H. & Lu, L. Graphene-based surface modification on layered Li-rich cathode for high-performance Li-ion batteries. *Journal of Materials Chemistry A* **1**, 9954-9965, doi:10.1039/c3ta11580a (2013).
- 25 Kang, S. H., Johnson, C. S., Vaughey, J. T., Amine, K. & Thackeray, M. M. The effects of acid treatment on the electrochemical properties of $0.5\text{Li}_2\text{MnO}_3 \cdot 0.5\text{LiNi}_{0.44}\text{Co}_{0.25}\text{Mn}_{0.31}\text{O}_2$ electrodes in lithium cells. *Journal of The Electrochemical Society* **153**, A1186-A1192, doi:10.1149/1.2194764 (2006).
- 26 Omomo, Y., Sasaki, T., Wang, L. & Watanabe, M. Redoxable nanosheet crystallites of MnO_2 derived via delamination of a layered manganese oxide. *Journal of the American Chemical Society* **12**, 3568-3575 (2003).

- 27 Kobayashi, Y., Hata, H., Salama, M. & Mallouk, T. E. Scrolled Sheet Precursor Route to Niobium and Tantalum Oxide Nanotubes. *Nano letters* **7**, 2142-2145 (2007).
- 28 Oh, E.-J. *et al.* Unilamellar Nanosheet of Layered Manganese Cobalt Nickel Oxide and Its Heterolayered Film with Polycations. *ACS Nano* **8**, 4437-4444 (2010).
- 29 Lee, K. M. *et al.* Heterolayered Li⁺-MnO₂-[Mn_{1/3}Co_{1/3}Ni_{1/3}]O₂ Nanocomposites with Improved Electrode Functionality: Effects of Heat Treatment and Layer Doping on the Electrode Performance of Reassembled Lithium Manganate. *The Journal of Physical Chemistry C* **116**, 3311-3319, doi:10.1021/jp210063c (2012).
- 30 Zhao, J. *et al.* An Ion-Exchange Promoted Phase Transition in a Li-Excess Layered Cathode Material for High-Performance Lithium Ion Batteries. *Advanced Energy Materials* **5**, n/a-n/a, doi:10.1002/aenm.201401937 (2015).
- 31 Saupe, G. B. *et al.* Nanoscale Tubules Formed by Exfoliation of Potassium Hexaniobate. *Chemistry of Materials* **12**, 1556-1562 (2000).
- 32 Zhao, J., Aziz, S. & Wang, Y. Hierarchical functional layers on high-capacity lithium-excess cathodes for superior lithium ion batteries. *Journal of Power Sources* **247**, 95-104, doi:10.1016/j.jpowsour.2013.08.071 (2014).
- 33 Robertson, A. D., Armstrong, A. R. & Bruce, P. G. Low temperature lithium manganese cobalt oxide spinels, Li_{4-x}Mn_{5-2x}Co_{3x}O₁₂ (0<x<1), for use as cathode materials in rechargeable lithium batteries. *Journal of Power Sources* **97-98**, 332-335 (2001).
- 34 Zhang, Q., Uchaker, E., Candelaria, S. L. & Cao, G. Nanomaterials for energy conversion and storage. *Chemical Society reviews* **42**, 3127-3171, doi:10.1039/c3cs00009e (2013).
- 35 Vu, A., Qian, Y. & Stein, A. Porous Electrode Materials for Lithium-Ion Batteries - How to Prepare Them and What Makes Them Special. *Advanced Energy Materials* **2**, 1056-1085, doi:10.1002/aenm.201200320 (2012).

Chapter 6. Sonication-Induced Colloidal Nanocrystals of High-Capacity Cathode Materials for Advanced Lithium-Ion Batteries

6.1 Introduction

Nanostructured materials have demonstrated wide applications in various energy conversion and storage systems with improved performances, such as solar cells, supercapacitors, catalysts, and lithium-ion batteries, etc.^{1,2,3,4,5} The functional materials used in these energy devices are mostly metals or inorganic materials, including noble metals (Pt, Co, Ag, Au, etc.), binary alloys (CdSe, PbSe, etc.), metal oxides (TiO₂, ZnO, M_xO_y (M=transition metal), etc.), and lithium-containing transition metal oxides (LiCoO₂, LiMn₂O₄, Li_x[LiMO₂]O₂, etc.).

Colloidal inorganic nanocrystals are one of the most intriguing nanomaterials, since they can function as perfect building blocks for constructing a wide variety of superstructures through facile and controllable self-assembly.^{4,6,7,8,9,10,11,12,13,14,15} Formation of colloidal inorganic nanocrystals in a stable dispersion system is the prerequisite for subsequent assembly of nanocrystals, since inorganic nanoparticles are apt to aggregate and precipitate out from solvents. Usually organic surfactants are introduced into solvents to functionalize the surface of inorganic nanoparticles at the molecular level, in order to form dispersible supramolecules.^{6,11,16} Each supramolecule consists of one inorganic core and numerous surfactant molecules capping at its surface via various interactions, i.e., hydrogen bonding, Van der Waals forces, electrostatic forces, $\pi - \pi$ interactions, etc.^{17,18,19,20,21} The subsequent self-assembly of surfactant-

assisted inorganic colloids during solvent evaporation is depended on the sensitivity of surfactant molecules to external stimuli, such as temperature, light, solvent polarity, pH and ionic strength. As such, control of stimuli can be used to manipulate interactions between the surfactant molecules and core materials, and thus tailor assembly behaviors of the colloids.^{9,11} However, surfactant-assisted colloids suffer from the following limitations. First of all, most surfactants not only have complex molecular structures but also require special toxic solvents, like hydrazine, o-dichlorobenzene, toluene and chloroform, due to their dissolution compatibility with these solvents.^{6,14,16,22} Second, stability of surfactant-assisted colloidal dispersion systems is quite susceptible, since the surfactant molecules are very sensitive to external stimuli.⁹ Finally, removing the surfactants after the assembly can be time and energy consuming. It is also noted most colloidal systems synthesized so far are based on metals, simple oxides or semiconductors; few has been reported concerning colloids of complex inorganic compounds with multiple elements. Therefore, it would be very intriguing to explore formation and assembly of colloidal inorganic nanocrystals based on multiple-element complex compound in a common non-toxic solvent without using any surfactants.

The Li-excess transition metal oxide, $\text{Li}_{1.2}\text{Mn}_{0.54}\text{Ni}_{0.13}\text{Co}_{0.13}\text{O}_2$ (LMNCO), has attracted tremendous research attention as a promising cathode material for high-capacity lithium-ion batteries, due to its very high theoretical capacity of 321 mAh g^{-1} and wide operating voltage range of 2.0 - 4.8 V vs. Li/Li^+ .^{23,24,25,26,27,28,29} LMNCO is composed of two components, lithium-inactive Li_2MnO_3 (space group $C2/m$) and lithium-active $\text{LiMn}_{1/3}\text{Ni}_{1/3}\text{Co}_{1/3}\text{O}_2$ (space group $R-3m$) at a molar ratio of 1:1, i.e., $0.5\text{Li}_2\text{MnO}_3 \cdot 0.5\text{LiMn}_{1/3}\text{Ni}_{1/3}\text{Co}_{1/3}\text{O}_2$, in the integrated layered structure with Li-excess

characteristics.^{23,24,26} However, practical applications of these Li-excess cathodes are limited by considerable irreversible capacity loss in the first cycle, oxygen loss from the lattice during the first cycle, reaction with the electrolyte at the high operating voltage of up to 4.8 V, and low rate capability.³⁰ The huge irreversible capacity loss is due to the rearrangement of the layered oxide lattice at the end of first charge, resulting in an elimination of oxide ion vacancies and a corresponding number of lithium sites. As a result, not all the lithium extracted at the end of first charge could be inserted back into the lattice, resulting in a waste of capacity.

It is well accepted that the electrochemical performance of an electrode material depends on not only the intrinsic characteristics of the material but also its designed morphologies.¹ The problems mentioned above can be alleviated by fabricating nanostructured $\text{Li}[\text{Li},\text{Mn},\text{Ni},\text{Co}]\text{O}_2$ that provides high surface area, efficient electron transport pathway, improved electronic conductivity, and structural flexibility/stability for volume change during lithiation/delithiation. However, most $\text{Li}[\text{Li},\text{Mn},\text{Ni},\text{Co}]\text{O}_2$ materials reported in literature are submicron-sized, which show improved electrochemical properties but did not solve all the problems, especially the poor cycleability and low rate capability.³¹ It remains a challenge to obtain nano-sized or nanoarchitected $\text{Li}[\text{Li},\text{Mn},\text{Ni},\text{Co}]\text{O}_2$ due to its multiple-element complex composition and structure. Some approaches have been reported for fabricating nanostructured or nanoarchitected Li-excess layered cathode materials including solvothermal process and lithiation of nanostructured transition metal precursors.^{29,32,33,34} But these methods usually involve complicated and time-consuming synthetic procedures.

Self-assembly of surfactant-free LMNCO colloids could be a more facile and effective route for constructing diverse nanostructured or nanoarchitected LMNCO. To avoid using surfactants, ultrasonic cavitation phenomena have been observed and demonstrated to effectively disintegrate the aggregates and further fragment the dispersed particles into numerous monodisperse nanocrystals at nanoscale and/or sub-nanoscale in solvents.^{10,35,36} Sonication-induced formation of colloidal dispersions, followed by self-assembly has been extensively reported for the gelation system,^{37,38,39,40} but has not been reported for inorganic particles. In comparison with strong interactions between sonically generated radicals in the gelators, interactions between inorganic nanocrystals are very delicate and trivial, mostly resulting in an unstable suspension of inorganic nanoparticles. In this work, we report facile sonication-induced formation of tunable LMNCO colloidal nanocrystals in ethanol, a common and non-toxic solvent, without any assistance from surfactants.

The present work introduces a novel sonication-induced method to synthesize Li-excess transition metal oxide colloids in ethanol and explores the formation mechanism of the colloids. The effects of ultrasonic cavitation on inducing the interaction between LMNCO nanocrystals and ethanol molecules are studied using theoretical simulation and dynamic light scattering technique. It is suggested that the ultrasonic treatment contributes to “activating” the surface of LMNCO nanocrystals during the cavitation event in addition to breaking up LMNCO particles into nanocrystals. The LMNCO nanocrystals are thus enabled to absorb ethanol molecules via hydrogen bonding, resulting in the formation of LMNCO-EtOHs supramolecules with negative surface charge. The electrostatic repulsion force between LMNCO colloids helps to stabilize

LMNCO nanocrystals in ethanol, which facilitates subsequent self-assembly of nanocrystals during evaporation of the solvent. In this case, the colloidal dispersion system only consists of two components, LMNCO nanocrystals and ethanol, without any surfactants, which offers better and easier control over self-assembly procedure for constructing elaborate nanoarchitectures. The self-assembly behaviors of LMNCO colloids are studied, and the effect of assembling LMNCO into nanoarchitectures on improving its electrochemical performance is also evaluated.

6.2 Results and Discussion

6.2.1 Sonication-induced generation colloidal nanocrystals and solvent evaporation promoted morphology reconstruction of Lithium excessed oxide.

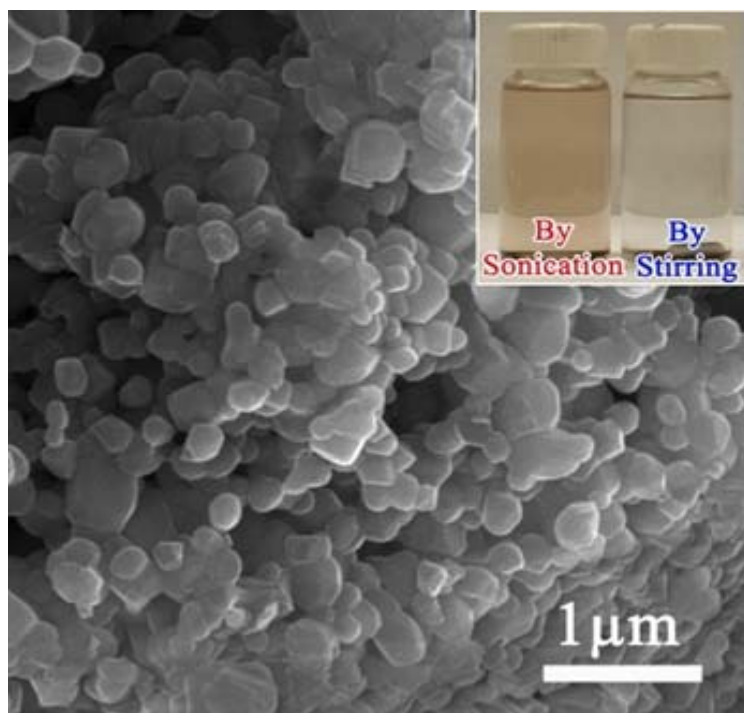


Fig. 6.2.1.1. SEM image of original LMNCO particles

Fig. 2.1.1.1 reveals the SEM image of original LMNCO particles with polyhedral shape and an average particle size of ~ 250 nm. As shown in Fig. 6.2.1.2 accordingly, the relative particle size distribution (PSD) indicates a high-level aggregation of the as-prepared LMNCO powders, which is probably attributed to the high annealing temperature at 900°C during the synthesis. The distinguishing effects on dispersing LMNCO particles in ethanol via different means can be obviously seen from the inset photographs in Fig. 6.2.1.1. It is interesting to note the sonication-assisted approach results in a stable and brown dispersion (the left vial) when 10 mg LMNCO powders are ultra-sonically dispersed in 20 mL ethanol for 2 h, followed by settling for 2 days. In contrast, the vigorous magnetic stirring at 60°C shows little effect on stabilizing LMNCO particles in the solvent (the right vial). The heating process is used to accompany the stirring treatment, because the dispersion system after 2 h sonication shows a temperature of $\sim 60^{\circ}\text{C}$. As reported in literature,^{35,36} the strong cavitation and streaming effects during the ultra-sonication process not only effectively disintegrate the original LMNCO aggregates into individual nanocrystals, but also yield broken chemical bonds on the surface of the newly-formed LMNCO nanocrystals. Consequently, such active surface might induce potential interactions between LMNCO nanocrystals and surrounding ethanol molecules, such as hydrogen bonding, in order to drastically lower the surface free energy.^{20,41} As a result, a stable colloidal dispersion of Li-excess transition metal oxide is achieved in a possible form of LMNCO-EtOHs supramolecules. On the other hand, shear stress from magnetic stirring even under heating is too weak to trigger this phenomenon. It should be noted that only a fraction of original LMNCO particles form the colloidal dispersion after settling for 2 days. In the case shown in Fig. 6.2.1.1, the

actual dispersion concentration is 0.12 mg/mL, much smaller than the nominal concentration of 0.5 mg/mL. Surprisingly, the concentrations of different colloidal dispersions are affected by the initial mass of LMNCO powders before sonically dispersing in the 20 mL solvent; hence, the nominal dispersion concentrations are used hereafter.

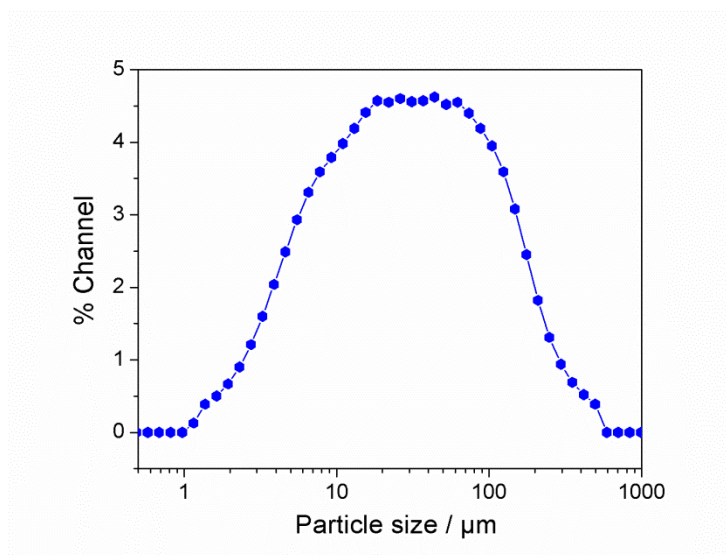


Fig. 6.2.1.2. Particle size distribution of the as-prepared LMNCO powders.

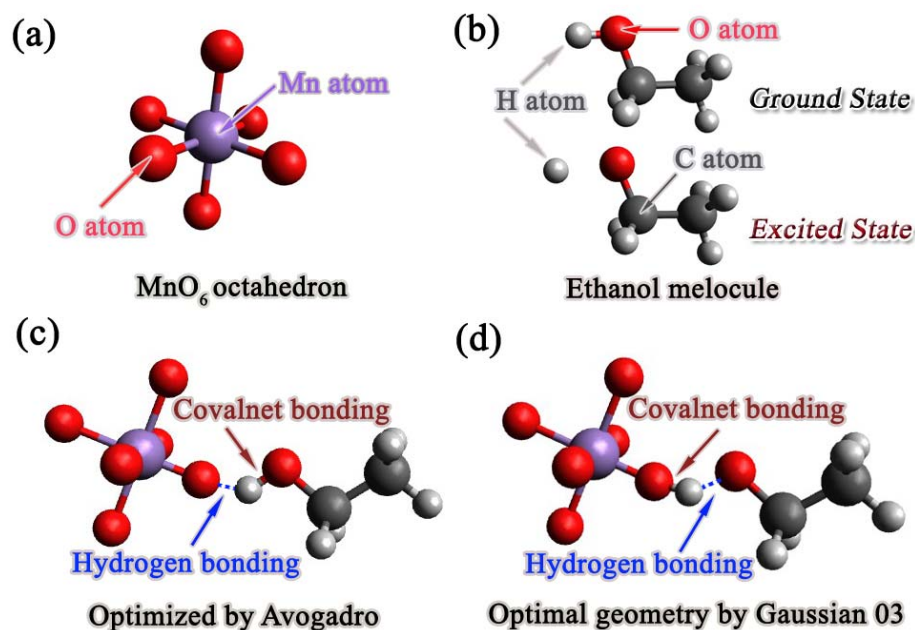


Fig.6.2.1.3. A theoretical study by simulating the interaction between LMNCO nanocrystals and ethanol molecules via hydrogen bonding: (a) the structural configuration of MnO_6 octahedron representative of Li-excess transition metal oxide, (b) the molecular structure of an ethanol molecule (EtOH) at ground and excited states, respectively, (c) the composite structure of MnO_6 - EtOH optimized by Avogadro, and (d) the optimal geometry of MnO_6 - EtOH by Gaussian 03.

Theoretical calculation was carried out in order to understand the potential interaction existed between LMNCO and EtOH molecules. It has been known that LMNCO has a very complex structure consisting of two components (Li_2MnO_3 and $\text{LiMn}_{1/3}\text{Ni}_{1/3}\text{Co}_{1/3}\text{O}_2$) in Li-rich characteristics. The integrated layered structure of Li-excess transition metal oxide is formed by transition metal cations occupying on octahedral sites within cubic close-packed oxygen arrays;²³ MnO_6 octahedron is the predominant unit within Mn-based Li-rich LMNCO. Therefore, we simplify our simulation work by employing a MnO_6 octahedron as a representative for Li-excess layered LMNCO to react with ethanol molecules ($\text{CH}_3\text{CH}_2\text{OH}$). As reported in literatures,^{44,45} UB3LYP is one of the most successful hybrid functions, and LANL2DZ is

capable for transition-metal-involved calculation for a creditable modeling study. Hence, we employ UB3LYP/LANL2DZ level of theory to manipulate the geometry optimization, frequency analysis and time-dependent density-functional theory (TD-DFT) calculation between MnO_6 and EtOH units. The property of the ethanol molecule alone is also calculated using the same level of theory. Fig. 6.2.1.3a displays the unit configuration of the MnO_6 octahedron. As the oxidation state of Mn in MnO_6 octahedron is tetravalent, i.e., there is one unpaired 3d electron, the multiplicity of the MnO_6 unit is set to 2. All oxygen ions are assumed to be negatively bivalent. Fig. 6.2.1.3 b shows the optimized geometry of an EtOH molecule at ground state and excited state, respectively. A quasi-deprotonation event can be predicted for the ethanol molecule at its excited state, giving rise to an extremely weak bonding between O and H in OH groups. MnO_6 and EtOH were first put together in Avogadro as shown in Fig. 6.2.1.3c. A composite structure can be optimized first via Avogadro by forming the hydrogen bonding between one exposed oxygen atom from MnO_6 and the hydrogen atom in hydroxyl group (OH) from EtOH molecule. Hydrogen bonding formation was predicted between one oxygen atom from MnO_6 and hydrogen atom from the hydroxyl group of EtOH when MnO_6 and EtOH molecule are close enough, which represent the case at solid liquid interface in real systems when LMNCO nanoparticles was in direct contact with EtOH solvent. Geometric optimization between the MnO_6 octahedron and EtOH molecule was then attempted by Gaussian 03. The geometry optimization did not yield a defined minimum and did not converge within the default thresholds. Nevertheless, the dissociated $\text{EtO}\cdot\cdot\text{H}$ and newly-formed H-O-Mn structures are predicted by the calculations as shown in Fig. 6.2.1.3 d. Such composite geometry indicates the existence of an interactional force between MnO_6

and EtOH, in which the EtOH molecule shows certain geometric changes due to the existence of MnO_6 . Furthermore, Fig. 6.2.1.3 d reveals complete de-protonation of EtOH molecule after the optimal modeling calculation, which is different from the covalent bonding in the original ethanol (Fig. 6.2.1.3b and 6.2.1.3c). Simultaneously, a new covalent bonding is formed between the free hydrogen atom from EtOH and an oxygen atom from MnO_6 . As a result, the theoretical calculation illustrates that the ethanol molecule has an intensive tendency to interact with the exposed oxygen from Li-excess transition metal oxide via hydrogen bonding, and the geometry of ethanol molecule within the optimal MnO_6 -EtOH composite structure is similar as the excited state of the original ethanol (Fig. 6.2.1.3 b). This calculation also predicted a negative surface charge on the particle surface due to the absorption of the deprotonated ethanol molecules.

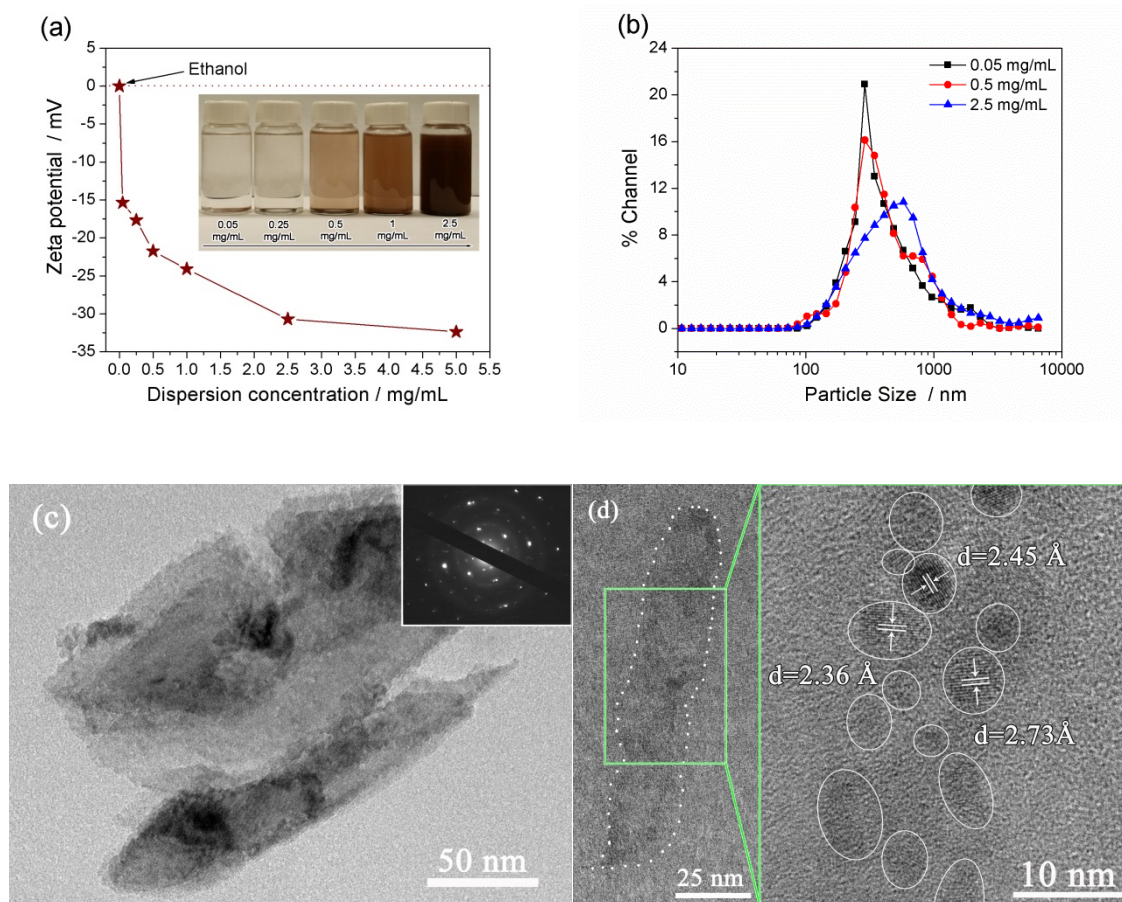


Fig. 6.2.1.4. (a) Zeta potentials and photographs in the inset and (b) particle size distribution of LMNCO/ethanol colloidal systems with different dispersion concentrations; (c) TEM images of dominant LMNCO nanocrystals and (d) HRTEM images of LMNCO monocrystals from a colloidal dispersion with a concentration of 0.5 mg/mL.

Fig. 6.2.1.4 explores the particle characteristics of LMNCO nanocrystals and surface charge properties of LMNCO colloids in the stable colloidal dispersion system via dynamic light scattering and microscopic techniques. Fig. 6.2.1.4a shows the Zeta potentials (ζ , mV) of various colloidal dispersions with different dispersion concentrations ranging from 0.05 to 5 mg/mL, along with the selected photographs in the inset. Darker color indicates more LMNCO nanocrystals being stabilized in the 20 mL ethanol, leading to a higher concentration of the colloidal system. The negative signal of

ζ potentials indicates the negative surface charge of LMNCO colloids,⁴⁶ which is well agreed with our theoretical calculation. Accordingly, PSD analyses in Fig. 6.2.1.4 b reveal LMNCO nanocrystals in the colloidal dispersion have larger particle size when the concentration increases, possibly because the water-bath-based sonication has limited power to disintegrate the LMNCO aggregates when the initial quantity of the particles increases in the system.³⁶ Since the absolute value of ζ potential is associated with the magnitude of surface charges,⁴⁷ ζ potentials in Fig. 6.2.1.4 a indicate that a colloidal LMNCO system with a larger particle size possesses more negative surface charge within a stable colloidal system at a higher concentration. Such phenomenon is accordance with the simulation result, because a larger LMNCO core having a larger surface area can adsorb more ethanol molecules at the surface, and thus contributes to the higher negative charge of LMNCO-EtOHs supermolecule, i.e., the resultant LMNCO individual.

TEM images are captured to examine detailed morphology and structure of the dispersive LMNCO nanocrystals. The specimens are prepared by dropping 0.5 mL colloidal dispersion on the TEM copper grid, followed by drying at room temperature. Fig. 6.2.1.4 d and 6.2.1.4 e present two different forms of LMNCO nanocrystals coexisting in a colloidal dispersion at a dispersion concentration of 0.5 mg/mL. As shown in Fig. 6.2.1.4c, most LMNCO nanocrystals have a mean particle size around 200 nm, which is consistent with the PSD analysis (Fig. 3b). The inset selected area electron different (SAED) pattern shows the combination of polycrystalline and monocrystalline characteristics of these nanocrystals. In contrast, high-resolution TEM (HRTEM) image in Fig. 6.2.1.4d reveals LMNCO monocrystals with an average particle size of ~ 5 nm.

The cavitation effect during the sonication process can not only disintegrate LMNCO aggregates into individual particles, but also smash individual LMNCO particle into numerous smaller nanocrystals.³⁶ When original LMNCO nanoparticle is cleaved to generate new surfaces, the structure of the two newly-created surfaces may or may not be the same. If two structures at the each surface are identical, the surface will be dipoleless and is considered a nonpolar surface. If they are different, the surface will have a strong dipole and is considered a polar surface. Due to the complexity of sonication environment, nanocrystals with different surface properties were generated. This was evidenced by the fact pieces of nanocrystals were also found in the precipitate after sonication while other portion of newly-created nanocrystals were suspended in the solvent. The generation of multiple exposed defective oxygen anionic centers (Lewis base) at the newly-created surfaces should be mainly accountable for the stability of those suspended nanocrystals via formation of hydrogen bonding with solvent molecules (ethanol) as predicted by the theoretical calculation. On the other hand, sonication-induced cutting might also generate a few exposed defective metal cationic centers (Lewis acid), which can also interact with the solvent molecules via coordination.⁴⁸ Further, Fig. 6.2.1.4d reveals the self-assembly characteristics of LMNCO nanocrystals after the removal of ethanol on the TEM copper grid, which will discuss in details below.

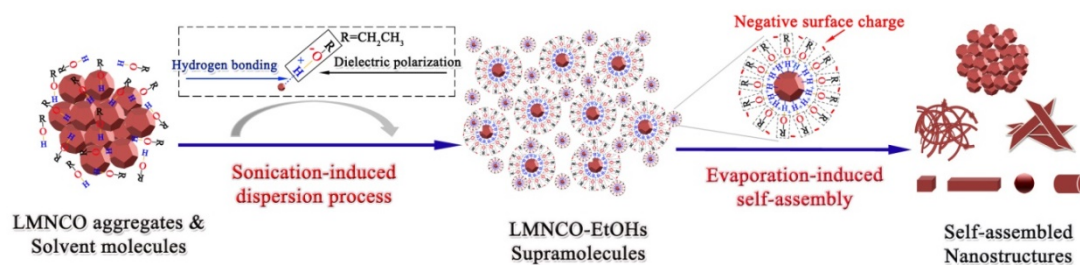


Fig. 6.2.1.5 Schematics showing the sonication-induced colloidal LMNCO nanocrystals to form LMNCO-EtOHs supramolecules, and the resultant superstructures through evaporation-induced self-assembly.

Based on all the analyses above, we propose a formation mechanism of LMNCO colloids as presented in Fig. 6.2.1.5. During the initial sonication-induced process, the ultrasonic cavitation plays a crucial role to form and activate LMNCO nanocrystals by breaking up original LMNCO aggregates (Fig. 6.2.1.1). The interaction between the newly-formed LMNCO nanocrystals and ethanol molecules can be referred to the simulation study in Fig. 6.2.1.3, which states that an individual LMNCO nanocrystal tends to absorb EtOH molecules via hydrogen bonding, in order to lower its surface free energy. As a result, a new, stronger bonding might be formed between hydrogen atoms from EtOH molecules and oxygen atoms from LMNCO nanocrystals, while the dissociation of EtOH molecules occurs. Such chemisorption leads to an elongated covalent bonding in the hydroxyl groups within the absorbed EtOH molecules, resulting in the electronic transition and subsequent dielectric polarization of EtOH molecules. Since each LMNCO nanocrystal can absorb numerous EtOH molecules, the effect from the dielectric polarization of EtOH molecules accumulates at the surface of the LMNCO nanocrystal core, which contributes to a negative surface charge of individual LMNCO-EtOHs supramolecules. Therefore, LMNCO colloids in ethanol are stabilized by electrostatic repulsion of the negatively-charged LMNCO-EtOHs supramolecules.^{18,21} Additionally, the excellent dispersibility of LMNCO colloids may arise from the steric effects of EtOH molecules as well.^{9,20} In short, colloidal LMNCO nanocrystals can be easily prepared in ethanol via one-step sonication-induced process and the proposed formation mechanism of LMNCO-EtOHs supramolecules is consistent with the characterizations of the dispersion system.

The colloidal dispersion of inorganic nanocrystals offers a promising route for constructing complex superstructures through facile self-assembly.^{9,11,14} In the case of Li-excess layered transition metal oxide, LMNCO colloids are only associated with solvent molecules. Mechanism of self-assembly behaviors of colloidal LMNCO nanocrystals can be referred to the evaporation-induced self-assembly (EISA) that has been extensively reported in literatures.^{9,12,14} Evaporation of the solvent gives rise to the progressively increasing concentration of nonvolatile colloidal components. Such process can be easily affected by the evaporation environment in combination with chemical and/or physical properties of both solvent molecules and inorganic nanocrystal cores. During the evaporation of ethanol, the van der Waals attraction among LMNCO-EtOHs supramolecules is increased, leading to the gradual aggregation of LMNCO nanocrystals, meanwhile the liquid-vapor interface serves as the nucleating sites for assembly of LMNCO nanocrystals.^{10,12}

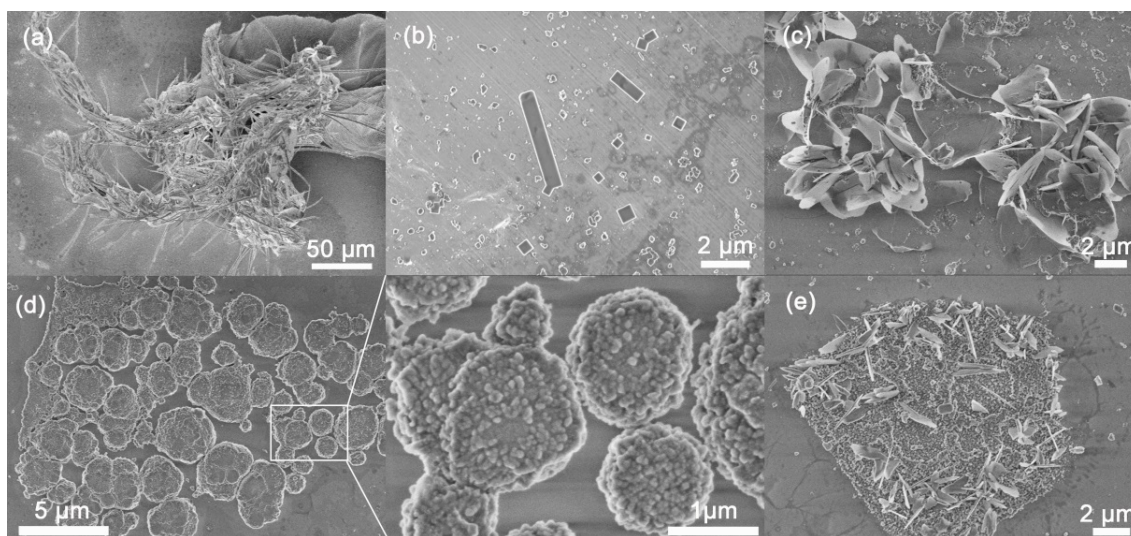


Fig. 6.2.1.6 SEM images of various nanoarchitectures via self-assembly of LMNCO colloids on Al substrates at 80°C: (a) fiber networks, (b) regular-shaped blocks, (c) sheet networks, (d) aggregates of particles with magnified details, and (e) a composite structure.

Fig. 6.2.1.6 shows the resultant products via self-assembly after evaporating the ethanol in the colloidal dispersion with a concentration of 0.5 mg/mL on the Al substrate at 80°C. The evaporation temperature is set slightly higher than the boiling point of the ethanol (78.4°C), to ensure an inhomogeneous evaporation environment. SEM images in Fig. 6.2.1.6 display four major micron-sized architectures assembled from colloidal LMNCO nanocrystals, indicating very complicated self-assembly behaviors. The self-assembly products are expected to show diverse morphology and architectures such as rods, sheets, cubes, spheres, etc., since concentration of the colloidal system changes during evaporation of ethanol and different concentrations yield different morphology/structure. For example, the dipole-dipole interaction of LMNCO-EtOHs supramolecules arising from the asymmetrical charge distribution of LMNCO colloids can lead to the micron-sized network of rods during the solvent evaporation process (Fig. 6.2.1.6 a). Similar behavior has been observed in evaporation induced assembly of gold nanoparticles in ethanol.⁴² Rabani and co-workers reported that when the solvent evaporation is inhomogeneous and the concentration of colloidal nanocrystals is low, network structures are mostly apt to form as vapor nuclei meet owing to infrequent nucleation events.¹² This assembly is only stable if the interfaces are frozen following the evaporation, resulting in extremely long networks of LMNCO rods with a length at sub-millimeter scale (Fig. 6.2.1.6 a). Otherwise, networks break down to yield distinct fragments that asymptotically evolve by coarsening. As a result, different shapes of LMNCO blocks, including cube, cuboid, diamond, sphere, etc., are formed as revealed in Fig. 5b. The length of the LMNCO blocks ranges from several nanometers to microns, possibly due to an effect equivalent to the Ostwald ripening occurring during

nanoparticle fabrication process.³⁹ The two assemblies summarized above occur more easily for LMNCO colloids with low concentrations,⁴³ which are probably dominant for small LMNCO monocrystals in Fig. 6.2.1.4 d, due to their higher thermodynamic activity and kinetics than larger LMNCO nanocrystals.

During the evaporation process, continuous loss of the ethanol solvent leads to the increased concentration of LMNCO-EtOHs supramolecules. Hence, self-assembly of LMNCO is dominated by two- and three-dimensional (2D and 3D) aggregation of LMNCO nanocrystals in order to drastically reduce the surface free energy in the dispersion system.^{13,10,43} The 2D assembly results in sheet network (Fig. 6.2.1.6 c) constructed from small LMNCO nanocrystals, and 3D assembly of large LMNCO nanoparticles yields spherical aggregates in Fig. 6.2.1.6 d. Fig. 6.2.1.6 e reveal the simultaneous and competing progresses of 2D and 3D assembly. The simulation study by Rabani and his co-workers reported that the shapes of terminal structures can be affected by the evaporation conditions and diffusion coefficient of nanoparticles in the colloidal dispersion system during the drying-mediated self-assembly process.¹² These preliminary results provide useful clues for producing tailorable superstructures via controlling the self-assembly process.

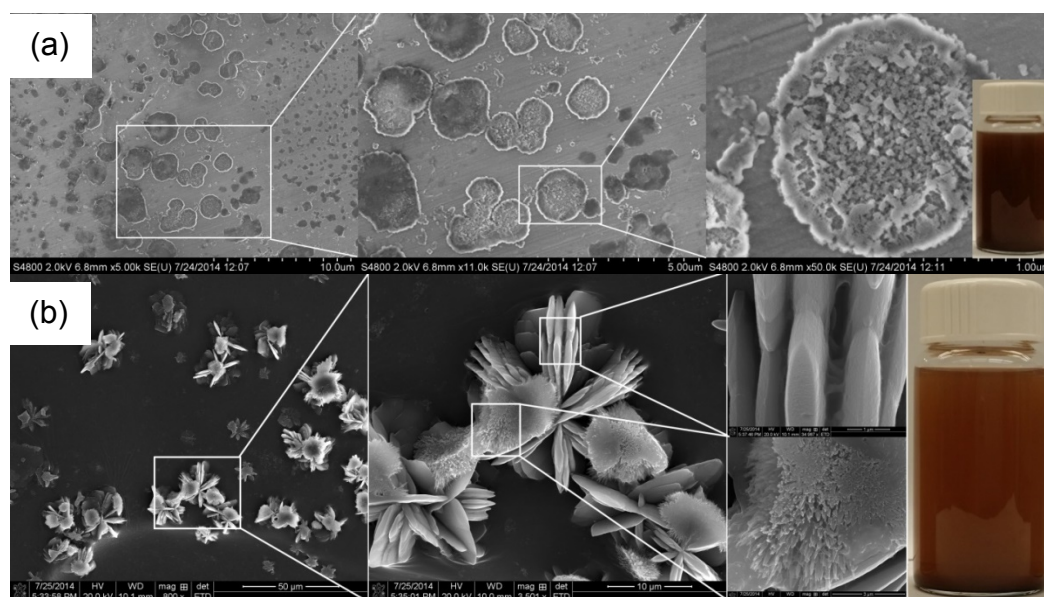


Fig. 6.2.1.7 SEM images of superstructures assembled from LMNCO colloidal system with a dispersion concentration of 2.5 mg/mL at room temperature prepared in (a) DI water, and (b) methanol with an inserted photo showing corresponding colloidal dispersion.

Furthermore, Fig. 6.2.1.7 manifests that the formation of colloidal LMNCO dispersion and subsequent self-assembly behaviors can be extended to other solvents such as distilled water and methanol, since both of them have hydroxyl groups to interact with LMNCO particles via hydrogen bonding. It is possible that volatility of different solvents can further influence the properties of LMNCO colloids during solvent evaporation process, resulting in distinguishing assembly behaviors. Our ongoing work focuses on comprehensively study and precisely control the self-assembly of LMNCO colloids in various solvents, in order to achieve tailorable assembled nanostructures of LMNCO material and its analogs.

6.2.2 Structure and electrochemical evaluation of the re-assembled product

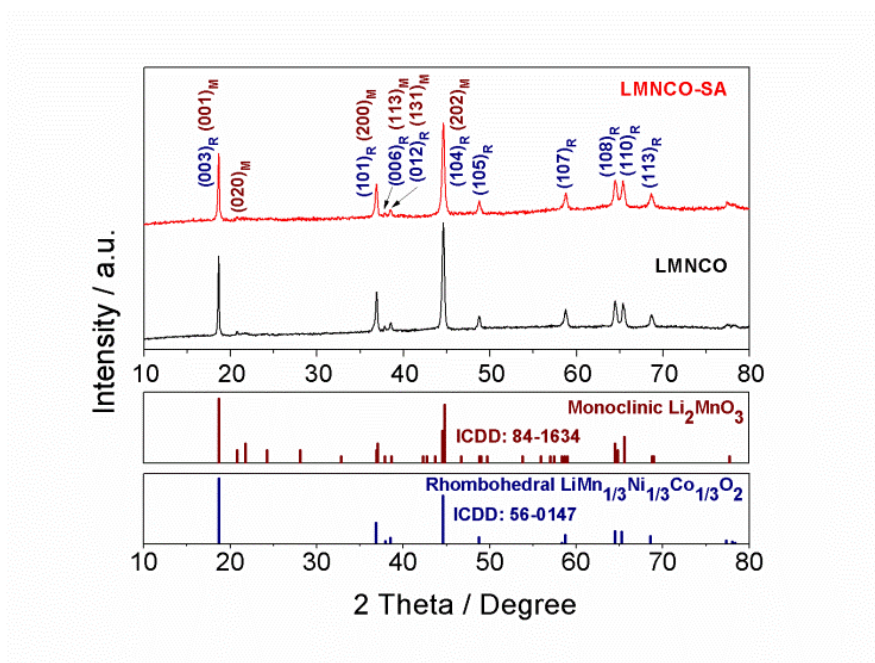


Fig. 6.2.2.1 XRD patterns of original LMNCO particles and the self-assembly product from a colloidal system with a dispersion concentration of 0.5 mg/mL (LMNCO-SA).

As shown in Fig. 6.2.2.1, the powders collected from the self-assembly of colloids (marked as LMNCO-SA) have identical XRD patterns as the pristine LMNCO particles, indicating that assembly of LMNCO into superstructures does not affect its chemical composition and crystal phase.

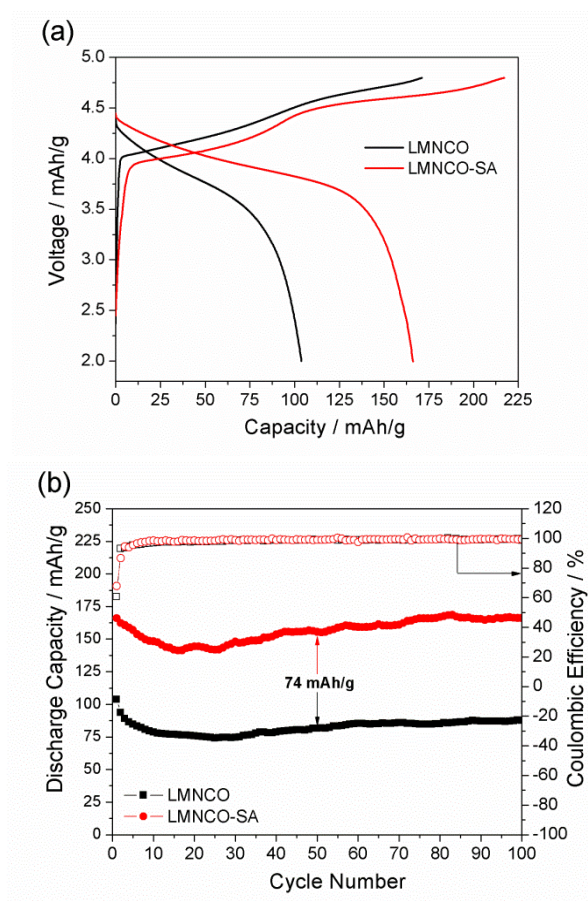


Fig. 6.2.2.2 Electrochemical performances of original LMNCO particles and the self-assembly product from LMNCO colloidal system (LMNCO-SA), cycled in a voltage range of 2.0-4.8 V vs. Li/Li^+ : (a) initial charge and discharge curves, and (b) cycling performances at a current density of 0.5 C ($1\text{C} = 250 \text{ mA g}^{-1}$) and corresponding Coulombic efficiencies.

Since Li-excess transition metal oxide is a promising high-capacity cathode material for lithium ion batteries, it would be very interesting to evaluate electrochemical properties of the assembled LMNCO architectures in comparison with the pristine LMNCO particles. Fig. 6.2.2.2a presents initial charge/discharge curves of LMNCO and LMNCO-SA cathodes at 0.5 C ($1\text{C} = 250 \text{ mA g}^{-1}$) in a voltage range of 2.0-4.8 V vs. Li/Li^+ . The nanostructured LMNCO-SA delivers a discharge capacity of 166.1 mAh g^{-1} , much higher than 103.8 mAh g^{-1} of the original LMNCO particles. It is noted that self-

assembly of LMNCO contributes to the significantly improved specific capacity and reduced electrochemical polarization in the initial cycle. On the other hand, LMNCO-SA and LMNCO both show low Columbic efficiencies of 67.26% and 60.66%, respectively, which are attributed to electrochemical activation of inert Li_2MnO_3 component in LMNCO,²⁹ indicating the same electrochemical characteristic of LMNCO before and after self-assembly. However, self-assembly of LMNCO exhibits phenomenal effect on enhancing its cycling stability. As shown in Fig. 6.2.2.2 b, LMNCO-SA retains approximately 100% of initial discharge capacity after 100 electrochemical cycles, while LMNCO shows moderate discharge capacity retention of 84.5%. Such remarkably increased capacity and improved cycleability in LMNCO-SA are attributed to the assembled superstructures that can offer more lithium active sites and effectively release reaction strains during lithiation/delithiation processes and phase conversion.¹

6.3 Conclusions

In summary, an inorganic colloidal dispersion system is facilely synthesized by inducing interactions between inorganic nanocrystals and solvent molecules via one-step sonication. In the case of Li-excess transition metal oxide dispersed in ethanol, hydrogen bonding plays a crucial role to form stable and dispersible colloidal supramolecules, in which the surface of LMNCO core is capped by numerous ethanol molecules via hydrogen bonding. Such chemisorption gives rise to the dielectric polarization of ethanol molecules, resulting in negative surface charge of colloidal nanocrystals. The formation mechanism of the surface-charged inorganic colloids in the ethanol is proposed, and demonstrated by Zeta potential measurements as well as simulation studies. The self-assembly behavior of solvent-assisted colloidal nanocrystals is also explored. The

assembled architectures of Li-excess layered transition metal oxide are evaluated for applications as cathode materials in lithium ion batteries and show significantly enhanced electrochemical performance compared to original particles, delivering a much higher specific capacity and better cycling stability. This work presents an ultra-facile route for preparing inorganic colloids in common solvent, and provides a promising approach to assemble inorganic particles into tailorable nanoarchitectures for significantly improved performance in device applications.

6.4 Materials and Methods

Synthesis of Li-excess $\text{Li}[\text{Li}_{0.2}\text{Mn}_{0.54}\text{Ni}_{0.13}\text{Co}_{0.13}]\text{O}_2$ oxide. $\text{Li}[\text{Li}_{0.2}\text{Mn}_{0.54}\text{Ni}_{0.13}\text{Co}_{0.13}]\text{O}_2$ (marked as LMNCO) particles were synthesized using surfactant-assisted dispersion in a sol-gel method. We first prepared three precursor solutions: 5.4 mmol F127 ($\text{EO}_{106}\text{PO}_{70}\text{EO}_{106}$) in 50 mL ethanol, 0.08 mol transition metal acetate tetrahydrates (a molar ratio of $\text{Mn}^{2+}:\text{Ni}^{2+}:\text{Co}^{2+}=0.54:0.13:0.13$) in 50 mL ethanol, and 0.12 mol lithium hydroxide in 20 mL DI water. The molar ratio of F127/ Mn^{2+} was 0.01. The transition metal precursor solution was added dropwise into the F127/ethanol solution under vigorous stirring at 40°C, and then the mixed solution was added into the lithium precursor solution. The final mixture was heated at 80°C until the solvent was completely evaporated. Afterwards, the mixture was dried in air at 120°C for 12 h. Heat treatment of the dried mixture was carried out in air at 300°C for 3 h, followed by sintering at 900°C for 12 h. $\text{Li}[\text{Li}_{0.2}\text{Mn}_{0.54}\text{Ni}_{0.13}\text{Co}_{0.13}]\text{O}_2$ particles were collected after cooling to room temperature.

Preparation of colloidal $\text{Li}[\text{Li}_{0.2}\text{Mn}_{0.54}\text{Ni}_{0.13}\text{Co}_{0.13}]\text{O}_2$ nanocrystal dispersions in the solvent. Preparation of $\text{Li}[\text{Li}_{0.2}\text{Mn}_{0.54}\text{Ni}_{0.13}\text{Co}_{0.13}]\text{O}_2$ colloids in ethanol was carried out using an one-step sonication treatment in a VWR B2500A-BTH ultrasonication water bath, operating at 210 W and 40 kHz. A certain amount of LMNCO particles was directly dispersed in 20 mL ethanol within a cap-sealed disposable scintillation vial by sonication for 2 h. The stable colloidal dispersions of LMNCO nanocrystals were obtained after settling for 2 days, and then examined by various characterizations. The dispersion concentration with a unit of mg/mL was calculated by dividing the original mass of LMNCO powders over the volume of ethanol (20 ml). Other solvents containing a hydroxyl group, such as methanol and DI water, can also be used.

Characterization:

Crystallographic structures of original $\text{Li}[\text{Li}_{0.2}\text{Mn}_{0.54}\text{Ni}_{0.13}\text{Co}_{0.13}]\text{O}_2$ particles and powders collected from colloidal dispersions after the removal of the solvent, were examined by a Panalytical X'pert Diffractometer with $\text{Cu K}\alpha$ radiation. Morphology and particle size of the samples were observed using a Hitachi S2500 field emission scanning electron microscopy (FESEM). Transmission electron microscopic (TEM) images were captured on a JEM-2010 microscopy at an acceleration voltage of 200 kV. Excitation and emission spectra of pristine LMNCO solid particles, ethanol solvent and colloidal dispersions were measured by HORIBA Fluorolog-3 Spectrofluorometer. Geometry optimizations in the simulation study were performed by Gaussian-03 using UB3LYP/LANL2DZ level of theory. The Zeta potential (ζ , mV) values and particle size distribution (PSD) of LMNCO colloids in ethanol at different dispersion concentrations were measured by a MicroTrac

ZetaTrac analyzer based on the principle of dynamic light scattering. A 3 mW laser source with a wavelength of 780 nm was used as the light source.

Electrochemical measurements. The working electrodes were composed of 80 wt.% original $\text{Li}[\text{Li}_{0.2}\text{Mn}_{0.54}\text{Ni}_{0.13}\text{Co}_{0.13}]\text{O}_2$ particles or self-assembled powders, 10 wt.% acetylene black (conductive carbon, Alfa Aesar, 99.5%), and 10 wt.% polyvinylidene fluoride (PVDF, Alfa Aesar) as the binder. These cathodes were assembled into two-electrode CR2032-type coin cells for electrochemical measurements, with metallic lithium foil as anode and Celgard-2320 membrane as separator. The electrolyte was 1 M LiPF_6 dissolved in ethylene carbonate (EC), dimethyl carbonate (DMC) and diethyl carbonate (DEC) at a volumetric ratio of 1:1:1. Theoretical capacity of the cathode materials is set to 250 mAh g^{-1} , i.e., the specific current corresponding to 1 C is 250 mA g^{-1} . Galvanostatic charge and discharge were performed at 0.5 C in a voltage range of 2.0 - 4.8 V vs. Li/Li^+ using an 8-channel battery analyzer (MTI Corp.).

6.5 References

1. Zhang, Q.; Uchaker, E.; Candelaria, S. L.; Cao, G., Nanomaterials for energy conversion and storage. *Chemical Society reviews* **2013**, 42 (7), 3127-71.
2. Yua, G.; Xie, X.; Pan, L.; Bao, Z.; Cui, Y., Hybrid nanostructured materials for high-performance electrochemical capacitors. *Nano energy* **2013**, 2, 213-234.
3. Stein, A.; Wilson, B. E.; Rudisill, S. G., Design and functionality of colloidal-crystal-templated materials--chemical applications of inverse opals. *Chemical Society reviews* **2013**, 42 (7), 2763-803.
4. Kannan, P.; Maiyalagan, T.; Opallo, M., One-pot synthesis of chain-like palladium nanocubes and their enhanced electrocatalytic activity for fuel-cell applications. *Nano Energy* **2013**, 2, 677-687.
5. Nie, Z.; Petukhova, A.; Kumacheva, E., Properties and emerging applications of self-assembled structures made from inorganic nanoparticles. *Nature Nanotechnology* **2010**, 5, 15-25.
6. Puentes, V. F.; Krishnan, K. M.; Alivisatos, P., Colloidal nanocrystal shape and size control The case of cobalt. *Science* **2001**, 291, 2115-2117.
7. Cho, K.-S.; Talapin, D. V.; Gaschler, W.; Murray, C. B., Designing PbSe nanowires and nanorings through oriented attachment of nanoparticles. *Journal of the American Chemical Society* **2005**, 127, 7140-7147.
8. Srivastava, S.; Kotov, N. A., Nanoparticle assembly for 1D and 2D ordered structures. *Soft Matter* **2009**, 5, 1146-1156.
9. Grzelczak, M.; Vermant, J.; Furst, E. M.; Liz-Marzan, L. M., Directed self-assembly of nanoparticles. *ACS Nano* **2010**, 4, 3591-3605.
10. Bassett, D. C.; Merle, G.; Lennox, B.; Rabiei, R.; Barthelat, F.; Grover, L. M.; Barralet, J. E., Ultrasonic phosphate bonding of nanoparticles. *Advanced materials* **2013**, 25 (41), 5953-8.
11. Li, F.; Josephson, D. P.; Stein, A., Colloidal assembly: the road from particles to colloidal molecules and crystals. *Angewandte Chemie* **2011**, 50 (2), 360-88.
12. Rabani, E.; Reichman, D. R.; Geissler, P. L.; Brus, L. E., Drying-mediated self-assembly of nanoparticles. *Nature* **2003**, 426, 271-274.
13. Dang, R.; Song, L.; Dong, W.; Li, C.; Zhang, X.; Wang, G.; Chen, X., Synthesis and self-assembly of large-area Cu nanosheets and their application as an aqueous conductive ink on flexible electronics. *ACS applied materials & interfaces* **2014**, 6 (1), 622-9.
14. Misztal, K.; Graaf, J. d.; Bertoni, G.; Dorfs, D.; Brescia, R.; Marras, S.; Ceseracciu, L.; Cingolani, R.; Roij, R. v.; Dijkstra, M.; Manna, L., Hierarchical self-assembly of suspended branched colloidal nanocrystals into superlattice structures. *Nature Materials* **2011**, 10, 872-876.
15. Chen, P.; Luo, Z.; Guven, S.; Tasoglu, S.; Ganesan, A. V.; Weng, A.; Demirci, U., Microscale assembly directed by liquid-based template. *Advanced materials* **2014**, 26 (34), 5936-41.
16. Kovalenko, M. V.; Scheele, M.; Talapin, D. V., Colloidal nanocrystals with molecular metal chalcogenide surface ligands. *Science* **2009**, 324 (5933), 1417-20.

17. Min, Y.; Akbulut, M.; Kristiansen, K.; Golan, Y.; Israelachvili, J., The role of interparticle and external forces on the assembly and properties of nanoparticle materials. *Nature Materials* **2008**, *7*, 527-538.
18. Bishop, K. J.; Wilmer, C. E.; Soh, S.; Grzybowski, B. A., Nanoscale forces and their uses in self-assembly. *Small* **2009**, *5* (14), 1600-30.
19. Lin, Y.; Böcker, A.; Jinbo He, K. S.; Xiang, H.; Abetz, C.; Li, X.; Wang, J.; Emrick, T.; Long, S.; Wang, Q.; Balazs, A.; Russell, T. P., Self-directed self-assembly of nanoparticle/copolymer mixtures. *Nature* **2005**, *434* (7029), 55-59.
20. Ni, W.; Mosquera, R. A.; Perez-Juste, J. P.; Liz-Marzan, L. M., Evidence for hydrogen-bonding-directed assembly of gold nanorods in aqueous solution. *The Journal of Physical and Chemistry Letters* **2010**, *1*, 1181-1185.
21. Young, K. L.; Jones, M. R.; Zhang, J.; Macfarlane, R. J.; Esquivel-Sirvent, R.; Nap, R. J.; Wu, J.; Schatz, G. C.; Lee, B.; Mirkin, C. A., Assembly of reconfigurable one-dimensional colloidal superlattices due to a synergy of fundamental nanoscale forces. *PNAS* **2012**, *109*, 2240-2245.
22. Yamada, M.; Shen, Z.; Miyake, M., Self-assembly of discotic liquid crystalline molecule-modified gold nanoparticles: control of 1D and hexagonal ordering induced by solvent polarity. *Chemical communications* **2006**, (24), 2569-71.
23. Boulineau, A.; Simonin, L.; Colin, J.-F.; Canévet, E.; Daniel, L.; Patoux, S., Evolutions of $\text{Li}_{1.2}\text{Mn}_{0.61}\text{Ni}_{0.18}\text{Mg}_{0.01}\text{O}_2$ during the Initial Charge/Discharge Cycle Studied by Advanced Electron Microscopy. *Chemistry of Materials* **2012**, *24* (18), 3558-3566.
24. Amalraj, F.; Kovacheva, D.; Talianker, M.; Zeiri, L.; Grinblat, J.; Leifer, N.; Goobes, G.; Markovsky, B.; Aurbach, D., Synthesis of integrated cathode materials $x\text{Li}_2\text{MnO}_3 \cdot (1-x)\text{LiMn}_{1/3}\text{Ni}_{1/3}\text{Co}_{1/3}\text{O}_2$ ($x=0.3, 0.5, 0.7$) and studies of their Electrochemical behavior. *Journal of The Electrochemical Society* **2010**, *157* (10), A1121-A1130.
25. Wu, Y.; Manthiram, A., High capacity, surface-modified layered $\text{Li}[\text{Li}_{(1-x)/3}\text{Mn}_{(2-x)/3}\text{Ni}_{x/3}\text{Co}_{x/3}]\text{O}_2$ cathodes with low irreversible capacity loss. *Electrochemical and Solid-State Letters* **2006**, *9* (5), A221-A224.
26. Yabuuchi, N.; Yoshii, K.; Myung, S. T.; Nakai, I.; Komaba, S., Detailed studies of a high-capacity electrode material for rechargeable batteries, $\text{Li}_2\text{MnO}_3\text{-LiCo}_{1/3}\text{Ni}_{1/3}\text{Mn}_{1/3}\text{O}_2$. *Journal of the American Chemical Society* **2011**, *133* (12), 4404-4419.
27. Song, B.; Liu, H.; Liu, Z.; Xiao, P.; Lai, M. O.; Lu, L., High rate capability caused by surface cubic spinels in Li-rich layer-structured cathodes for Li-ion batteries. *Scientific reports* **2013**, *3*, 3094.
28. Gu, M.; Belharouak, I.; Zheng, J.; Wu, H.; Xiao, J.; Genc, A.; Amine, K.; Thevuthasan, S.; R. Baer, D.; Zhang, J.-G.; Browning, N. D.; Liu, J.; Wang, C., Formation of the Spinel Phase in the layered composite cathode used in Li ion batteries. *ACS Nano* **2013**, *7* (1), 760-767.
29. Zhao, J. Q.; Wang, Y., High-capacity full lithium-ion cells based on nanoarchitected ternary manganese–nickel–cobalt carbonate and its lithiated derivative. *Journal of Materials Chemistry A* **2014**, *2*, 14947–14956.
30. Armstrong, A. R.; Holzapfel, M.; Novak, P.; Johnson, C. S.; Kang, S.-H.; Thackeray, M. M.; Bruce, P. G., Demonstrating Oxygen Loss and Associated Structural

- Reorganization in the Lithium Battery Cathode $\text{Li}[\text{Ni}_{0.2}\text{Li}_{0.2}\text{Mn}_{0.6}]\text{O}_2$. *Journal of the American Chemical Society* **2006**, *128*, 8694-8698.
31. Zhao, J.; Aziz, S.; Wang, Y., Hierarchical functional layers on high-capacity lithium-excess cathodes for superior lithium ion batteries. *Journal of Power Sources* **2014**, *247*, 95-104.
 32. Zhang, J.; Guo, X.; Yao, S.; Zhu, W.; Qiu, X., Tailored synthesis of $\text{Ni}_{0.25}\text{Mn}_{0.75}\text{CO}_3$ spherical precursors for high capacity Li-rich cathode materials via a urea-based precipitation method. *Journal of Power Sources* **2013**, *238*, 245-250.
 33. Wang, D.; Belharouak, I.; Zhou, G.; Amine, K., Nanoarchitecture Multi-Structural Cathode Materials for High Capacity Lithium Batteries. *Advanced Functional Materials* **2013**, *23* (8), 1070-1075.
 34. Xi, L.; Cao, C.; Ma, R.; Wang, Y.; Yang, S.; Deng, J.; Gao, M.; Lian, F.; Lu, Z.; Chung, C. Y., Layered $\text{Li}_2\text{MnO}_3.3\text{LiNi}(0.5-x)\text{Mn}(0.5-x)\text{Co}(2x)\text{O}_2$ microspheres with Mn-rich cores as high performance cathode materials for lithium ion batteries. *Physical chemistry chemical physics : PCCP* **2013**, *15* (39), 16579-85.
 35. Verdan, S.; Burato, G.; Comet, M.; Reinert, L.; Fuzellier, H., Structural changes of metallic surfaces induced by ultrasound. *Ultrasonics Sonochemistry* **2003**, *10* 291-295.
 36. Huang, Y. Y.; Knowles, T. P. J.; Terentjev, E. M., Strength of nanotubes, filaments and nanowires from sonication-induced scission. *Advanced materials* **2009**, *21*, 3945-3948.
 37. Malicka, J. M.; Sandeep, A.; Monti, F.; Bandini, E.; Gazzano, M.; Ranjith, C.; Praveen, V. K.; Ajayaghosh, A.; Armaroli, N., Ultrasound stimulated nucleation and growth of a dye assembly into extended gel nanostructures. *Chemistry-A European Journal* **2013**, *19* (39), 12991-3001.
 38. Maity, S.; Kumar, P.; Haldar, D., Sonication-induced instant amyloid-like fibril formation and organogelation by a tripeptide. *Soft Matter* **2011**, *7*, 5239-5245.
 39. Thompson, J. A.; Chapman, K. W.; Koros, W. J.; Jones, C. W.; Nair, S., Sonication-induced Ostwald ripening of ZIF-8 nanoparticles and formation of ZIF-8-polymer composite membranes. *Microporous and Mesoporous Materials* **2012**, *158*, 292-299.
 40. Ye, F.; Chen, S.; Tang, G.; Wang, X., Sonication induced morphological transformation between 3D gel network and globular structure in a two-component gelation system. *Colloids and Surfaces A: Physicochemical and Engineering Aspects* **2014**, *452* 165-172.
 41. Yang, Y.; Yang, A.-L.; Yang, R.-Q.; Yuan, G.-J.; Shi, Y.-L., Investigation of the Enhancement Fluorescence of Ethanol Doped SiO_2 Nanoparticles. *Journal of Nanoscience and Nanotechnology* **2011**, *11*, 9717-9720.
 42. Liao, J.; Zhang, Y.; Yu, W.; Xu, L.; Ge, C.; Liu, J.; Gu, N., Linear aggregation of gold nanoparticles in ethanol. *Colloids and Surfaces A: Physicochemical and Engineering Aspects* **2003**, *223*, 177-183.
 43. Shipway, A. N.; Lahav, M.; Gabai, R.; Willner, I., Investigations into the Electrostatically Induced Aggregation of Au Nanoparticles. *Langmuir* **2000**, *16*, 8789-8795.
 44. Okumura, M.; Kitagawa, Y.; Haruta, M.; Yamaguchi, K., DFT studies of interaction between O_2 and Au clusters. The role of anionic surface Au atoms on Au clusters for catalyzed oxygenation. *Chemical Physics Letters* **2001**, *346* (1-2), 163-168.

45. Lu, X.; Tian, F.; Feng, Y.; Xu, X.; Wang, N.; Zhang, Q., Sidewall oxidation and complexation of carbon nanotubes by base-catalyzed cycloaddition of transition metal oxide: a theoretical prediction. *Nano Letters* **2002**, *2*, 1325-1327.
46. Yang, S. C.; Paik, S. Y.; Ryu, J.; Choi, K. O.; Kang, T. S.; Lee, J. K.; Song, C. W.; Ko, S., Dynamic light scattering-based method to determine primary particle size of iron oxide nanoparticles in simulated gastrointestinal fluid. *Food chemistry* **2014**, *161*, 185-191.
47. Han, J.; Zhou, C.; Wu, Y.; Liu, F.; Wu, Q., Self-assembling behavior of cellulose nanoparticles during freeze-drying: effect of suspension concentration, particle size, crystal structure, and surface charge. *Biomacromolecules* **2013**, *14* (5), 1529-1540.
48. Glazneva, T. S.; Kotsarenko, N. S.; Paukshtis, E. A., Surface acidity and basicity of oxide catalysts: From aqueous suspensions to in situ measurements. *Kinetics and Catalysis* **2008**, *49* (6), 859-867.